Self-Consistent Solution of Schrödinger's and Poisson's Equations in Carrier Confining Heterostructures

by

Steve Joseph Shelemy

A Thesis Submitted to
the Faculty of Graduate Studies
in Partial Fulfilment of the Requirements
for the Degree of

MASTER OF SCIENCE

Department of Electrical and Computer Engineering
University of Manitoba
Winnipeg, Manitoba
Canada

UNIVERSITY OF MANITOBA

THE UNIVERSITY OF MANITOBA

FACULTY OF GRADUATE STUDIES

*****

COPYRIGHT PERMISSION

Self-Consistent Solution of Schrödinger's and Poisson's Equations in Carrier Confining Heterostructures

BY

Steve Joseph Shelemy

A Thesis/Practicum submitted to the Faculty of Graduate Studies of The University of Manitoba in partial fulfillment of the requirement of the degree

OF

MASTER OF SCIENCE

THE UNIVERSITY OF MANITOBA

FACULTY OF GRADUATE STUDIES

*****

MASTER'S THESIS/PRACTICUM FINAL REPORT

The undersigned certify that they have read the Master's Thesis/Practicum entitled:

Self-Consistent Solution of Schrödinger's and Poisson's Equations in Carrier Confining Heterostructurers

submitted by

Steve Shelemy

in partial fulfillment of the requirements for the degree of

Master of Science

The Thesis/Practicum Examining Committee certifies that the thesis/practicum (and oral examination if required) is:

Approved

(Approved or Not Approved)

☐ Thesis

Dr. G. Bridges, Advisor, ECE

Dr. D. Buchanan, ECE

Dr. P. Loly, Physics and Astronomy

Date: August 23, 2006

Abstract

A self-consistent solution of the Schrödinger and Poisson equations is developed to calculate the energy levels and energy band offsets of a carrier confining heterostructure which is of finite extent bound by either vacuum/air or metallic contacts. The Schrödinger equation is solved in the Hartree approximation in which the band edge is the superposition of a 'bulk' band potential and a potential resulting from the presence of ionized donor (or acceptor) atoms and charge carriers distributed throughout the device. Our self-consistent method involves decoupling the Schrödinger and Poisson equations by developing an approximate expression for the dependence of the electron density on the potential energy. The finite element method (FEM), employing Hermite polynomial basis functions, is used to solve the Schrödinger and Poisson equations. We present a simple integration by parts method to derive the required finite element equations. Multiple well structures at different temperatures and donor densities are used as examples.

Acknowledgements

I would like to thank my thesis advisor Dr. Greg Bridges for allowing me to pursue this thesis topic and putting up with my disappearing for periods of time as the priorities of my full time job demanded my attention. Without his encouragement, support, and guidance this thesis would not have been possible.

I would like to recognize my employer, Manitoba Hydro for the financial support of this Master of Science Degree. I would also like to thank the many people at Manitoba Hydro encouraged me to embark on graduate studies at the University of Manitoba and who encouraged me through the many long years of study. Marv Kloss and Nancy Dykstra from the Engineer-in-Training Program, Allan Silk, Lorne Midford, Dr. Doug Chapman my past and present supervisors/managers. In particular I would like to thank Dr. David Swatek and Dr. Wenjie Zhang for the many useful discussions which help me to pick this topic and guided me through my research. Finally I want to thank Robert Yonza for taking the time to proof read this manuscript, I greatly appreciate his efforts on catching all my typing errors and his input on improving the readability of this manuscript.

I would also like to thank my family and friends who gave me their ear as I struggled to balance a full time job, graduate studies and personal life. Without your ear and support I could have never finished the long journey to complete this thesis. Thankyou!

Table of Contents

List of Figures

List of Tables

1) Introduction

1.1 Motivation

Advances in the crystal growth of semiconductor heterostructures have enabled nearly precise atomic control over the growth of the layers of heterostructure semiconductor crystals. These advanced manufacturing techniques together with accurate theoretical modelling of the electron dispersion relations and optical properties coupled with improved numerical modelling such as the finite element method have ushered in the concept of *wave function engineering*. Wave function engineering is the ability to 'engineer' a carrier wave function through simulation to achieve some desired optical or electrical properties before manufacturing the actual crystal. Through the use of heterostructure architecture the mechanisms governing carrier dynamics like overlap, density of states, tunnelling times, lifetimes of carrier recombination, optical detection efficiencies, non-linear optical properties, etc. can all be altered. To a remarkable degree the probability density or occupancy of carriers in any region of a heterostructure can be controlled through the use of thin layers of different materials, employing asymmetric wells, localizations of barrier layers, controlling intervalley transfer via externally applied fields, control of optical phonon emission via strain, and tailor the band mixing and properties via the use of diluted magnetic semiconductor layers [1],[2],[3]. Wave function engineering has also allowed the creation of a new generation of advanced and novel devices based on precise control over the electric and optical properties of quantum heterostructures with novel geometries including quantum wires, quantum wave guides, and quantum interference transistors to name a few.

In a semiconductor heterostructure, the presence of local discontinuities in the conduction and valence band edges leads to the possibility of separating free charge carriers from their parent donor or acceptor atoms. This redistribution of charge results in an electric potential which alters the bulk band edge profile.

Through the use of a self-consistent solution of the Schrödinger and the Poisson equations the band edge 'bending' can be calculated. The self-consistent solution is known to be numerically unstable because a small change in potential results in a large change in the distribution of charge in the device. The effect of the layered semiconductor architecture and all applied fields including electric, magnetic, or mechanical can be included in the self-consistent solution. The most elementary self-consistent solution is the calculation of the band edge profile of a layered semiconductor heterojunction.

The self-consistent calculation of the band edge profile was previously referred to as band-gap engineering and has been used to investigate the characteristics of semiconductor devices in order to improve their operation. For example Tsuneya [4],[5] used a self-consistent model to calculate the subband structure, light-scattering spectra, and low temperature mobility of a GaAs/Al_xGa_{1-x}As heterojunction. Shur *et. al.* [6] developed a self-consistent model to be used for the design of doped channel quantum well HIGFETs. This model involves the calculation of the subbands and electron density in quantum wells and is use to determine the effect of the doping of the channel regions on the thermionic emission gate current. Foulger *et. al.* [7] used self-consistent modelling to investigate the effect that band edge bending has on the gain/current relation and carrier leakage of quantum well lasers. Zid *et. al.* [8] solve the Schrödinger and Poisson equations self-consistently to calculate the conduction-band edge profile with and without an applied electric field of a resonant tunnelling diode and investigate the Stark effect (change in band levels due to applied fields) and interband transitions which are of interest for voltage-tunable optoelectronic devices.

The finite element method (FEM) had gained considerable interest for solving problems in quantum mechanics because of its ease in implementation and high accuracy [9]. For example, the finite element method has been found to

provide realistic numbers for the energy spectra in quantum well devices. Such accuracy is crucial in the study of linear and non-linear optical properties of semiconductor heterostructures [10].

The finite element method rests on more rigorous mathematical foundations than finite difference methods [11]. This gives one a better feel of its accuracy and error analysis. It gives an approximate solution which is defined throughout the configuration space rather than being isolated at discrete points [12]. It can easily accommodate local additions or deletions of degrees of freedom (adding or subtracting nodal points). These advantages of the finite element method, including that it can easily be applied to carrier confinement problems where the effective mass and potential are complicated functions of position and that it tends to be more stable in classically forbidden regions, mean that it is ideally suited to the self-consistent solution.

1.2 Background

Iteration methods used to solve the self-consistent problem typically involve inputting some 'seed' or starting 'input' potential which represents the band structure into the Schrödinger equation and solving for the wave functions and energy eigenvalues of bound states. Using the wave function and energy eigenvalue information the electron charge distribution is calculated and together with the donor distribution input into Poisson's equation to solve for an 'output' potential. A self-consistent solution is achieved when the 'input' potential to the Schrödinger equation is equal to the 'output' potential from Poisson's equation. The key problem to iteration schemes is how to generate the new or updated 'input' Potential to be used in the Schrödinger equation for the next iteration.

The earliest method used to self-consistently solve the Schrödinger and Poisson equations was an under-relaxation method [15],[19],[21],[22]. Solution by under-relaxation involved solving the coupled non-linear partial differential equations by an iteration between Poisson and Schrödinger equations as follows; 1) Solve the Poisson equation using electron density from last iteration, 2) Solve Schrödinger's equation using the potential from step 1, 3) Calculate the intermediate charge density, 4) Calculate a 'new' charge density using the 'intermediate' and 'old' charge densities via under-relaxation and 5) Repeat until charge density is stationary. The inherent instability of this self-consistent iteration process arises because the required value of the relaxation parameter is not known in advance. Instability also arises because the electron density is not a function of the potential.

The best way to improve any self-consistent algorithm is to decouple the Schrödinger and Poisson equations in such a way as to dampen out oscillations in the total charge density. This is possible with the knowledge of the exact dependence of the quantum electron density on the electrostatic potential[22]. Unfortunately a direct solution of the Schrödinger equation yields an electron

number density which depends on the wave functions $\psi_i(z)$ and corresponding energy eigenvalues E_i alone,

$$n_e(z) = n_e\left(E_i, \psi_i(z)\right). \tag{1.1}$$

If we knew the exact dependence of the electron charge density on potential, we could substitute this into the non-linear Poisson's equation and improve solution stability. Unfortunately the exact dependence is not known, but an alternative method is to find an approximate expression relating the electron charge density to the potential,

$$n_e(z) \approx n_e\left(V(z)\right). \tag{1.2}$$

In this way an inner iteration loop which does not include the solution to Schrödinger's equation can be used to 'predict' $n_e(z)$ and $V(z)$. These predictions can then be 'corrected' in an outer iteration step by an exact solution to Schrödinger's equation. Several different self-consistent algorithms have been proposed, all with the aim of improving solution stability and convergence.

Self-consistent methods typically involve a Hartree approximation to the band structure. In this approximation the Schrödinger equation is not solved using the periodic potential due to atoms occupying the crystal lattice. Instead the band structure is represented by a macroscopic bulk band edge potential with a potential function, resulting from the distribution of charge inside the semiconductor, added to it. The Schrödinger equation is solved in an effective mass approximation for envelope wave functions and corresponding energy eigenvalues. The envelope approximation does not contain the periodic Bloch functions normally associated with the solution to Schrödinger's equation for a crystal lattice. Bastard[17] has shown that little is lost in the envelop approximation as the bulk semiconductor characteristics are contained in the envelop function.

One of the first attempts at achieving convergence of the self-consistent

solution of the Schrödinger and Poisson equations in an iterative scheme was by Stern[15],[16]. Stern introduced two iteration methods which form the basis of methods used today. The first he called the 'extrapolated-convergence-factor' method and the second of which he called 'perturbation-iteration' method.

The simplest means for generating a new 'input' potential of the k^{th} iteration is to scale the old input potential by some fraction of the difference between the output potential and input potential in a given iteration. That is,

$$V_{input}^{(k+1)}(z) = V_{input}^{(k)}(z) + f^{(k+1)} \cdot W^{(k)}(z) \tag{1.3}$$

where,

$$W^{(k)}(z) = V_{output}^{(k)}(z) - V_{input}^{(k)}(z) \tag{1.4}$$

and f is a weighting factor typically in the range $0 \leq f \leq 1$ used to control the rate of convergence. In Stern's 'extrapolated-convergence-factor' method f is extrapolated from iteration to iteration using[15],

$$f^{(k+1)} = \frac{f^{(k)}}{1-r} \tag{1.5}$$

where,

$$r = \frac{w^{(k)}}{w^{(k-1)}} \tag{1.6}$$

where $w^{(k)}$ is a measure of the convergence in the k^{th} iteration and is that value of $W^{(k)}(z)$ which has the largest magnitude and may be positive or negative. The choice of the weighting factor is very important, too small of a factor leads to a very slow rate of convergence, too large of a factor leads to oscillations with the solution possibly never converging and in some cases diverging.

In his second method, 'perturbation–iteration' method, instead of solving for the output potential directly, Stern uses perturbation theory to develop a relationship between the change in the input potential and the change in output

potential. Using this relationship he creates the new input potential using the equation,

$$V_{input}^{(k+1)}(z_i) = V_{input}^{(k)}(z_i) + \sum_j A_{ij}\left(V_{output}^{(k)}(z_j) - V_{input}^{(k)}(z_j)\right) \qquad \textbf{(1.7)}$$

where **A** is a matrix which is derived from perturbation theory and relates how a change in input potential (or 'perturbation' in input potential) will change the energy eigenvalues and corresponding wave functions (and hence change the electron charge distribution). This method was found to have improved convergence at the cost of increased computation time since the related equations to find the **A** matrix must be solved for each bound state individually.

Stern's solution involved solving the **A** matrix only for a subset of the grid used to solve the Schrödinger and Poisson equations and used interpolation to 'fill' in the remaining grid points. His algorithm was restricted to solving for the fields and energy levels present at a semiconductor junction.

Inoue *et. al.* [18] used a self-consistent calculation to determine the energy levels of a selectively doped AlGaAs/GaAs/AlGaAs quantum well heterostructure device under an electric field. Their self-consistent solution method is centred on determining the Fermi energy E_F from the set of analytical expressions for the potential at the well/barrier interface. Starting with an arbitrary input potential function Inoue *et. al.* used a finite element method to solve the Schrödinger equation for the wave functions and corresponding energy eigenvalues. Using the wave functions and energy eigenvalues they solved for the electron distribution in the well and together with an estimate of the depletion region the Fermi energy was calculated such that the potential at the well/barrier interface satisfied the relation,

$$\phi_{barrier} = \phi_{well} - \left(\frac{\Delta E_c}{e}\right), \qquad \textbf{(1.8)}$$

where ΔE_c is the conduction band discontinuity. Using this Fermi energy level a

new potential was calculated using Poisson's equation,

$$\varepsilon_0 \kappa \frac{d^2\phi(z)}{dz^2} = e\sum_i N_i \psi_i^2(z) - \rho(z), \tag{1.9}$$

where $\psi_i(z)$ is the wavefuction of the i^{th} subband, $\rho(z)$ is the impurity charge density and N_i is the electron distribution of the i^{th} subband given by,

$$N_i = \frac{m^* k_B T}{\pi\hbar^2} \ln\left[1 + \exp\left(\frac{E_F - E_i}{k_B T}\right)\right]. \tag{1.10}$$

The new potential is inserted back into the Schrödinger equation and the entire process iterated until a self-consistent potential is achieved.

Another algorithm for solving the self-consistent problem of an electron in a quantum wire (2-D quantum well) was purposed by Kerkhoven *et. al.* [19],[20] and involved inner and outer iteration loops. Their method involved solving for the electron charge density using an iterative fixed point mapping,

$$T(n_e(z)) = n_e(z). \tag{1.11}$$

In the fixed point mapping a function which corresponds to the logarithm of the electron density is mapped to its function value,

$$T(n_e(z)) \quad \rightarrow \quad n_e(z) = \exp\left(\overline{n}_e(z)\right) - \delta \tag{1.12}$$

through the successive solution of Poisson's equation and the eigenvalue problem of Schrödinger's equation (where δ is an arbitrary small number to avoid the singularity of the logarithm at zero). This forms the inner loop. Self-consistency is obtained through the outer iteration in which the Poisson's equation is solved using the 'new' electron density. Kerkhoven *et. al.* also purposed stabilization and acceleration methods for the inner loop using adaptive under-relaxation for the initial solution,

$$n_e^{(k+1)}(z) = qT(n_e^{(k)}(z)) + (1-q)n_e^{(k)}(z) \tag{1.13}$$

(q is the relaxation parameter) and Newton's method,

$$n_e^{(k+1)}(z) = T(n_e^{(k)}(z)) \tag{1.14}$$

as the solution approached convergence. Schrödinger's equation is solved using the Chebyshev subspace iteration algorithm and Poisson's equation is solved using a Conjugate Gradient algorithm. Their self-consistent algorithm is reported to be stable for a range of temperatures and electron densities. However, at very low temperatures the Fermi Dirac function is observed to create convergence problems if eigenstates are near the Fermi Energy. In this case oscillations may arise as the eigenstate is completely occupied in one iteration and empty in the next iteration.

Kim *et. al.* [21] recognized the importance of charge neutrality for the solution to the self-consistent problem and utilized an integration method to solve for the Poisson equation which naturally satisfies charge neutrality. They used a Ritz variational method to solve the Schrödinger equation. The self-consistent solution is solved using the standard under-relaxation method described above.

Trellakis *et. al.* [22] developed an impoved self-consistent scheme to solve for the Schrödinger-Poisson equations in a quantum heterostructure. Using quantum mechanical perturbation theory, they developed an expression which describes the dependence of the electron density on the electrostatic potential,

$$n_e\left(V(z)+\delta V(z)\right) = N_e \sum_i \psi_i^2(z) \boldsymbol{F}_{-\frac{1}{2}}\left(\frac{E_F - E_i(V) + e\,\delta V}{k_B T}\right) \tag{1.15}$$

Here F_k is the Fermi-Dirac integral of order k,

$$F_k(x) = \frac{1}{\Gamma(k+1)} \int_0^\infty \frac{t^k dt}{\exp(t-x)+1}, \quad k > -1, \tag{1.16}$$

and δV is the perturbation in the potential. This expression was then used in a predictor-corrector iteration scheme to solve for the bound electron states of a

GaAs-AlGaAs quantum wire. Their method involved the following steps; 1) Solve the non-linear Poisson's equation, 2) Solve Schrödinger's equation, 3) Calculate the exact quantum electron density and 4) Repeat until stationary. No under-relaxation is necessary in this method. To avoid the cost of solving the Schrödinger equation in a large grid Trellakis *et. al.* solved Schrödinger's equation to determine the correct expression of the electron charge density in the well region only. In the rest of the solution domain the electron density was given by its classical value. Using Chebyshev-Arnoldi iteration to solve the Schrödinger equation and Newton-Raphson iteration to solve Poisson's equation, their method was found to have excellent convergence speed and stability.

More recently Ram-Mohan *et. al.* [13], [14] have borrowed the work by Trellakis *et. al.* and included multi-band theory. Using the finite element method they improved the method presented by Trellakis by solving for the change in the potential function $\delta V(z)$ from iteration to iteration instead of the potential function directly. Using perturbation theory they developed an expression which describes the dependence of the electron density on the electrostatic potential,

$$n_e(z) = 4\pi |e| \int dz\, \varphi_l(z) \sum_i \Lambda_i(z) \left(\frac{\partial F(\varepsilon_i)}{\partial \varepsilon_i} \right) \left(\frac{\partial \varepsilon_i}{\partial V} \right) \tag{1.17}$$

where $\varphi_l(z)$ are the finite element shape functions, $\Lambda_i(z)$ is the charge carrier density of states, and $F(\varepsilon)$ is the Fermi distribution function. Instead of solving the Fermi-Dirac integral, the related functional derivatives were approximated as a finite difference of nodal values. The Fermi energy was specifically calculated to ensure charge neutrality in the semiconductor device. They assumed a free electron solution for electrons not confined in the well region which leads to a difficulty in predicting the energies of the free electron states.

Their solution method followed these steps; 1) Starting from a seed potential solve Schrödinger's for the wave functions and energy eigenvalues, 2)

calculate the Fermi energy to ensure charge neutrality, 3) solve Poisson's equation for the change in potential using electron charge density found in step 2, 4) generate a new 'output' potential was using under-relaxation, 5) return to step 3 and repeat until tolerance is achieved, 6) generate a new 'input' potential using under-relaxation and finally, 7) return to step 1 and repeat until tolerance is achieved. Ram-Mohan *et. al.* report that their method is very stable for a wide range of parameter values.

This thesis presents a self-consistent method to calculate the band offset due to the redistribution of charge in the presence of a charge confining well (quantum well). We extend our calculation to include the electron charge density both inside and outside the well regions for a semi-conductor device of finite extent using suitable boundary conditions. Our self-consistent method follows the recent work by Ram-Mohan *et. al.* [1], [13], [14]. The method involves determining an expression which relates the carrier charge density to the potential. This carrier charge density $n_e(z)$ along with the charge density of the ionized parent donor or acceptor atoms forms the source term of the Poisson equation. Poisson's equation is solved to 'predict' $n_e(z)$ and $V(z)$ in an inner loop and updated using an under-relaxation method. Once tolerance of the inner loop is achieved we exit the inner loop, update the potential used in the outer loop (the potential functions of the inner and outer are kept separate) using under-relaxation and solve the Schrödinger equation to 'correct' $n_e(z)$. The Schrödinger and Poisson equations are solved at each iteration in this manner until a self-consistent potential is achieved.

The unique features of this thesis include, one, we present a procedure to develop the finite element equations which uses a simple integration by parts. This procedure is applicable to any partial differential equation we wish to solve using the finite element method. Two, for complex geometries we found that the adaptive weighting factor methods could not achieve a self-consistent solution,

thus we confirm that for these problems it is necessary to decouple the Schrödinger and Poisson equations by developing an approximate expression for the charge carrier distribution. Finally, three, we consider 1-D finite devices, bound in one dimension by a potential barrier of arbitrary shape. These boundary conditions approximate vacuum, semiconductor substrates, or metallic connectors.

1.3 Thesis Overview

This thesis is concerned with calculating the energy levels of charge carriers bound inside a one dimensional well (quantum well). This quantum well is created by the conduction or valence band offset between two heterojunctions. At the same time determine how the conduction and valence band edges align at the heterojunctions. The heterostructure devices will be of finite extent and are bound by either vacuum/air or metallic connectors. The energy levels and band offsets will be calculated using a self-consistent solution of the Schrödinger and Poisson equations. Chapter 2 will review the finite element method. Chapter 3 will outline the finite element solution to the Schrödinger and Poisson equations. Chapter 4 will present the formulation of the Schrödinger equation and Poisson equation into a self-consistent solution. Chapter 5 will test the self-consistent algorithm and present the results to several examples of carrier confining heterostructure devices. Conclusions of this thesis will be presented in Chapter 6.

2) Finite Element Method

In this thesis we are concerned with finding solutions to the time-independent Schrödinger and Poisson Equations in one dimension. Both equations are of the same form thus we can develop one general finite element formulation capable of solving both these equations. In this section we will develop the finite element equations required for the self-consistent algorithm. We deviate from the variational procedure presented by Ram-Mohan *et. al.* [1],[13],[14] and adopt a procedure presented by Szabo, Babuska, and Guo [32],[33]. The method presented by Szabo and Babuska, and Guo is simple and more general to apply. It can be applied to any partial differential equation we wish to solve using the finite element method, the underlying assumption being that the partial differential equations describing the problem have been developed through some other means. The resulting finite element equations are identical to those developed by other means.

In this section we will present the standard finite element formulation required to solve for an unknown vector problem (Poisson's equation) and the finite element formulation required to solve for the eigenvalues and eigenfunctions of an eigenvalue problem (Schrödinger equation).

2.1 Problem Statement

Consider the general second order differential equation defined over a domain $\Omega \in \Re^1$,

$$-\nabla^2 \Psi(x) + t(x)\Psi(x) = r(x) \tag{2.1}$$

subject to boundary conditions,

$$\Psi(x)\big|_{\Gamma_D} = c_D$$
$$\left.\frac{d\Psi(x)}{dx}\right|_{\Gamma_N} = c_N \tag{2.2}$$

where $c_{N,D}$ are constants, the one dimensional Laplacian is given by, $\nabla^2 = \frac{d^2}{dx^2}$, and $t(x)$ and $r(x)$ are functions of the coordinate x. Γ_N and Γ_D are the boundaries of Ω and specified by Neumann and Dirichlet boundary conditions respectively.

Numerical Solution.

For most boundary value problems the exact analytical solution is very difficult if not impossible to find except for some very special cases. Typically numerical methods are used to find the solution. Two numerical methods commonly used to solve this type of problem are the finite difference method and the finite element method. Both methods having advantages when compared with the other. The finite difference approach is easy to understand and code while the finite element method is more difficult to understand and code but tends to provide superior results. In the finite difference approach, the solution of the partial differential equation is found at nodal points which are chosen such that they span the domain of the partial differential equation. The value of the derivative of the solution to the partial differential equation is approximated at each nodal point by a finite difference equation [34]. On the other hand with the finite element method, the exact solution is approximated by a flexible trial or test

solution,

$$\Psi_{Exact}(x) \approx \Psi_{F.E.M.}(x) = \sum_{i=1}^{N} \psi_i \theta_i(x) \tag{2.3}$$

where ψ_i are undetermined coefficients and $\theta_i(x)$ are called basis or shape functions which must satisfy the boundary conditions of the problem. The resulting equations are solved to find the best fit, or best trial solution [32],[33],[34],[35], amenable to special bases and higher order.

2.2 Finite Element Formulation

The finite element formulation avoids solution of the original boundary value problem in the partial differential form and seeks the solution of an alternate integral equation representation [36]. Multiplying the original differential equation, equation (2.1), by an arbitrary set of functions $\varphi_i(x)$ and integrating over the domain Ω we obtain the integral equations [32],[33],

$$\int_{\Omega} \left[-\varphi_i(x) \frac{d^2}{dx^2} \Psi(x) + \varphi_i(x) t(x)\ \Psi(x) \right] dx = \int_{\Omega} \varphi_i(x) r(x)\, dx. \tag{2.4}$$

The set of functions $\varphi_i(x)$ are called *test*, or *weighting* functions in the literature.

Strong Solution

In the strong solution we restrict the set of $\varphi_i(x)$ functions to those for which the second derivative exists and which satisfy the boundary conditions. We then seek a solution function $\Psi(x)$ for which the second derivative exists, is continuous, and satisfies the integral equation at every point in Ω and the boundary conditions. The strong solution tends to be a difficult problem to solve [36],[35].

Weak Solution

In the weak formulation we expand the solution set by considering any set of functions $\varphi_i(x)$ having a first derivative and satisfying the boundary conditions. Using integration by parts we can rewrite the integral equation (2.4) as,

$$\int_{\Omega}\left[\tfrac{d}{dx}\varphi(x)\tfrac{d}{dx}\Psi(x)+t(x)\varphi(x)\Psi(x)\right]dx-\varphi(x)\tfrac{d}{dx}\Psi(x)\Big|_{\Gamma_N} = \int_{\Omega}\varphi(x)r(x)\,dx. \tag{2.5}$$

Any function $\Psi(x)$ which satisfies this integral equation is a 'weak' solution to the original differential equation [32],[33]. We call this the weak solution because the set of functions $\varphi_i(x)$, are only required to have a first derivative. This equation is identically equivalent to those developed by variational methods [1],[14],[13],[35], method of weighted residuals [34],[37] and methods of virtual work [32] and can be summarized as projective methods [36].

From equation (2.5), we can define the following terms,

Bilinear Form:

$$B\left(\varphi(x),\Psi(x)\right)=\int_{\Omega}\left[\tfrac{d}{dx}\varphi(x)\tfrac{d}{dx}\Psi(x)+t(x)\varphi(x)\Psi(x)\right]dx \tag{2.6}$$

where $\Psi(x)$ and $\varphi(x)$ are elements of the Hamiltonian space H_D^1 and are square integratable, that is,

$$\Psi(x),\varphi(x)\in H_D^1(\Omega)=\left\{\begin{array}{l}\Psi(x)\big|_{\Gamma_N},\ \Psi(x)\big|_{\Gamma_D}=0\,;\\ \int\left[\left|\tfrac{d}{dx}\Psi(x)\right|^2+\left|\Psi(x)\right|^2\right]d\Omega<\infty\end{array}\right\}. \tag{2.7}$$

Linear Functional:

$$F\left(\varphi(x)\right)=\int_{\Omega}r(x)\varphi(x)dx+\varphi(x)\tfrac{d}{dx}\Psi(x)\Big|_{\Gamma_N}. \tag{2.8}$$

Thus we can define the integral problem of equation (2.5) in terms of a variational

equation and say that we seek a function $\Psi(x) \in H_D^1(\Omega)$ such that,

$$B\left(\varphi(x), \Psi(x)\right) = F\left(\varphi(x)\right) \quad \forall\, \varphi(x) \in H_D^1(\Omega). \tag{2.9}$$

2.3 Solution to the Weak Formulation (Discretization)

The finite element solution to equation (2.9) is obtained by selecting a set of test or weighting functions $\varphi = \varphi_1, \varphi_2, \varphi_3, \ldots \varphi_N$ over some *N*-dimensional subspace S_N, $S_N = span\{\varphi_1, \varphi_2, \varphi_3, \ldots \varphi_N\}$ where, $S_N \subset H_D^1(\Omega)$. In other words the test functions are elements of the subspace S_N which is a proper subset of the Hamiltonian space, $\varphi_i(x) \in S_N \subset H_D^1(\Omega)$.

Recall that in the finite element method we approximate the exact solution by the approximation,

$$\Psi_{Exact}(x) \approx \Psi_{F.E.M.}(x) = \sum_{i=1}^{N} \psi_i \theta_i(x) \tag{2.10}$$

where ψ_i are undetermined coefficients and $\theta_i(x)$ are the basis or shape functions which must satisfy the boundary conditions of the problem. Note that we use the lower case ψ_i to represent the coefficients because these coefficients physically represent the value of the finite element solution $\Psi_{F.E.M.}(x)$ at sampling points. In Galerkin's method the weighting functions are chosen to be the same as the basis or shape functions, $\theta_i(x) = \varphi_i(x)$. This allows us to re-write the variational equation (2.9) in its discrete form,

$$B\left(\sum_{j=1}^{N} \psi_j \varphi_j(x), \varphi_i(x)\right) = F\left(\varphi_i(x)\right);\ i = 1, 2, \ldots, N. \tag{2.11}$$

The bilinear form has the following linearity and commutative properties,

$$\begin{aligned} B\left(c\varphi(x), \theta(x)\right) &= cB\left(\varphi(x), \theta(x)\right) \\ B\left(\theta(x), \varphi(x)\right) &= B\left(\varphi(x), \theta(x)\right) \end{aligned} \tag{2.12}$$

where c is a constant. This allows us to cast equation (2.11) in matrix form, $\mathbf{A}\psi = \mathbf{P}$ [33]:

$$\begin{pmatrix} A_{11} & A_{12} & \cdots & A_{1N} \\ A_{21} & A_{22} & \cdots & A_{2N} \\ \vdots & \vdots & \ddots & \vdots \\ A_{N1} & A_{N2} & \cdots & A_{NN} \end{pmatrix} \begin{pmatrix} \psi_1 \\ \psi_2 \\ \vdots \\ \psi_N \end{pmatrix} = \begin{pmatrix} P_1 \\ P_2 \\ \vdots \\ P_N \end{pmatrix} \tag{2.13}$$

where,

$$A_{ij} = \mathrm{A}\left(\varphi_i(x), \varphi_j(x)\right) = \begin{Bmatrix} \int_\Omega \left[\frac{d}{dx}\varphi_i(x) \frac{d}{dx}\varphi_j(x) + t(x)\varphi_i(x)\varphi_j(x) \right] dx \\ + \varphi_i(x) \frac{d}{dx}\varphi_j(x)\Big|_{\Gamma_N} \end{Bmatrix}, \tag{2.14}$$

$$P_i = \mathbf{P}\left(\varphi_i(x)\right) = \int_\Omega \left[r(x)\varphi_i(x) \right] dx.$$

The finite element method involves solving for the unknown constants ψ_i in Equation (2.13); our algorithms use the IMSL [38] subroutine, DLSARG, which is a double precision solver for a general system of real linear equations with iterative refinement. Refer to Appendix A to see an example of the programming considerations required to implement the procedure presented in this section.

2.4 Choice of the Subdomain S_N

The domain Ω is subdivided into m sub-domains ω_i, $\Omega = \bigcup_{i=1}^{m} \omega_i$. In the one dimensional case the sub-domain is simply a segment of the real axis. Note that these sub-domains or segments do not have to be uniform but must satisfy the following conditions [32][33],

i. Boundaries must lie on a segment endpoint.

ii. Each segment can only contain one type of media.

iii. The intersection of segments, $\omega_i \cap \omega_j$ contain only one vertex (node).

Each segment is referred to as an 'element' in the finite element method.

2.5 Standard Elements

To ensure robustness of the finite element algorithm we choose a standard element which is mapped onto each subdomain ω_i of Ω using a mapping function [36]. Each subdomain contains the same local coordinate system. This enables us to define a standard set of local shape or test functions once and use the mapping function to apply them globally anywhere in the domain Ω. The standard element is defined as, $\Omega_{ST} = \{\xi | -1 < \xi < 1\}$ [32]. Figure 2.1 illustrates the standard element for one dimension.

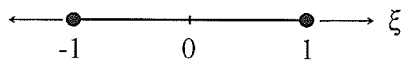

Figure 2.1: Standard Local Element in one dimension.

2.6 Local Shape (test or weight) Functions

For ease of implementation we choose shape functions defined over the local element. This frees us from the difficulty of defining global shape functions over the entire domain and allows us to define the shape functions once over the standard element and then map the functions to each element. We are free to choose any type of local or *element-level* shape functions provided they satisfy the following conditions [21];

i.) It must be possible to map the local shape functions into piecewise and continuous global shape functions. Where by continuous we mean that the local shape functions are chosen such that upon being mapped into the global shape function there are no discontinuities between the shape functions on the boundaries of neighbouring elements. Special local shape functions may be chosen in which the first derivative is also continuous on element boundaries.

ii.) Local shape functions are chosen such that upon being mapped to global shape functions, the final global shape functions have minimal local support. This means that each local shape function is mapped to a global shape function which is non-zero only within the interval of a single element or at most in the interval of two neighbouring elements. The global shape function is zero everywhere else in the domain.

2.7 Hermite Polynomials

For quantum mechanical problems it is convenient to choose Hermite interpolation polynomials as the shape functions [49]. Hermite polynomials allow us to impose first derivative continuity at the nodal points. In quantum mechanics first derivative continuity means that the probability current density is conserved at nodal points and across element interfaces (boundaries) [1],[37]. Hermite polynomials satisfy the following conditions,

i. Each node has two undetermined coefficients.

ii. Each node is identified with two basis functions.

In this thesis we will use quintic Hermite interpolation functions for our basis or shape functions. These functions require that each local element contain three nodal points $\xi_1 = -1, \xi_2 = 0,$ and $\xi_3 = +1$. Each node has two degrees of freedom; one degree for functional continuity and the other for first derivative continuity. Conditions of minimal local support require that only one polynomial per degree of freedom be non-zero at a nodal point. We can represent the finite element solution in the m^{th} element as,

$$\Psi^{(m)}_{F.E.M.}(\xi) = \sum_{n=1}^{3} \psi_n^{(m)} \Theta_n(\xi) + \sum_{n=1}^{3} \psi_n^{(m)\prime}\ \bar{\Theta}_n(\xi) \qquad (2.15)$$

where the bar is used to identify those functions for which the first derivative is continuous at the nodal points. Notice that for those polynomials whose first derivative is continuous at nodal points the undetermined coefficient ψ'_n in the summation is now the value of the derivative of $\Psi_{F.E.M.}$ at that nodal point. Also recall that we chose that the local shape functions $\Theta_i(\xi)$ are the same in every local or standard element.

Six, fifth order Hermite polynomials of the form,

$$\Theta_i(\xi) = a_i + b_i\xi + c_i\xi^2 + d_i\xi^3 + e_i\xi^4 + f_i\xi^5 \;;\; i = 1,..,6, \tag{2.16}$$

are required as our basis functions. We will use the procedure presented by Ram-Mohan [1] and Lapindus and Pinder [37] to derive these. Continuity at the nodal points $\xi = \xi_j,\ j = 1,2,3$ is imposed by satisfying the following conditions,

$$\left\{ \begin{array}{ll} \Theta_i(\xi_j) = \delta_{ij} & \overline{\Theta}_i(\xi_j) = 0 \\ \frac{d}{dx}\Theta_i(\xi_j) = 0 & \frac{d}{dx}\overline{\Theta}_i(\xi_j) = \delta_{ij} \end{array} \right\} \quad \text{for } i = 1,2,3, \tag{2.17}$$

where δ_{ij} is the Diarc delta function. Applying these constraints on the general polynomial of equation (2.16) we can specify a matrix equation to solve for the coefficients. The first matrix contains values of the powers of ξ evaluated at the three nodal points with the rows arranged alternately for $\Theta_i(\xi_j)$ and $\overline{\Theta}'_i(\xi_j)$. The second matrix consists of the undetermined coefficients in the polynomial equation. The product of these two matrices is equal to the identity matrix, as

$$\begin{pmatrix} 1 & -1 & 1 & -1 & 1 & -1 \\ 0 & 1 & -2 & 3 & -4 & 5 \\ 1 & 0 & 0 & 0 & 0 & 0 \\ 0 & 1 & 0 & 0 & 0 & 0 \\ 1 & 1 & 1 & 1 & 1 & 1 \\ 0 & 1 & 2 & 3 & 4 & 5 \end{pmatrix} \begin{pmatrix} a_1 & a_2 & a_3 & a_4 & a_5 & a_6 \\ b_1 & b_2 & b_3 & b_4 & b_5 & b_6 \\ c_1 & c_2 & c_3 & c_4 & c_5 & c_6 \\ d_1 & d_2 & d_3 & d_4 & d_5 & d_6 \\ e_1 & e_2 & e_3 & e_4 & e_5 & e_6 \\ f_1 & f_2 & f_3 & f_4 & f_5 & f_6 \end{pmatrix} = \mathbf{I}. \tag{2.18}$$

Solving for the coefficients we obtain the quintic Hermite polynomials,

$$\begin{aligned}
\Theta_1(\xi) &= \xi^2 - \tfrac{5}{4}\xi^3 - \tfrac{1}{2}\xi^4 + \tfrac{3}{4}\xi^5 \\
\Theta_2(\xi) &= \tfrac{1}{4}\xi^2 - \tfrac{1}{4}\xi^3 - \tfrac{1}{4}\xi^4 + \tfrac{1}{4}\xi^5 \\
\Theta_3(\xi) &= 1 - 2\xi^2 + \xi^4 \\
\Theta_4(\xi) &= \xi - 2\xi^3 + \xi^5 \\
\Theta_5(\xi) &= \xi^2 + \tfrac{5}{4}\xi^3 - \tfrac{1}{2}\xi^4 - \tfrac{3}{4}\xi^5 \\
\Theta_6(\xi) &= -\tfrac{1}{4}\xi^2 - \tfrac{1}{4}\xi^3 + \tfrac{1}{4}\xi^4 + \tfrac{1}{4}\xi^5
\end{aligned} \tag{2.19}$$

defined with respect to the local coordinates of the standard element. These are shown in Figures 2.2 and 2.3.

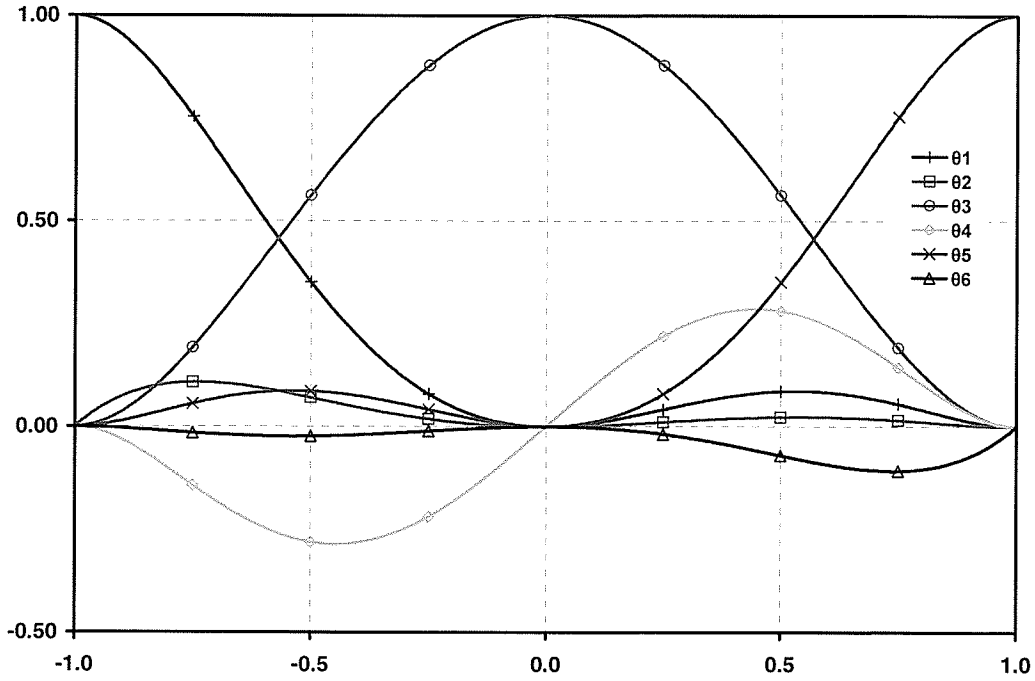

Figure 2.2: Quintic Hermite Polynomials in the Standard Local Element.

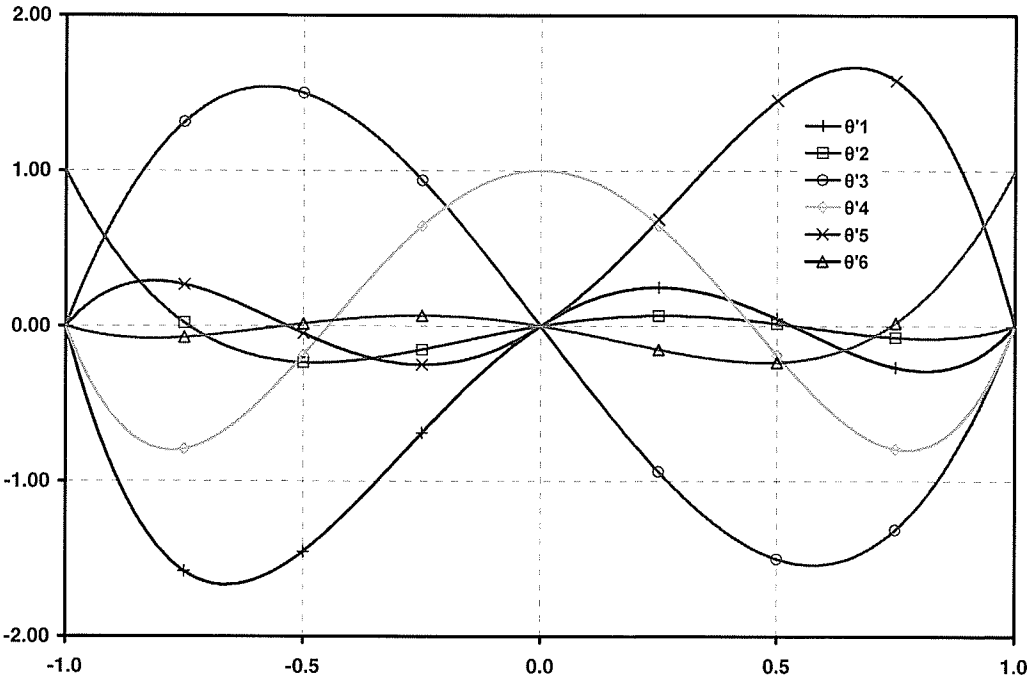

Figure 2.3: First Derivative of the Quintic Hermite Polynomials in the Standard Local Element.

2.8 Mapping

In our finite element implementation two maps are required. The first is a mapping between local and global coordinates. The second is a mapping between local and global shape functions.

Coordinate Mappings:

Points on the standard or local element are mapped to the global domain via a mapping function. For the one dimensional problem this function is of the form [32],

$$M^{(m)}: \quad \{x = X(\xi) = \tfrac{1}{2}(1-\xi)x_1^{(m)} + \tfrac{1}{2}(1+\xi)x_2^{(m)} \tag{2.20}$$

where x is the mapped global coordinate corresponding to the local coordinate ξ of the m^{th} element; $x_1^{(m)}$ and $x_2^{(m)}$ are the global coordinates of the 'end-points' of the m^{th} element. Note that element end-points correspond to the local coordinates $\xi_1 = -1$ and $\xi_3 = +1$. As this mapping function is one-to-one (not all mapping functions are) an inverse mapping function can be found and is given by,

$$M^{(m)^{-1}}: \quad \left\{\xi = \Xi(x) = \frac{2x - x_1^{(m)} - x_2^{(m)}}{x_2^{(m)} - x_1^{(m)}}. \right. \tag{2.21}$$

Shape Function Mappings:

Local shape functions must be mapped to global shape functions in order to construct the global matrix equation (2.13). Typically the mapping of the shape functions will depend upon the choice of the local shape functions, however, the technique used to develop a mapping does not change. Consider the quintic Hermite polynomials of Section 2.7 specified over a two element system. Recall that for this type of shape function there are six shape functions per element, two per nodal point indexed by a subscript. We indicate which element each shape

function is associated with by the superscript number in brackets. Figure 2.4 illustrates the local shape functions of the two element system. It can be seen that for the common node of the two elements, the shape functions are the same. That is $\theta_5^{(1)} = \theta_1^{(2)}$ and $\theta_6^{(1)} = \theta_2^{(2)}$. This means that the total number of global shape functions or degrees of freedom for this example is ten. A table mapping the local shape functions to the global shape functions can be developed. A table is for the two element system example here is presented in Table 2.1. An algorithm can be developed to populate the mapping table for any number of elements and a given type of shape functions.

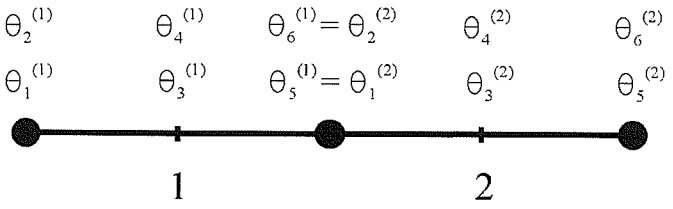

Figure 2.4: Mapping local shape functions to global shape functions for a two element system.

Table 2.1: Shape Function Mapping Table

Local Shape Function Index	Element Number	Global Shape Function Index
1	1	1
2	1	2
3	1	3
4	1	4
5	1	5
6	1	6
1	2	5
2	2	6
3	2	7
4	2	8
5	2	9
6	2	10

Finally we need to define the complete finite element solution in terms of the local shape functions. We are required to represent the global solution function $\Psi_{F.E.M.}(x)$ in an element interval $x \in [a, b]$ in terms of the superposition of standard local shape functions $\varphi_i(\xi)$ defined in a standard element of interval $\xi \in [-1, 1]$. The global coordinate x is mapped into the local coordinate ξ using the mapping functions presented at the beginning of this section. This implies that we should write the finite element solution of 2.10 as,

$$\Psi^{(m)}_{F.E.M.}(x) = \sum_i \psi_i \theta_i \left(X(\xi) \right) = \sum_n \psi_n \Theta_n \left(\xi(x) \right) + \sum_n \psi'_n \bar{\Theta}_n \left(\xi(x) \right) \frac{dx}{d\xi} \quad \textbf{(2.22)}$$

where $\frac{dx}{d\xi}$ is a scaling constant which is required to ensure that the derivative of

the global functions evaluated at the node points x_i are, $\left.\frac{d\Psi(x)}{dx}\right|_{x_i} = \psi_i'$. From the mapping function we can arrive at an expression for this scale function in each element as,

$$\frac{dx}{d\xi}^{(m)} = \frac{x_2^{(m)} - x_1^{(m)}}{2}. \tag{2.23}$$

For simplicity we include this scale factor in the local derivative continuity shape functions to get,

$$\begin{aligned}
\Theta_1(\xi) &= \xi^2 - \tfrac{5}{4}\xi^3 - \tfrac{1}{2}\xi^4 + \tfrac{3}{4}\xi^5, \\
\Theta_2(\xi) &= \left(\tfrac{1}{4}\xi^2 - \tfrac{1}{4}\xi^3 - \tfrac{1}{4}\xi^4 + \tfrac{1}{4}\xi^5\right)\frac{dx}{d\xi}, \\
\Theta_3(\xi) &= 1 - 2\xi^2 + \xi^4, \\
\Theta_4(\xi) &= \left(\xi - 2\xi^3 + \xi^5\right)\frac{dx}{d\xi}, \\
\Theta_5(\xi) &= \xi^2 + \tfrac{5}{4}\xi^3 - \tfrac{1}{2}\xi^4 - \tfrac{3}{4}\xi^5, \\
\Theta_6(\xi) &= \left(-\tfrac{1}{4}\xi^2 - \tfrac{1}{4}\xi^3 + \tfrac{1}{4}\xi^4 + \tfrac{1}{4}\xi^5\right)\frac{dx}{d\xi}.
\end{aligned} \tag{2.24}$$

2.9 Eigenvalue Problems

In the previous sections we considered a Poisson type description of the form described by equation (2.1) and developed a finite element method numerical approach for its solution. Schrödinger's equation requires us to consider equations of the form,

$$-\nabla^2\Psi(x)+t(x)\Psi(x)=\lambda\Psi(x), \tag{2.25}$$

where λ is an undetermined constant. This is an eigenvalue problem with a solution $\Psi(x)$ referred to as an eigenfunction and λ as an eigenvalue. The integral form of equation 2.25 can be derived following the the same procedure as in Section 2.2. Multiplying equation 2.25 by a weighting function, integrating over the space, and using integration by parts, we arrive at,

$$\begin{aligned}\int_\Omega \left[\tfrac{d}{dx}\varphi(x)\tfrac{d}{dx}\Psi(x)+t(x)\varphi(x)\Psi(x)\right]dx-\varphi(x)\tfrac{d}{dx}\Psi(x)\Big|_{\Gamma_N}\\ =\lambda\int_\Omega \varphi(x)\Psi(x)\,dx.\end{aligned} \tag{2.26}$$

Using the procedure of Section 2.3 and employing Galerkin's method we can formulate the matrix equation, $\mathbf{A}\psi=\lambda\mathbf{D}\psi$:

$$\begin{pmatrix} A_{11} & A_{12} & \cdots & A_{1N} \\ a_{21} & a_{22} & \cdots & A_{2N} \\ \vdots & \vdots & \ddots & \vdots \\ A_{N1} & A_{N2} & \cdots & A_{NN} \end{pmatrix}\begin{pmatrix}\psi_1\\ \psi_2\\ \vdots\\ \psi_N\end{pmatrix}=$$

$$\begin{pmatrix}\lambda_1 & \lambda_2 & \cdots & \lambda_N\end{pmatrix}\begin{pmatrix} D_{11} & D_{12} & \cdots & D_{1N} \\ D_{21} & D_{22} & \cdots & D_{2N} \\ \vdots & \vdots & \ddots & \vdots \\ D_{N1} & D_{N2} & \cdots & D_{NN} \end{pmatrix}\begin{pmatrix}\psi_1\\ \psi_2\\ \vdots\\ \psi_N\end{pmatrix} \tag{2.27}$$

where,

$$A_{ij} = A\left(\varphi_i(x), \varphi_j(x)\right) = \left\{ \begin{array}{l} \int_{\Omega} \left[\frac{d}{dx}\varphi_i(x) \frac{d}{dx}\varphi_j(x) + t(x)\varphi_i(x)\varphi_j(x) \right] dx \\ + \varphi_i(x) \frac{d}{dx}\varphi_j(x)\Big|_{\Gamma_N} \end{array} \right\}, \quad \textbf{(2.28)}$$

$$D_{ij} = D\left(\varphi_i(x), \varphi_j(x)\right) = \int_{\Omega} \left[\varphi_i(x)\varphi_j(x) \right] dx.$$

Choice of subdomain, local elements, shape functions, and mappings remain the same as in Sections 2.4 -2.8. Solution to the eigenvalue problem involves solving for the N unknown eigenvalues λ_i and wave functions ψ_j for equation (2.27). Our algorithms will use the IMSL [38] double precision subroutine DGVLCRG which computes all the eigenvalues and eigenfunctions of a generalized real eigensystem. Refer to Appendix B to see an example of the programming considerations required to implement the procedure presented in this section.

3) Carrier Confinement in Heterostructure Devices

In this section we examine carrier confinement in semiconductor heterostructure devices. Here we will present the equations which are solved using the finite element method. The first part presents the solution of Schrödinger's equation for wave functions and energy levels. This equation is solved within the effective mass approximation and reduces to solving the Schrödinger equation for an envelope function [1],[39],[17]. In the effective mass approximation the related Schrödinger equation is macroscopic. For the single-band approximation these effective parameters are given in Section 2.3. The simplest heterostructure created is the quantum well consisting of the layers AlGaAs/GaAs/AlGaAs.

The distribution of charges within the heterosturcture device gives rise to a potential which 'bends' the bulk conduction band structure. The amount of this bending is considered by solving the Poisson equation for change in potential. This involves solving for the distribution of charges inside of the heterostructure. In the second part will present Poisson's equation in a variational form and in part three develop the necessary equations required to determine the charge distribution.

3.1 Energy Band Structure

Electrons in infinite crystals are found to have energies which are arranged in *energy bands* separated by forbidden regions. The energy band is a continuum of energies which the electron can have and is bound by a minimum and maximum energy. The electron can not have energies which are outside of the energy band. These forbidden energy regions are called energy gaps or *band gaps*. The location and size of the energy bands and energy gaps depend on the type of semiconductor material. Electrons in a crystal will occupy energy states starting from those in the lowest energy bands first and then proceed to occupy the energies in higher energy bands.

Semiconductor physics is interested in the last filled energy bands; it is these bands which determine the electrical properties of the material. A semiconductor material is one in which one or two bands are either slightly filled or slightly empty. A slightly filled band is referred to as a conduction band while a slightly empty band is referred to as the valence band. The lowest point in the conduction band is called the *conduction band edge* and the highest point in the valence band is called the *valence band edge*.

In this thesis, even though the approach is general to any semiconductor composition, we consider a semiconductor composed of GaAs/AlGaAs due to the abundance of literature to compare our results against. Ga is a Group III element, meaning it has three valence electrons; As is a Group V element, having five valence electrons. These materials bond together in a zincblende structure, sharing their valence electrons to completely fill their valence bands. GaAs has a large band gap of 1.424 eV. By replacing a small percentage of the Ga with another Group III element such as Al (forming $Al_xGa_{1-x}As$) we can change the size of the energy band gap. The band gap is also know to depend upon the temperature of the semiconductor material.

3.2 Creation of Charge Carriers

There are three simple ways in which charge carriers are created. All three methods require some type of excitation energy for the charge carriers to be created. Examples of this excitation can be light, applied electric potential or thermal excitation at a finite temperature.

The first is the creation of an electron - hole pair, in which an electron from the valence band is excited into the conduction band. The charge carrier can be the electron, the hole, or both the electron and hole. In this thesis we are assuming that this mechanism is not very likely and thus is not considered in our analysis.

The second is to excite an electron from an impurity energy level into the conduction band. An electron from the donor or impurity atom is weakly bound in the impurity energy state which lies "just" below the conduction band edge. The donor atom is ionized and the weakly bound electron is excited into the conduction band. The charge carrier is the electron since the hole is bound to the site of the donor atom. In GaAs donor atoms can be created by replacing some of the Ga atoms with a Group IV element like Si or Se [23],[24]. The weakly bound electron is in an energy state just below the conduction band edge.

The third is to excite an electron from the valence band into an acceptor energy level. In this case an acceptor atom has an acceptor energy state which lies "just" above the valence band edge. The electron from the valence band is excited into the impurity energy level to ionize the impurity atom. In this case the charge carrier is the hole since the electron is bound to the site of the acceptor atom. In GaAs acceptor atoms can be created by replacing some of the Ga atoms with a Group II element like Zn or Cd [23],[24].

3.3 Semiconductor Heterostructure

A heterostructure is a semiconductor structure in which the chemical composition of the material changes with position usually in a layered manner. The effect of changing the chemical composition with position is to change the size of the energy gap with position over the semiconductor [25],[26]. This implies that the band-edge profile varies with position throughout the semiconductor. The advantage of a heterostructure is that it offers precise control over the states and dynamics of the charge carriers. A unique feature of a heterostructure is that the fate of the electrons and holes are not related in the sense that their respective conduction channels can be separated. In this thesis we will consider the simplest heterostructure, a heterojunction between GaAs and AlGaAs. A heterojunction is a structure in which the chemical composition changes abruptly across a boundary.

A key problem in the modelling of a heterojunction is determining the alignment of the band edges. Typically the conduction and valence band edges do not align across a heterojunction. Usually there is some offset between the conduction band edges ΔE_C and the valence band edges ΔE_V, of the different materials. This is illustrated in Figure 3.1. To date there remains significant uncertainties in band alignments of many heterojunction systems. Several theories and indirect experimental measurements have been developed and are presented in the literature, often appearing to disagree depending upon the measurement technique and crystal structure [27],[28],[29],[30]. For example it has been found that band alignment depends rather sensitively on strain. In this thesis we will use the same band alignments presented in the literature when comparing our results to others. Otherwise, for $Al_xGa_{1-x}As/GaAs$ in the direct-gap range, we will use the band edge alignments experimentially estimated in Frensley[27], $\Delta E_C = 0.77x$ and $\Delta E_V = 0.48x$ for the conduction and valence band offsets respectively. Here, 'x' is the amount of Ga replaced by Al (in percent).

Consider a simple one dimensional heterostructure device created by three layers of semiconductor material. Two heterojunctions are created in which the

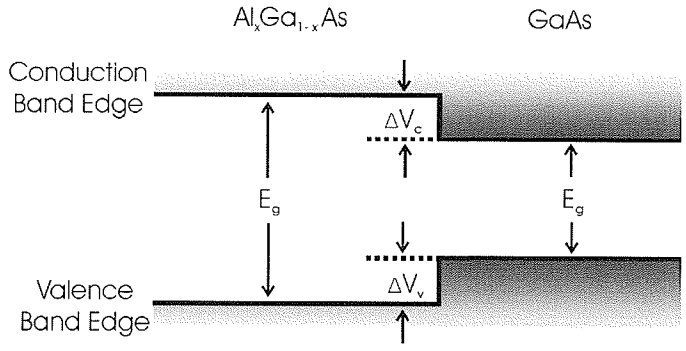

Figure 3.1: Band-edge misalignment between AlGaAs and GaAs. Note the different band gaps of the two materials. The shaded grey represents continuum energy states.

semiconductor material is changed abruptly from AlGaAs to GaAs and then back to AlGaAs, Figure 3.2. The conduction and valence band edge offsets of this layered heterostructure device form a 'well' which can capture free charge carriers. Conduction electrons in the conduction band of the AlGaAs can aquire a lower energy by "sliding down" from the conduction band of AlGaAs into the conduction band quantum well of GaAs. Likewise a conduction hole in the valence band of AlGaAs can acquire a lower energy by "sliding up" from the valence band in AlGaAs into the valence band quantum well of GaAs. These quantum wells form conduction channels.

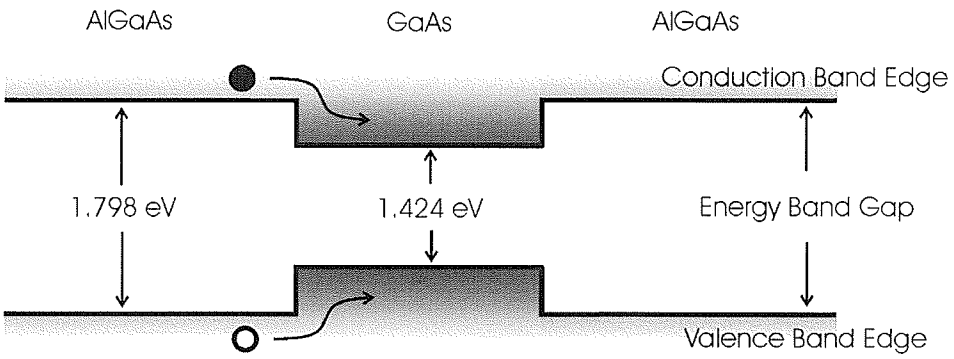

Figure 3.2: A carrier confining well (quantum well) created by the two heterojunctions of three semiconductor materials with an Al concentration x = 0.3. Note that there are two quantum wells, one created by the conduction band offset and the other created by the valence band offset.

Figure 3.2 illustrates one of the advantages of modern heterostructure manufacturing which leads to wave function engineering. With the advent of molecular beam epitaxy (MBE) it is possible to separate the conduction channel (GaAs or well region) from the location of the impurity donor or acceptor atoms (AlGaAs or barrier region)[1],[14]. Thus a quantum well heterostructure can be grown in which only the barrier regions are doped with impurities. This means that any charge carriers which were initially bound to the impurity atom will seek lower energy states and 'fall' into the quantum well. The separation of the charge carrier in the well from its parent atom in the barrier region means that there is a reduction in the scattering of the charge carriers off of the ionized impurity atoms. The advantage of such a layered heterostructure device is improved mobility of the charge carriers. For example, electron mobilities of 4×10^6 cm^2/Vs have been achieved in quantum well structures compared with typical mobilities of 10^5 cm^2/Vs in bulk semiconductors[1] (this allows the development of faster devices). In two dimensions this quantum well heterostructure device is referred to as a *quantum wire*.

3.4 Single Band Schrödinger Equation

Assume that we have a one dimensional heterostructure with the material layers normal to the z-direction as shown in Figure 3.3. (the device is infinite in extent in the xy-plane). In the one dimensional structure electrons are free in the xy-plane (in-plane direction). In the envelope function approximation, the single band Schrödinger equation for the electron wave function $\Psi(\mathbf{r})$ of the conduction band is given by [1],[13],[4], [22],

$$-\frac{\hbar^2}{2m_o}\nabla\left(\frac{1}{m^*(\mathbf{r})}\nabla\Psi(\mathbf{r})\right)+V(\mathbf{r})\Psi(\mathbf{r})=E\Psi(\mathbf{r}) \tag{3.1}$$

where $\hbar$ is the reduced Planck constant, m_0 is the electron rest mass, $m^*(\mathbf{r})$ is the position dependent dimensionless electron effective mass, $V(\mathbf{r})$ is the potential energy and E is the energy eigenvalue. The potential energy is the superposition of the heterostructure's bulk band potential energy $V_{bulk}(z)$ and the potential which arises from the presence of ionized donors and their free electrons $V_{chrg}(z)$,

$$V(z)=V_{bulk}(z)+V_{chrg}(z). \tag{3.2}$$

The bulk potential is given by,

$$V(z)=\begin{cases}V_0; & \text{for } z\le\frac{-\ell}{2} \text{ and } \quad z\le\frac{\ell}{2}\\ 0; & \text{for } \frac{-\ell}{2}<z<\frac{\ell}{2}\end{cases} \tag{3.3}$$

where ℓ is the width of the well. The bulk band potential is illustrated in Figure 3.3. The dimensionless effective mass is assumed to change abruptly at the well interfaces,

$$m(z) = \begin{cases} m^*_{barrier}\ m_0 & z < -\frac{\ell}{2} \\ m^*_{well}\ m_0 & -\frac{\ell}{2} < z < -\frac{\ell}{2} \\ m^*_{barrier}\ m_0 & z > \frac{\ell}{2} \end{cases} \tag{3.4}$$

where $m^*_{barrier}$ and m^*_{well} represent the dimensionless effective mass of the hole or electron in the barrier or well region, respectively.

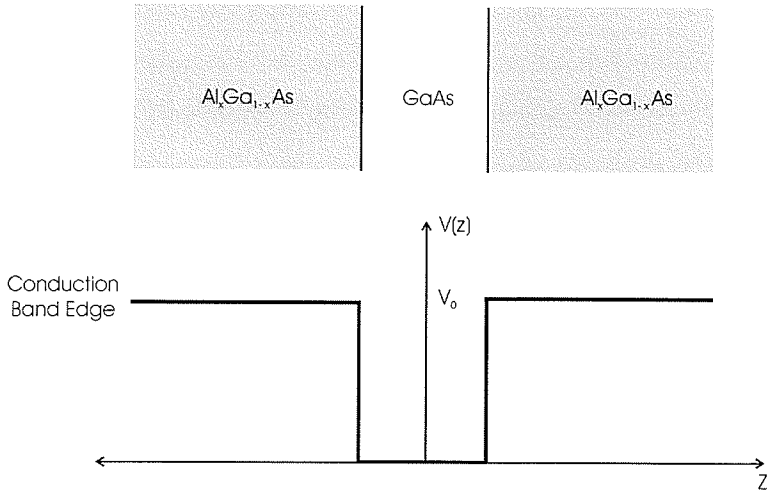

Figure 3.3: One dimensional layered heterostructure device. Semiconductor layers (xy-plane) run in and out of the page and up and down. The z-direction runs left and right as indicated.

For the 1-D heterostructure, the three-dimensional electron wave function can be written as [13],[14],

$$\Psi(\mathbf{r}) = \tfrac{1}{L} e^{ik_x x} e^{ik_y y} \mathrm{Z}(z) \tag{3.5}$$

where L is the period of wave function in the xy-plane and is the result of normalizing the wave function in the xy-direction. Substituting equation (3.5) into (3.1) yields a 1-D Schrödinger equation as a function of the normal plane wave-vectors $k_\perp^2 = k_x^2 + k_y^2$, as

$$-\frac{\hbar^2}{2m_o}\frac{d}{dz}\left(\frac{1}{m^*(z)}\frac{d}{dz}\mathrm{Z}(z)\right)+\frac{\hbar^2 k_\perp^2}{2m_o}\mathrm{Z}(z)+V(z)\mathrm{Z}(z)=E_{k_\perp}\,\mathrm{Z}(z). \tag{3.6}$$

Using the techniques developed in Chapter 2 we can cast equation (3.6) in a variational form, as

$$\begin{aligned}\int_\Omega \frac{1}{m^*(\xi)}\frac{d}{d\xi}\varphi_n(\xi)\frac{d}{d\xi}\mathrm{Z}(\xi)\,d\xi - \varphi_n(\xi)\frac{1}{m^*(\xi)}\frac{d}{d\xi}\mathrm{Z}(\xi)\Big|_a^b \\ +\frac{2m_0\ell^2V_0}{\hbar^2}\int_\Omega \varphi_n(\xi)\left(\frac{\hbar^2k_\perp^2}{2m_0V_0}+v(\xi)\right)\mathrm{Z}(\xi)\,d\xi \\ =\frac{2m_0\ell^2V_0}{\hbar^2}\,\lambda\int_\Omega \varphi_n(\xi)\mathrm{Z}(\xi)\,d\xi,\end{aligned} \tag{3.7}$$

where $E = V_0\lambda$ and $V(\xi) = V_0 v(\xi)$. Subsequently this can be written in matrix form $\mathbf{A}\psi = \lambda\mathbf{D}\psi$ where,

$$A_{ij} = \int_{\Omega} \left[\frac{1}{m^*(\xi)} \frac{d}{d\xi} \varphi_i(\xi) \frac{d}{d\xi} \varphi_j(\xi) + \frac{2m_0 \ell^2 V_0}{\hbar^2} \varphi_i(\xi) \left(\frac{\hbar^2 k_\perp^2}{2m_0 V_0} + v(\xi) \right) \varphi_j(\xi) \right] d\xi$$

$$- \varphi_i(\xi) \frac{1}{m^*(\xi)} \frac{d}{d\xi} \varphi_j(\xi) \Big|_a^b \qquad \textbf{(3.6)}$$

$$D_{ij} = \frac{2m_0 \ell^2 V_0}{\hbar^2} \lambda \int_{\Omega} \varphi_i(\xi) \varphi_j(\xi) \, d\xi$$

$$\psi_i = \mathrm{Z}(\xi_i)$$

and we solve for the unknown eigenvector ψ and eigenvalue λ. We will choose a procedure where $k_\perp$ is incremented for values ranging from 0 to a maximum value at which the contribution to the charge distribution becomes negligible.

The boundary conditions are specified so that the wave function and its first derivative (current density distribution) are continuous across the well/barrier interface. When considering the boundary condition for the first derivative at the interface, however, there is a subtlety we must consider. The boundary condition for the first derivative is derived from enforcement of the conservation of current density across the interface. For the time-independent Schrödinger equation the current density distribution function is given by [40],[41],

$$j(z) = \frac{\hbar}{2m\, i} \left(\Psi_1^*(z) \frac{\partial \Psi_2(z)}{\partial z} - \frac{\partial \Psi_2^*(z)}{\partial z} \Psi_1(z) \right) \qquad \textbf{(3.9)}$$

where the * represents the complex conjugate and Ψ_1 is the wave function in the medium 1 and Ψ_2 is the wave function in the medium 2.

Boundary conditions on the wave function also require that inside the barrier regions the wave function satisfies $\psi(z) \to 0$ as $z \to \pm\infty$. At the interface between semiconductor layers boundary conditions are,

$$\Psi_1 = \Psi_2$$
$$\frac{1}{m_1}\frac{d\Psi_1}{dz} = \frac{1}{m_2}\frac{d\Psi_2}{dz}, \tag{3.10}$$

where the index indicates which medium the wave function is in. Refer to Appendix C to see an example of the programming considerations necessary to apply these boundary conditions.

3.5 The Poisson Equation

The Poisson's equation for the electrostatic potential $\phi_{chrg}(\mathbf{r})$ is given by,

$$\nabla\left[\varepsilon(\mathbf{r})\nabla\phi_{chrg}(\mathbf{r})\right]=-\rho_{chrg}(\mathbf{r}), \tag{3.11}$$

where $\varepsilon(\mathbf{r})$ is the permittivity and $\rho_{chrg}(\mathbf{r})$ is the charge distribution. For a 1-D heterostructure we assume that the barrier layers have uniform doping, hence the potential energy is not a function of the in-plane *(x, y)* coordinates. Employing dimensionless units in terms of the well width ℓ, $z=\ell\xi$ and defining a relative permittivity $\varepsilon=\varepsilon_r\varepsilon_0$, we transform equation (3.11),

$$\frac{d}{d\xi}\left[\varepsilon_r(\xi)\frac{d}{d\xi}\phi_{chrg}(\xi)\right]=-\frac{\ell^2}{\varepsilon_o}\rho_{chrg}(\xi). \tag{3.12}$$

Equation (3.12) can be cast in terms of a potential energy by multiplying by the electric charge -|e|: $-|e|\phi(\xi)\rightarrow V(\xi)$. Scaling by the barrier potential of the square well, results in a Poisson equation for the scaled potential function $v(\xi)$,

$$\frac{d}{d\xi}\left[\varepsilon_r(\xi)\frac{d}{d\xi}v_{chrg}(\xi)\right]=|e|\frac{\ell^2}{\varepsilon_o V_o}\rho_{chrg}(\xi). \tag{3.13}$$

The charge distribution term is due to ionized donors and conduction electrons,

$$\rho_{chrg}(\xi)=\rho_d(\xi)-\rho_e(\xi). \tag{3.14}$$

We define a source term due to the ionized donor atoms as,

$$S_d(\xi)=|e|\frac{\ell^2}{\varepsilon_o V_o}\rho_d(\xi) \tag{3.15}$$

and similarly a source term due to conduction electrons as,

$$S_e(\xi) = -|e| \frac{\ell^2}{\varepsilon_o V_o} \rho_e(\xi). \tag{3.16}$$

Using the techniques developed in Chapter 2 we can cast equation (3.13) in a variational form,

$$\begin{aligned} \int_\Omega \varepsilon_r(\xi) \frac{d}{d\xi} \varphi_n(\xi) \frac{d}{d\xi} v_{chrg}(\xi)\, d\xi - \varphi_n(\xi) \varepsilon_r(\xi) \frac{d}{d\xi} v_{chrg}(\xi) \Big|_a^b \\ = -\int_\Omega \varphi_n(\xi) \left[S_d(\xi) + S_e(\xi) \right] d\xi. \end{aligned} \tag{3.17}$$

Using Galerkin's method equation (3.17) can be solved as a matrix equation of the form $\mathbf{Av} = \mathbf{F}$ where,

$$\begin{aligned} A_{ij} &= \int_\Omega \varepsilon_r(\xi) \frac{d}{d\xi} \varphi_i(\xi) \frac{d}{d\xi} \varphi_j(\xi) d\xi - \varphi_i(\xi)\, \varepsilon_r(\xi) \frac{d}{d\xi} \varphi_j(\xi) \Big|_a^b, \\ F_{ij} &= -\int_\Omega \varphi_i(\xi) \left[S_d(\xi) + S_e(\xi) \right] d\xi, \\ v_i &= v_{chrg}(\xi_i) \end{aligned} \tag{3.18}$$

and we solve for the unknown vector $\mathbf{v}$.

3.6 Source Terms

In this section we develop a method to determine the charge distribution inside the heterostructure from the wave function solution of the Schrödinger equation. We limit our treatment to electrons donated from the donor atoms alone. This is a low temperature approximation in which the thermal energy is not enough to excite electrons from the valence band into the conduction band. For AlGaAs this low temperature approximation holds up to about 300 K.

To determine the electron charge distribution we count the number of occupied bound states and then determine the spacial distribution of the corresponding electrons. The spacial distribution is determined from the wave function of the electron, where $\left|\Psi^{*}_{n_x,n_y,n_z}(x,y,z)\cdot\Psi_{n_x,n_y,n_z}(x,y,z)\right|$ is a probability distribution function which gives the probability of finding a particle (electron in this case) with quantum state E_{n_x,n_y,n_z} inside an infinitesimal volume dr^3 centred at the point (x, y, z) [40], [42]. The Fermi distribution function **F** gives the probability that the conduction band state E_{n_x,n_y,n_z} is occupied [23],[26],[43],

$$\mathbf{F}\ (E,E_f,T)=\begin{cases}\Theta\left(E_f-E\right); & \text{for } T=0K,\\ \dfrac{1}{\exp\left(\left.(E-E_f)\right/k_BT\right)+1}; & \text{for } T\neq 0K.\end{cases} \tag{3.19}$$

where $\Theta(E_F-E)$ is the Heaviside step function, $E_{n_x,n_y,n_z}=E$, E_f is the Fermi Energy, T is the temperature and, k_B is Boltzmann's constant. With these definitions we can write an expression for the density of electrons in the heterostructure,

$$n_e(x,y,z)=2\sum_{n_x,n_y,n_z}\left|\Psi^{*}_{n_x,n_y,n_z}(x,y,z)\cdot\Psi_{n_x,n_y,n_z}(x,y,z)\right|\mathbf{F}\ \left(E,E_f,T\right) \tag{3.20}$$

where the sum extends over all allowed quantum numbers (states) [1]. The factor

of 2 takes into account the spin degeneracy of the electron.

Equation (3.20) involves a sum over single-particle states. The procedure to carried out this summation typically introduces the notion of the *density of states,* $\mathbf{D}(E)$ [40],[42] where such equations are rewritten as an integral over energy. Our equation would be of the form,

$$n_e = \int \mathbf{D}(E) \left| \Psi^*(\mathbf{r}) \Psi(\mathbf{r}) \right| \mathbf{F}(E, E_f, T) dE. \tag{3.21}$$

Deriving an expression for the density of states requires that the energy dispersion relation $E(\mathbf{k})$ be known. In general an analytical expression for the dispersion relation is not known. We will adopt the method similar to that presented by Ram-Mohan, Yoo, and Moussa [1],[13],[14].

We assume that the motion of the electron in the xy-plane is that of a free particle subject to periodic boundary conditions. Thus the energy states in the xy-plane can be characterized as a continuum of states. Thus in equation (3.20) the summation over discrete states n_x and n_y can be replaced by continuous states $\sum_{n_x} \rightarrow \int dn_x$ and $\sum_{n_y} \rightarrow \int dn_y$ [42]. Using the periodic boundary conditions $k_x, k_y = \frac{2\pi n_{x,y}}{L}$ we can derive a relationship between n and k [26]. Finally substituting the wave function equation (3.5) into (3.20) we get,

$$n_e(z) = 2 \int \frac{dk_x dk_y}{(2\pi)^2} \sum_{n_z = v} \left| \mathrm{Z}_v(z) \right|^2 \mathbf{F}\left(E_v, E_f, T\right), \tag{3.22}$$

where $E \rightarrow E_{n_z} = E_v$. The integral $\iint dk_x dk_y$ represents an 'area' in xy-momentum space. Assuming that the states are evenly distributed over momentum space, the area in momentum space will be related to the number of

states. Each set of values (k_x, k_y) form one lattice point in momentum space and correspond to one quantum state. It is easily seen that for a uniform density of states, one unit of area in momentum space corresponds to one state.

A more useful quantity to work with is $k_\perp$ because 'curves' of constant energy can be defined by this parameter alone (here $\perp$ refers to the direction at perpendicular to the z direction). The total number of states inside a ring of $k_\perp$ to $k_\perp + dk_\perp$ will be the area of the ring $2\pi k_\perp dk_\perp$ divided by the unit of area associated with one lattice point. Thus we can write equation (3.22) as,

$$n_e(z) = 2\int \frac{k_\perp dk_\perp}{2\pi} \sum_{n_z = v} \left|\mathrm{Z}_v(z)\right|^2 \mathbf{F} \quad \left(E_v, E_f, T\right). \tag{3.23}$$

Using the same procedure set out by Moussa, Yoo and Ram-Mohan [13],[14] we will evaluate equation (3.23) by breaking up the momentum space into a number of small bins of size $\Delta k_\perp$ (note that each bin actually corresponds to a 'thin' ring in momentum space). Within each 'bin' we will assume that the wave function $Z_v(z)$ and corresponding energy eigenvalue E_v are constant and can be found by solving the Schrödinger equation at a discrete value of $k_\perp$ located at the centre of each bin. In this approximation the integral over the momentum within each bin is constant. Summing over a number of discrete positive values of $k_\perp$ yields,

$$n_e(z) = \frac{\Delta k_\perp}{2\pi} \sum_{k_\perp} \sum_{v} \frac{\left(2k_\perp + \Delta k_\perp\right)\left|\mathrm{Z}_v(z)\right|^2}{1 + \exp\left(\dfrac{E_v - E_f}{k_B T}\right)} \tag{3.24}$$

where at each value of $k_\perp$ the Schrödinger equation is solved for the wave function and corresponding energy eigenvalue. Thus we can write the charge

distribution as,

$$\rho_e(z) = -|e| \frac{\Delta k_\perp}{2\pi} \sum_{k_\perp} \sum_{v} \frac{(2k_\perp + \Delta k_\perp)|Z_v(z)|^2}{1+\exp\left(\frac{E_v - E_f}{k_B T}\right)} \tag{3.25}$$

or as a source term,

$$S_e(z) = \frac{-|e|^2 \ell_o^2}{\varepsilon_o V_o} \frac{\Delta k_\perp}{2\pi} \sum_{k_\perp} \sum_{v} \frac{(2k_\perp + \Delta k_\perp)|Z_v(z)|^2}{1+\exp\left(\frac{E_v - E_f}{k_B T}\right)}. \tag{3.26}$$

Next we develop a method to determine the charge distribution resulting from the ionized donor atoms inside the heterostructure. Starting from the Fermi Distribution function for donors we can calculate the probability that an electron is in the donor band [26],[25],[23],

$$P(E_{Donor}) = \frac{1}{1+ {}^1\!/_{g_d} \exp\left(\frac{E_{Donor} - E_f}{k_B T}\right)} \tag{3.27}$$

where E_{Donor} is the energy level of a donor electron when bound to its parent atom and g_d is the degeneracy of the donor states . The donor energy level lies just below the conduction band edge and is typically presented as, $E_{Donor} = V_{total}(z) - E_d$. Where $V_{total}(z)$ is the total conduction band edge energy which includes the effects of charge redistribution in the well region. The donor ionization energy E_d is the amount of energy required to excited a bound donor electron into the conduction band.

In a heterostructure the conduction band edge varies with position; meaning $P(E_{Donor}) = P(E_{Donor}(z)) = P(z)$. Thus from equation (3.27) we can write the probability distribution function that a donor electron has been excited

into the conduction band as,

$$1-P(z)=\frac{1}{1+g_d\exp\left(\frac{E_f-V_{total}(z)+E_d}{k_BT}\right)}. \tag{3.28}$$

This is also the probability that there is a hole in the donor band. Multiplying this by the donor density $n_{d_{16}}\cdot n^*_{donor}(z)$, will give the ionized donor (or hole) density [1],[23],[25],

$$n_h(z)=\frac{n_{d_{16}}n^*_{donor}(z)}{1+g_d\exp\left(\frac{E_f-V_{total}(z)+E_d}{k_BT}\right)} \tag{3.29}$$

where we scaled a typical carrier density, $n_{d_{16}}=10^{16}[cm^{-3}]$. We can write the donor charge distribution as,

$$\rho_h(z)=|e|\frac{n_{d_{16}}n^*_{donor}(z)}{1+g_d\exp\left(\frac{E_f-V_{total}(z)+E_d}{k_BT}\right)} \tag{3.30}$$

or as a source term,

$$S_h(\xi)=\frac{|e|^2\ell^2}{\varepsilon_o V_o}\frac{n_{d_{16}}n^*_{donor}(\xi)}{1+g_d\exp\left(\frac{E_f-V_{total}(\xi)+E_d}{k_BT}\right)} \tag{3.31}$$

Determination of the Fermi Level

We insist upon charge neutrality throughout the semiconductor. Thus the total number of conduction electrons must equal the total number of holes,

$$n_e = n_h \tag{3.38}$$

Charge neutrality is obtained by adjusting the Fermi Energy Level until the total number of holes equals the total number of conduction electrons. Thus by equating the number densities of equations (3.23) and (3.29) we can calculate the Fermi Energy, E_f for low temperatures. We calculate the Fermi Energy using the algorithm developed by Brent [44].

From equation (3.29) we can see that as temperature increases there begins to be a finite probability that there are ionized donor atoms throughout the entire barrier region and not just located near the well region. Typically not all of the electrons from these ionized donor atoms occupy a quantum well states because at high temperatures there will be many more conduction electrons than quantum well states. This implies that as temperature increases electrons not only occupy the quantum well region but also the entire conduction band region above of the AlGaAs barrier. This adds a level of difficulty in determining the Fermi level.

4) Self-consistent Solution

The net effect of charge redistribution in the heterostructure device is to change the band edge profile, which in turn modifies the electrical properties of the device. A self-consistent solution of the Schrödinger and Poisson Equations is used to determine the band edge profile. The energy band offset and the energy levels in a carrier confining heterostructure are calculated utilizing the Hartree approximation. The Hartree approximation is the superposition or 'build-up' of the actual 'field' by accounting for physical effects one-at-a-time [40]. The procedure is to start from a simplified model and then build more complexities into the model until the physical phenomena is adequately modelled; the most important interactions are treated first followed by the minor interactions. In this approximation electrons are assumed to be independent of each other and the total electric potential is assumed to be the sum of several individual potentials.

In the Hartree approximation we assume that the 'overall' or 'bulk' band edge profile of the heterostructure results from the energy band profile of each individual semiconductor layer alone; the layers do effect the profile of the band edges of the other semiconductor layers. This heterojunction conduction energy band edge is illustrated in Figure 4.1 (a) and will be refered to as the 'bulk potential energy' V_{bulk} or V_0. The energy bands of the heterojunction are aligned based on the band offset estimates provided in Section 3.1.

The effect of charge carriers from the ionized donor (or acceptor) atoms is included next. A quantum well offers a way for the charge carrier to minimize its total energy. Free charge carriers 'see' the quantum well and start to occupy the well's available states. This separation of the charge carriers from their parent atoms leads to a build up of charge in the quantum well and opposite charge in the region containing the donor or acceptor atoms (barrier region). This redistribution of charge inside the heterostructure will result in an electric potential which acts to change in the band structure. Figure 4.1 (b) illustrates the band

bending of the conduction band edge due to this process. Using the principle of superposition we construct the total potential energy as the sum of the 'bulk' heterostructure potential and the potential due to the redistribution of charge inside the heterostructure, $V_{total}(z) = V_{bulk}(z) + V_{chrg}(z)$.

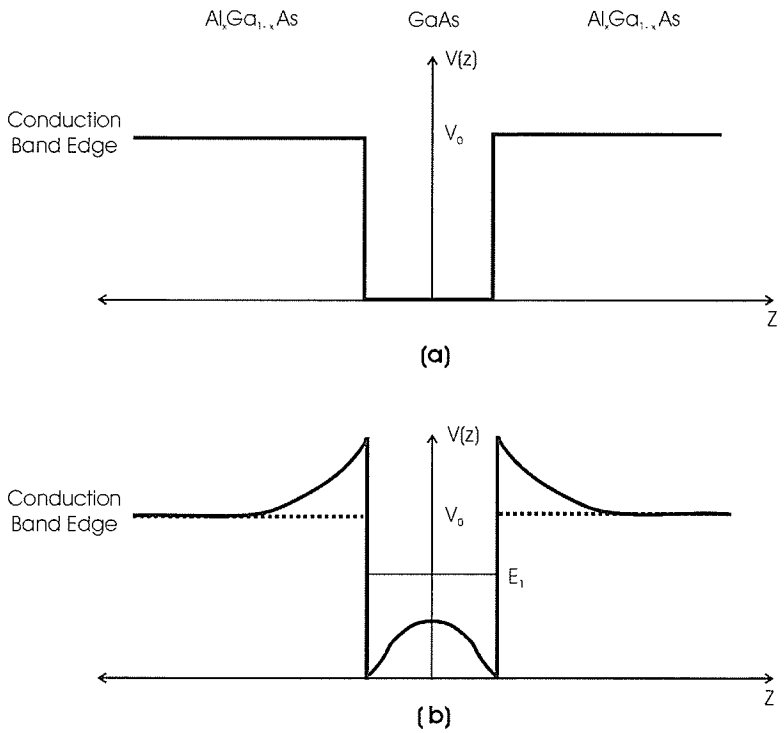

Figure 4.1: (a) The conduction band profile of a heterojunction considering only the 'bulk' semiconductor properties and **(b)** the conduction band edge bending after including the effect of the ionized donor atoms in the depletion region and electrons inside the well region.

Charge carriers will not continuously 'flow' into the quantum well. Charge carriers will stop entering the quantum well after, 1) all the accessible quantum well states are occupied and/or, 2) the Coulomb repulsive potential arising from the charge carriers already present in the well, prevents new charge carriers from entering the well. Condition 1 is satisfied by summing over all accessible states of the quantum well, including the in-plane (xy-plane) energy dispersion of the well. Condition 2 is satisfied by the simultaneous solution of the Schrödinger and

Poisson equations.

The self-consistent solution involves solving Poisson's equation for the electric potential due to the distribution of charge carriers and ionized donor/acceptor atoms. Using this electric potential in Schrödinger's equation, we then solve for the eigenvalues and associated wave functions from which we calculate the distribution of charges in the depletion region and quantum well. This cycle of calculating the electric potential from the charge distribution and then calculating the charge distribution from the electric potential is repeated until both calculations reproduce a charge distribution and electric potential which are consistent with each other. In this manner a self-consistent solution is generated.

The effects of other phenomena can be included by modifying the Schrödinger equation. For example, the effect of an externally applied electric field is easily included in self consistent solution by invoking the superposition principle for potentials [1], allowing us to add another term to the total potential energy, $V_{total}(z) = V_{bulk}(z) + V_{chrg}(z) + V_{external}(z)$. The effect of exchange and correlation due to electron-electron interactions can also be easily included in our calculation.

We will use the procedure developed by Trellakis[22] and later modified by Moussa, Yoo, and Moussa [14],[13] to develop an approximate expression for the charge carrier number density which relates the number density to the change in potential energy. We will use an inner loop to solve for the change in potential energy $\delta V_{chrg}^{(k)}(z)$. As before, the finite element solution is written as the sum of the interpolation shape functions, $\delta V_{chrg}(z) = \sum \delta v_i \, \varphi_i(z)$. At each iteration of the inner loop we update the potential due to the distribution of charges using,

$$V_{chrg}^{(k+1)}(z) = V_{chrg}^{(k)}(z) + \sigma \, \delta V_{chrg}^{(k)}(z), \qquad \textbf{(4.1)}$$

where σ is a scaling factor used to dampen oscillations in the iterations. It is in the range, $0 < \sigma \leq 1$, and is adjusted during the iteration process to accelerate convergence. As the iterations progress the change in the potential

$\delta V_{chrg}^{(k)}(z)$ becomes very small and we can set $\sigma = 1$. Our scaling factor is initiated at a very conservative value and through the use of a 'look-up' table adjusted based on the rate-of-convergence from between successive iterations. The self-consistent algorithm is initiated with a 'guess' or 'seed potential'. Our self-consistent procedure is illustrated in Figure 4.2.

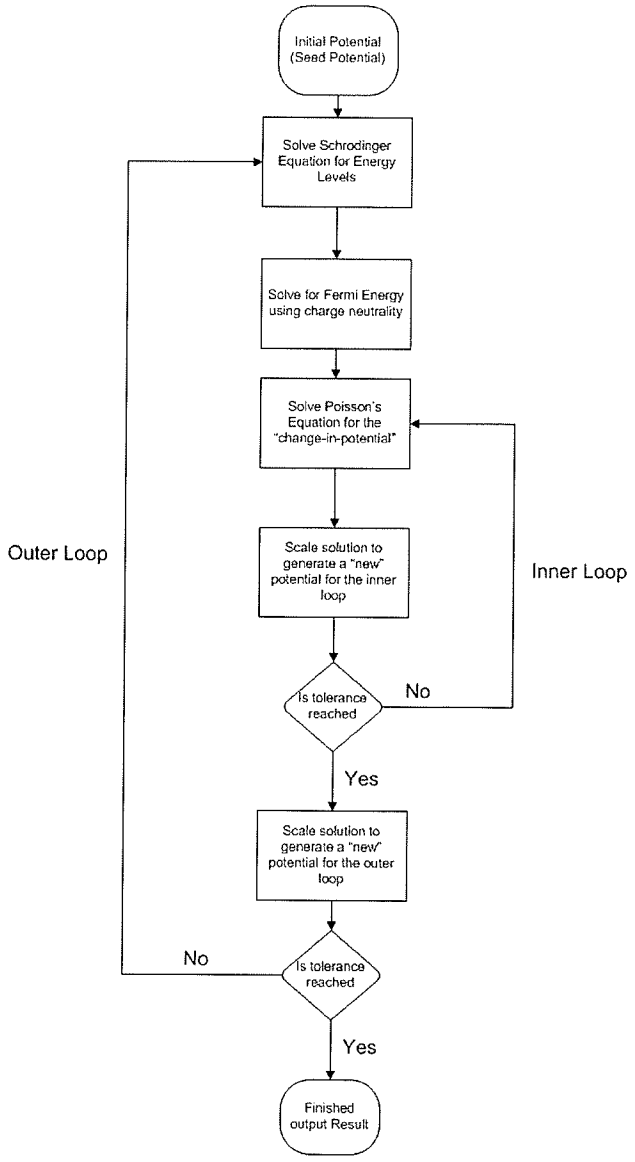

Figure 4.2: Flow chart of the self-consistent algorithm.

4.1 Decoupling the Schrödinger and Poisson Equations

We can develop a finite element equation to solve for the change in potential $\delta V_{chrg}^{(k)}(z)$ by substituting equation (4.1) into equation (3.17) (with $\sigma = 1$),

$$\begin{aligned} &\int_{\Omega} \varepsilon_r(z) \frac{d}{dz}\varphi_n(z) \frac{d}{dz}\left[V_{chrg}^{(k)}(z) + \delta V_{chrg}^{(k)}(z) \right] dz \\ &\quad - \varphi_n(z)\varepsilon_r(z) \frac{d}{dz}\left[V_{chrg}^{(k)}(z) + \delta V_{chrg}^{(k)}(z) \right]\Big|_a^b \\ &= -\int_{\Omega} \varphi_n(z)\left[S_d\left(V_{chrg}^{(k)}(z) + \delta V_{chrg}^{(k)}(z) \right) + S_e\left(V_{chrg}^{(k)}(z) + \delta V_{chrg}^{(k)}(z) \right) \right] dz. \end{aligned} \tag{4.2}$$

In equation (4.2), $V_{chrg}^{(k)}(z)$ is known from either the outer loop or the previous iteration k of the inner loop. Thus we are solving an equation of the form,

$$\left[\mathbf{A} + \mathbf{G} + \mathbf{H} \right] \delta \mathbf{v}_{chrg} = -\left[\mathbf{A} \cdot \mathbf{v}_{chrg} + \mathbf{g} + \mathbf{h} + \mathbf{f} \right] \tag{4.3}$$

where we solve for the unknown $\delta \mathbf{v}_{chrg}$ with,

$$\begin{aligned} \mathbf{A} &= \int_{\Omega} \varepsilon_r(z) \frac{d}{dz}\varphi_i(z) \frac{d}{dz}\varphi_j(z) dz - \varphi_i(z)\varepsilon_r(z) \frac{d}{dz}\varphi_j(z)\Big|_a^b \\ \mathbf{v}_{chrg} &= V_{chrg}^{(k)}(z_i) \\ \delta \mathbf{v}_{chrg} &= \delta V_{chrg}^{(k)}(z_i). \end{aligned} \tag{4.4}$$

The terms **G**, **H**, **g**, **h**, and **f** come from the functional for the source term as derived in the following.

In the following derivations we implicitly imply the dependence of the functional on the bulk potential $V_{bulk}(z)$ and to save space, do not include this term in the expressions. First, the functional for the source term due to donors is considered,

$$\mathrm{F}_i^{donor}\left(V_{chrg}^{(k)}(z)+\delta V_{chrg}^{(k)}(z)\right)$$
$$=\int_{\Omega}\varphi_i(z)S_d\left(V_{chrg}^{(k)}(z)+\delta V_{chrg}^{(k)}(z)\right)dz. \tag{4.5}$$

We can approximate the functional $\mathrm{F}_i^{donor}\left(V_{chrg}^{(k)}(z)+\delta V_{chrg}^{(k)}(z)\right)$ as a Taylor expansion up to first order,

$$\mathrm{F}_i^{donor}\left(V_{chrg}^{(k)}(z)+\delta V_{chrg}^{(k)}(z)\right)$$
$$\int_{\Omega}\varphi_i(z)\left[S_d\left(V_{chrg}^{(k)}(z)\right)+\frac{\partial S_d\left(V_{chrg}(z)\right)}{\partial V_{chrg}(z)}\delta V_{chrg}^{(k)}(z)\right]dz, \tag{4.6}$$

which we can rewrite as,

$$\mathrm{F}_i^{donor}\left(V_{chrg}^{(k)}(z)+\delta V_{chrg}^{(k)}(z)\right)=$$
$$\mathbf{g}+\mathbf{G}\,\delta\mathbf{v}_{chrg}^{(k)} \tag{4.7}$$

where,

$$\mathbf{g}=\mathrm{F}_i^{donor}\left(V_{chrg}^{(k)}(z)\right)=\int_{\Omega}\varphi_i(z)\,S_d\left(V_{chrg}^{(k)}(z)\right)dz. \tag{4.8}$$

The functional derivative term is approximated using a finite difference approximation as,

$$\mathbf{G}\,\delta\mathbf{v}_{chrg}^{(k)}$$
$$\int_{\Omega}\varphi_i(z)\sum_j\left[\frac{S_d\left(V_{chrg}^{(k)}(z)+\Delta V_{chrg}^{(k)}(z)\right)-S_d\left(V_{chrg}^{(k)}(z)-\Delta V_{chrg}^{(k)}(z)\right)}{2\,\Delta V_{chrg}^{(k)}(z)}\right] \tag{4.9}$$
$$\varphi_j(z)dz\quad\delta v_{chrg}^{(k)}(z_j).$$

Here the functional derivative is approximated with respect to changes in the potential energy function $\Delta\mathrm{V}_{chrg}^{(k)}(\mathrm{z})=\mathrm{V}_{chrg}^{(k)}(z)-\mathrm{V}_{chrg}^{(k-1)}(z)$. This functional

derivative is not evaluate for the first iteration of the inner loop. Moussa, Yoo, and Moussa [14],[13] calculate the functional derivative at nodal points only. Our derivation differs in that we calculate the functional derivative over the entire element.

An approximate expression for the charge carrier density is derived next. As the potential energy is updated from $V_{chrg}^{(0)}$ to $V_{chrg}^{(k)}$ during the iteration process, there is a corresponding change in the carrier charge density. This change in the carrier charge density is the result of the change in the band structure of the heterostructure. A change in the band structure will result in a change in the energy eigenvalues of the electrons bound in the quantum well region. In the inner iteration loop we do not want to resolve the Schrödinger equation for the energy eigenvalues, instead we will account for the change in the energy eigenvalues by adding the change in potential energy to the eigenvalues. Using the fact that the wave function changes very slowly from iteration to iteration, we can simplify the method by recognizing that we can rewrite equation (3.24) in terms of a "density of states" and a Fermi distribution for each 'bin',

$$n_e(z) = \sum_i \frac{\Lambda_i(z)}{1+\exp\left(\frac{E_i - E_f}{k_B T}\right)}. \tag{4.10}$$

Here 'i' labels the bin and in dimensionless form $k_\perp = E = E_i$. The density of states term, $\Lambda_i(z)$, contains the wave function information and is not updated in the inner loop. The change in the carrier charge density is taken into account in the Fermi distribution function by adding the change in potential energy to the bin energies,

$$\varsigma_i^{(k)}(z) = E_i + V_{chrg}^{(k)}(z) - V_{chrg}^{(0)}(z). \tag{4.11}$$

It is more convenient to work with the charge density, thus we multiply equation

(4.10) by the appropriate constants to convert it into a charge density.

The change in the carrier charge density from the first iteration to the k^{th} is represented by,

$$\Delta\rho_e\left(\varsigma_i^{(k)}(z)\right)=\rho_e^{(k)}(\varsigma_i^{(k)}(z))-\rho_e^{(0)}(z) \tag{4.12}$$

where $\rho_e^{(0)}(z)$ represents the initial charge carrier density at the beginning of the inner iteration. Thus from equation (4.10) and (4.12) we can write,

$$\Delta\rho_e\left(\varsigma_{v,k_\perp}^{(k)}(z)\right)=$$

$$-|e|\sum_i \Lambda_i(z)\left\{\frac{1}{1+\exp\left(\frac{\varsigma_i^{(k)}(z)-E_f}{k_BT}\right)}-\frac{1}{1+\exp\left(\frac{E_i-E_f}{k_BT}\right)}\right\}. \tag{4.13}$$

Multiplying by the appropriate constant enables us to write an equivalent expression for the source term in equation (4.2),

$$S_e^{(k)}(V_{chrg}^{(k)}(z)+\delta V_{chrg}^{(k)}(z))=\Delta S_e\left(V_{chrg}^{(k)}(z)+\delta V_{chrg}^{(k)}(z)\right)+S_e^{(0)}(V_{chrg}^{(0)}(z)). \tag{4.14}$$

Thus we can write the source term due to charge carriers in equation (4.2) as,

$$\begin{aligned}&\mathrm{F}_i^{carrier}\left(V_{chrg}^{(k)}(z)+\delta V_{chrg}^{(k)}(z)\right)\\&=\int_\Omega \varphi_i(z)S_e\left(V_{chrg}^{(0)}(z)\right)dz+\int_\Omega \varphi_i(z)\Delta S_e\left(V_{chrg}^{(k)}(z)+\delta V_{chrg}^{(k)}(z)\right)dz\end{aligned} \tag{4.15}$$

where the first term on the right-hand-side is explicitly calculated in the outer loop for the Schrödinger equation evaluation. All terms in this expression are known and we write this as the term $\mathbf{f}$ in equation (4.3) as,

$$\mathbf{f}=\int_\Omega \varphi_i(z)\,S_e\left(V_{chrg}^{(0)}(z)\right)dz=\int_\Omega \varphi_i(z)\,S_e(z)dz. \tag{4.16}$$

Expanding the second term on the right-hand-side in a Taylor expansion up to first order we have,

$$\int_{\Omega} \varphi_i(z)\Delta S_e\left(V_{chrg}^{(k)}(z)+\delta V_{chrg}^{(k)}(z)\right)dz = \int_{\Omega} \varphi_i(z)\left[\Delta S_e\left(V_{chrg}^{(k)}(z)\right)+\frac{\partial \Delta S_e\left(V_{chrg}(z)\right)}{\partial V_{chrg}(z)}\delta V_{chrg}^{(k)}(z)\right]dz. \tag{4.17}$$

The first term is easily evaluated using equation (4.13) and is the $\mathbf{h}$ term in equation (4.3),

$$\mathbf{h} = \int_{\Omega} \varphi_i(z)\,\Delta S_e\left(V_{chrg}^{(k)}(z)\right)dz. \tag{4.18}$$

The second term involves the functional derivative and is approximated using a finite difference approximation. For the $\mathbf{H}$ term in equation (4.3) we write,

$$\mathbf{H}\delta\mathbf{v}_{chrg}^{(k)} \quad \int_{\Omega}\left[\varphi_i(z)\frac{\partial \Delta S_e\left(V_{chrg}(z)\right)}{\partial V_{chrg}(z)}\varphi_j(z)\right]dz\;\delta v_{chrg}^{(k)}(z_j) = \int_{\Omega}\left[\varphi_i(z)\frac{\partial \Delta S_e\left(\varsigma_i(z)\right)}{\partial \varsigma_i(z)}\frac{\partial \varsigma_i(z)}{\partial V_{chrg}^{(k)}(z)}\varphi_j(z)\right]dz\;\delta v_{chrg}^{(k)}(z_j) \tag{4.19}$$

where,

$$\frac{\partial \Delta S_e\left(\varsigma_i(z)\right)}{\partial \varsigma_i(z)} = \frac{\Delta S_e\left(\varsigma_{i+1}+V_{chrg}^{(k)}(z)-V_{chrg}^{(0)}(z)\right)-\Delta S_e\left(\varsigma_i+V_{chrg}^{(k)}(z)-V_{chrg}^{(0)}(z)\right)}{\left(\varsigma_{i+1}(z)-\varsigma_i(z)\right)} \tag{4.20}$$

and,

$$\frac{\partial \varsigma_i}{\partial V_{chrg}^{(k)}(z)} = \frac{\partial}{\partial V_{chrg}^{(k)}(z)}\left(\varsigma_i + V_{chrg}^{(k)}(z) - V_{chrg}^{(0)}(z)\right) = 1. \qquad \textbf{(4.21)}$$

4.2 Convergence Conditions

With the appropriate choice of initial conditions, our method lends itself to a vary stable self-consistent algorithm with near monotonic convergence. For the finite element solution, the solution domain is subdivided into between 100 to 300 elements depending on the complexity of the problem geometry. With a suitable choice of seed potential the solution will converge within 500 iterations.

Initial attempts at a direct solution for the potential function resulted in poor solution convergence. The direct solution method did not involve an inner loop, and an 'intermediate' potential function was calculated using the updated energy eigenvalues, wave functions and Fermi energy. Using a weighting factor the 'intermediate' potential function was used to update the 'old' potential function into a 'new' potential.

For our convergence condition we use the vector-2-norm of the nodal values of the potential due to the distribution of charge,

$$\frac{1}{N}\sqrt{\sum_{i}^{N}\left(V_{chrg}^{(k+1)}(z_i)-V_{chrg}^{(k)}(z_i)\right)^2}<\tau \qquad \textbf{(4.22)}$$

where N is the number of nodal points and τ is the desired tolerance. Unless otherwise noted the solution tolerance was set at $\tau = 1\ \mu\text{eV}$ in our examples.

Refer to Appendix D for sample analytical problems used to test and confirm the performance of the finite element equations presented in this Chapter.

5) Modelled Heterostructures

The heterostructures studied in this thesis include *n*-type and *p*-type modulation-doped single quantum wells, a *n*-type modulation-doped double quantum well, a *n*-type modulation-doped asymmetric double quantum well and, a *n*-type modulation-doped single quantum well confined between metal contacts. The band bending dependence on temperature and donor concentration is also examined. Our results are found to be in good agreement with those in the literature.

5.1 Modelling Parameters

For the example calculations which follow we will assume that the size of the energy band gap of $Al_xGa_{1-x}As$ is given by,

$$E_g = 1.42 + 1.25x \tag{5.1}$$

for $0 \leq x \leq 0.45$ where 'x' is the amount of Ga replaced by Al in percent [27], [28]. The temperature dependence of the energy gap of bulk GaAs is described by the empirical relation [29],

$$E_g(T) = E_g(0) - \frac{0.0005408\,T^2}{T + 204} \tag{5.2}$$

where T is the temperature in Kelvin. The band edge alignments for heterostructure devices is experimentally estimated by Frensley [27] as,

$$\begin{aligned} \Delta E_C &= 0.77x \\ \Delta E_V &= 0.48x \end{aligned} \tag{5.3}$$

where 'x' is the amount of Ga replaced by Al in percent.

The effective mass of charge carriers within a heterostructure will vary depending upon the material making up the layer. For the layered $Al_xGa_{1-x}As$/GaAs compound material we will use an electron effective mass (Γ valley) to be [28],

$$m_e^{\Gamma} = 0.067 + 0.083x \tag{5.4}$$

and for the valence band the effective mass for heavy holes (hh) given by,

$$m_{hh} = 0.62 + 0.14x. \tag{5.5}$$

From Adachi [28] the static dielectric constant for $Al_xGa_{1-x}As$ is given by,

$$\varepsilon_0 = 13.18 - 3.12x. \tag{5.6}$$

The donor ionization energy (meV) as [28],

$$E_d = 5.2 + 7.9x + 7.1x^2. \tag{5.7}$$

The acceptor ionization energy (meV) will be taken as[26],

$$E_a = 10. \tag{5.8}$$

In all equations above, (5.4) to (5.7), x is the concentration of Al in percent. No donor doping is assumed for the well regions.

The seed potential and its first derivative used in simulations are given by the analytical expressions,

$$V_{seed}(z) = \frac{V_{centre}}{\cosh^2(\alpha z)} \tag{5.9}$$

and,

$$\frac{dV_{seed}(z)}{dz} = 2\,V_{centre}\,\frac{\alpha \sinh(\alpha z)}{\cosh^3(\alpha z)}, \tag{5.10}$$

respectively, where α is a scale factor that can be adjusted to vary the width of the seed potential function and V_{centre} is the height of the potential function.

We will ignore the presence of edge states which are outside of the scope of this thesis. These are the states which form at the edge of a semiconductor crystal as a result of the breaking of the periodic boundary conditions. They result from impurities which collect on crystal surfaces and, if the crystal is not properly grown, can contribute significantly to the bending of the conduction band, there by affecting the operation of the device. We will assume that we have an ideally grown crystal sufficiently large enough so that boundary effects are negligible.

We will ignore the effects of exchange and correlation due to electron - electron interactions. For GaAs heterostructures this has been found to be a reasonable omission for doping levels up to 10^{18} cm^{-3} [13]. We also assume that all electrons come from the donor atoms. For temperatures up to about 300 K this is a reasonable assumption as negligible valence electrons are thermally excited through the band gap. Finally, we will assume that we can treat all electrons as

being bound inside the solution region. Historically electrons in the barrier regions have been treated using the classical expression for the charge density. Ram-Mohan *et. al.* [13],[14] extended their approach to consider electrons as being free particles in the boundary regions. Our approach assumes a device of finite extent and therefore electrons are bound inside the solution region, bound either by 'large' potential barriers or infinite potential barriers. We can justify this assumption by recognizing that in any physical device the semiconductor is finite in extent and bound by air, vacuum, metallic connectors, etc.

Finally we will subdivide the solution domain into sub-elements only once, using the same element pattern to solve both the Schrödinger and Poisson equations. This greatly simplifies the bookkeeping and mapping of nodal points and elements for both equations. The number and size of the elements will be determined by the electron wave functions due to the wave function being highly oscillatory for those electrons energetic enough to be outside of the quantum well region and inside the 'barrier' conduction band region. The change in potential, being a smooth function, will not require as many elements. In all devices simulated, the origin of the spacial coordinate is assumed to be measured from the centre of the quantum well.

5.2 Heterostructure Devices

The purpose of the following examples is to verify the code and to determine the convergence. The example considered in Sections 5.2.1 - 5.2.4 is a 100 Å wide $Al_{0.35}Ga_{0.65}As$/ GaAs/$Al_{0.35}Ga_{0.65}As$ single quantum well device. This device is chosen because it allows our results to be compared with those found in the liturature[1].

5.2.1 n-type Single Quantum Well

The self-consistent potential of a *n*-type modulation-doped $Al_{0.35}Ga_{0.65}As$/ GaAs/$Al_{0.35}Ga_{0.65}As$, 100 Å wide single quantum well is calculated with a *n*-doping concentration of 10^{18} cm^{-3}. At a temperature of 5 K, this corresponds to a bulk potential V_0 (conduction band) with a 269.5 meV deep well. The solution domain is subdivided into 136 elements such that the elements in the barrier regions were 20 Å wide and smaller 5 Å wide elements were distributed near the well region in order to adequately model the depletion region. Compared with the literature [1],[13] where between 36 - 60 elements are used, this is significantly more elements which were necessary to model the wave functions in the barrier regions at large temperatures. In the literature the barrier regions were modelled using either the classical electron distribution or by a free electron model. The final number and size of elements used was based on the rate of convergence, that is as the number of elements is increased and the size decreased, the solution begins to converge to the 'same' value and the rate of convergence increases. Eventually changing the number and size of elements has little effect on the final solution and the convergence rate.

The finite element algorithm was initiated with the seed potential shown in Figure 5.1. For comparison the final potential energy is also drawn. For this problem the rate of convergence of the outer loop is shown in Figure 5.2. For this example it took 110 iterations of the outer loop for a self-consistent solution. Compared with the literature where convergence is achieved after 21 iterations,

our rate of convergence is slower, however, this is easily explained due to the increased number elements required to model the wave functions in the barrier regions. Figure 5.3 shows a typical rate of convergence for the inner iteration loop. It should be noted that the rate of convergence for the inner iteration loop varied greatly depending on iteration of the outer loop. For example, for the first iteration of the outer loop, the inner loop took 200 iterations to achieve convergence but in the final 110^{th} iteration, only 2 iterations of the inner loop were necessary to achieve convergence. In general the number of outer iterations required for convergence increases as the donor concentration increases or as the device complexity increases. The rate of convergence also depends on the initial conditions.

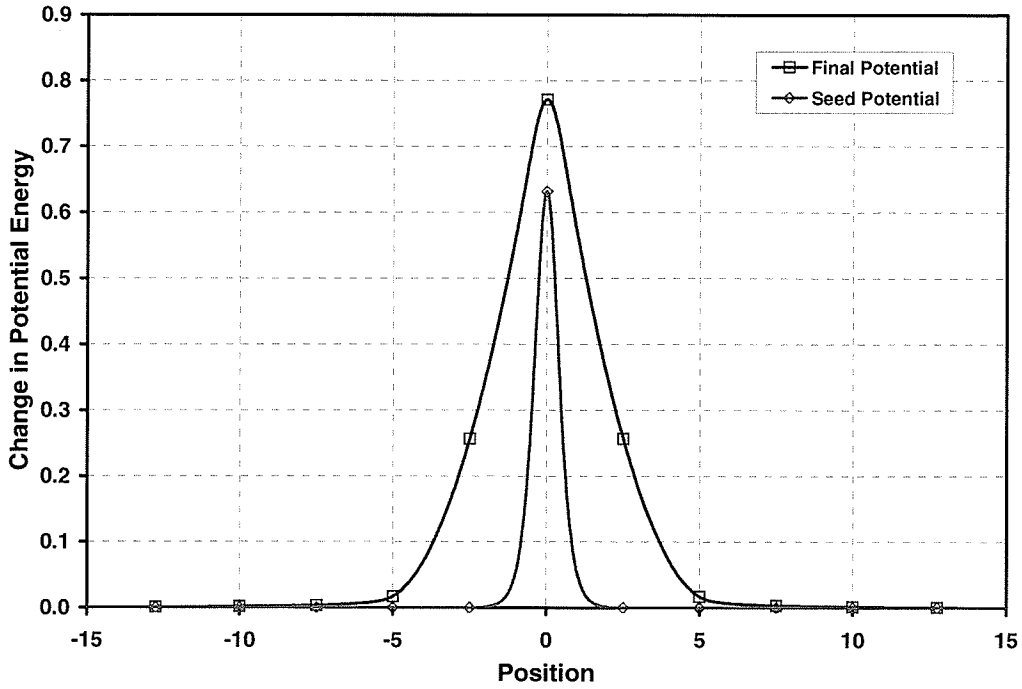

Figure 5.1: The difference between the initial seed potential and the final potential function of a 100 Å, AlGaAs/GaAs/AlGaAs electron confining quantum well heterostructure at T = 5 K and donor concentration of 10^{18} cm^{-3}.

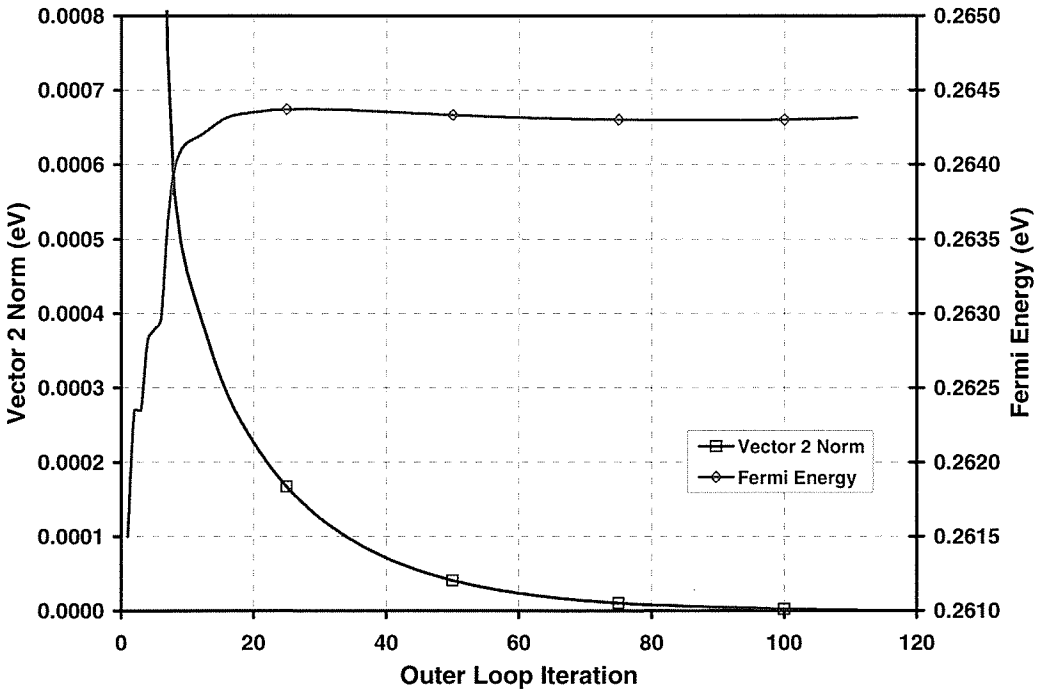

Figure 5.2: The rate of convergence for the potential function of the outer loop (Schrödinger) of an *n*-doped quantum well at T = 5 K. The convergence of the Fermi energy is overlayed.

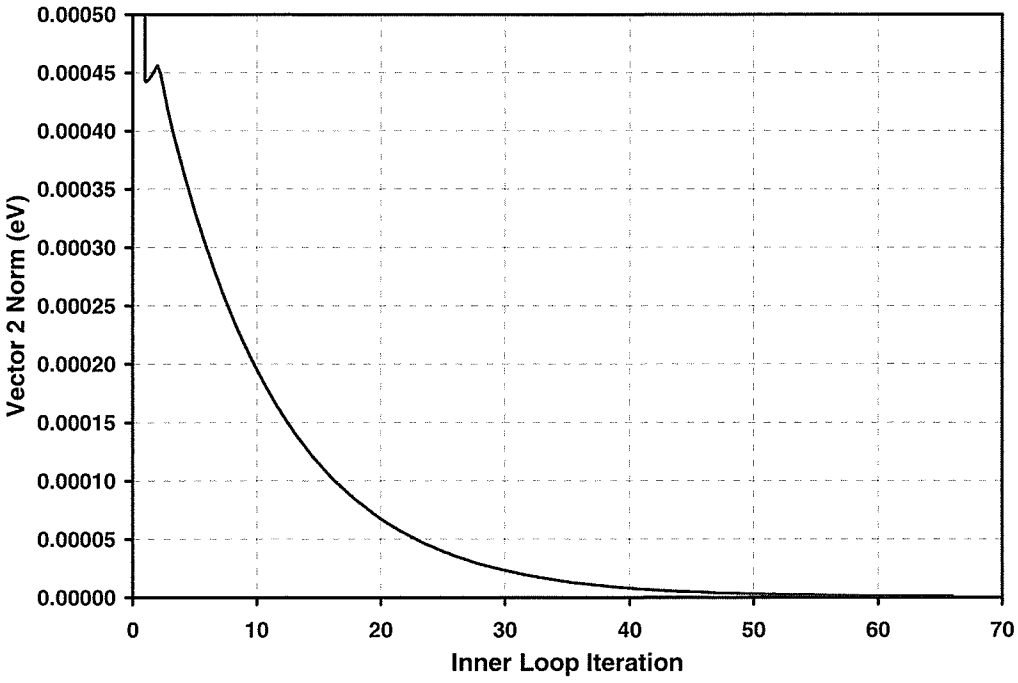

Figure 5.3: A typical rate of convergence for the potential function of the inner loop for an *n*-doped quantum well at T = 5 K. Convergence of the inner loop requires less iterations as the number of outer loop iterations increases.

The calculated self-consistent potential after considering the effect of electrons occupying the accessible states in the quantum well is shown in Figure 5.4. After the self-consistent calculation, this well is found to contain two distinct energy eigenvalues for the electrons confined in the well and a depletion region of about 26 Å on both sides of the well. Figure 5.5 shows the two electron wave functions corresponding to the two energy eigenstates. Note that inside the barrier regions the wave functions decay rapidly to zero implying that the free electrons are confined to the well region only. Figure 5.6 shows the density of electrons and holes in the one-dimensional heterostructure device. Finally for illustrative purposes, Figure 5.7 shows both the 'classical' conduction and valence band edge profiles of this heterostructure. The distribution of charge inside of the well region due to the electrons confined in the well region has the effect of bending both the conduction and valence band edges.

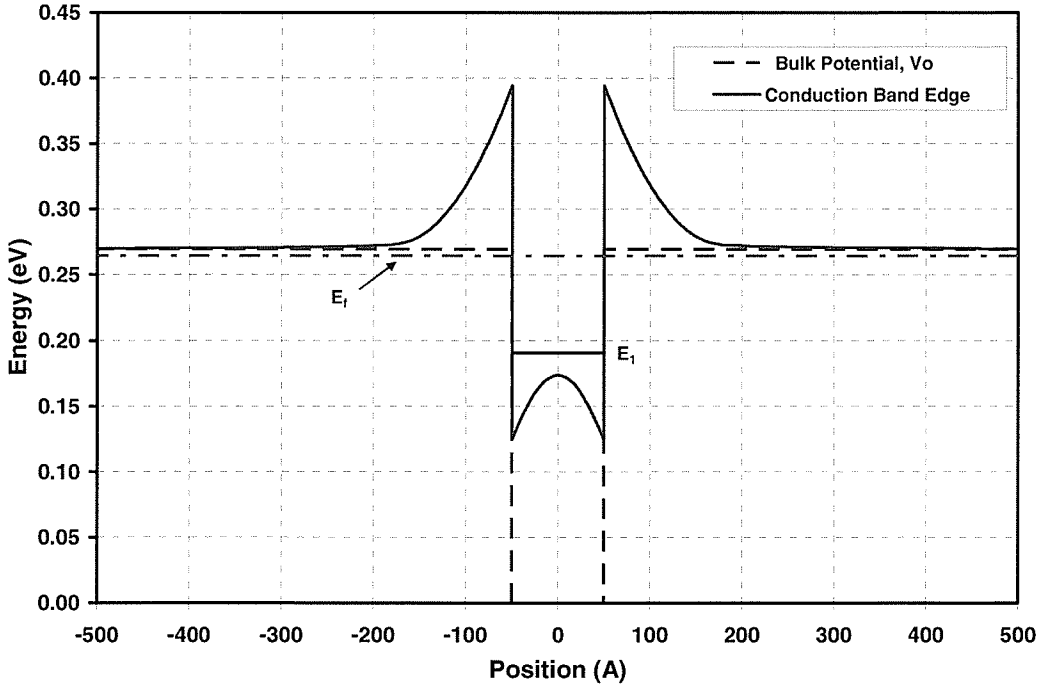

Figure 5.4: The conduction band edge bending of a 100 Å, AlGaAs/GaAs/AlGaAs electron confining quantum well heterostructure at T = 5 K and donor concentration of 10^{18} cm^{-3}. The conduction band edge is the solid (red) line. The Fermi energy is the dot-dashed (green) line. The bulk semiconductor conduction band is the dashed (blue) line. The energy eigenvalues bound in the well are also indicated.

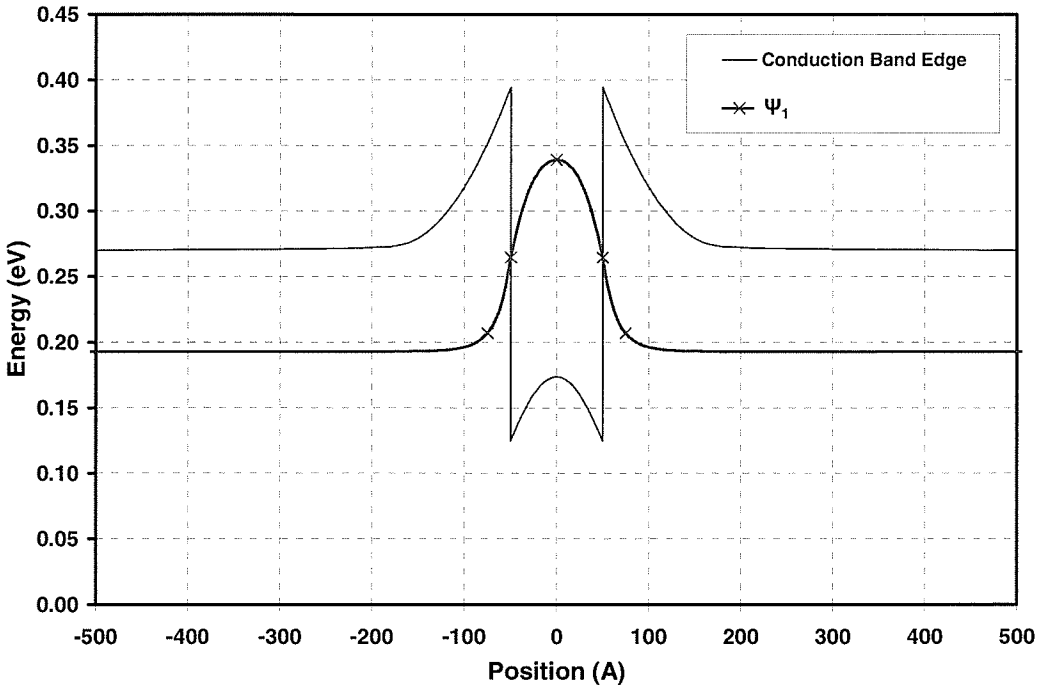

Figure 5.5: Wave function of the bound state for the quantum well Heterostructure of Figure 5.4. Note that the wave function quickly decays to zero outside the well region.

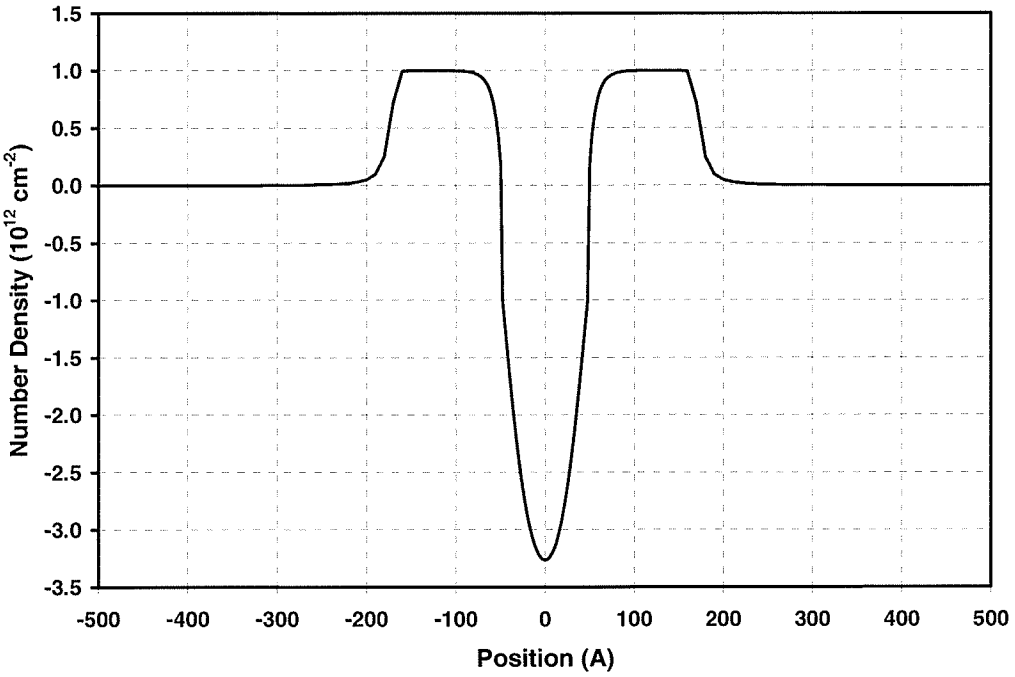

Figure 5.6: The number density of holes and electrons for the electron confining well heterostructure of Figure 5.4. A positive number density represents holes and a negative number density represents electrons.

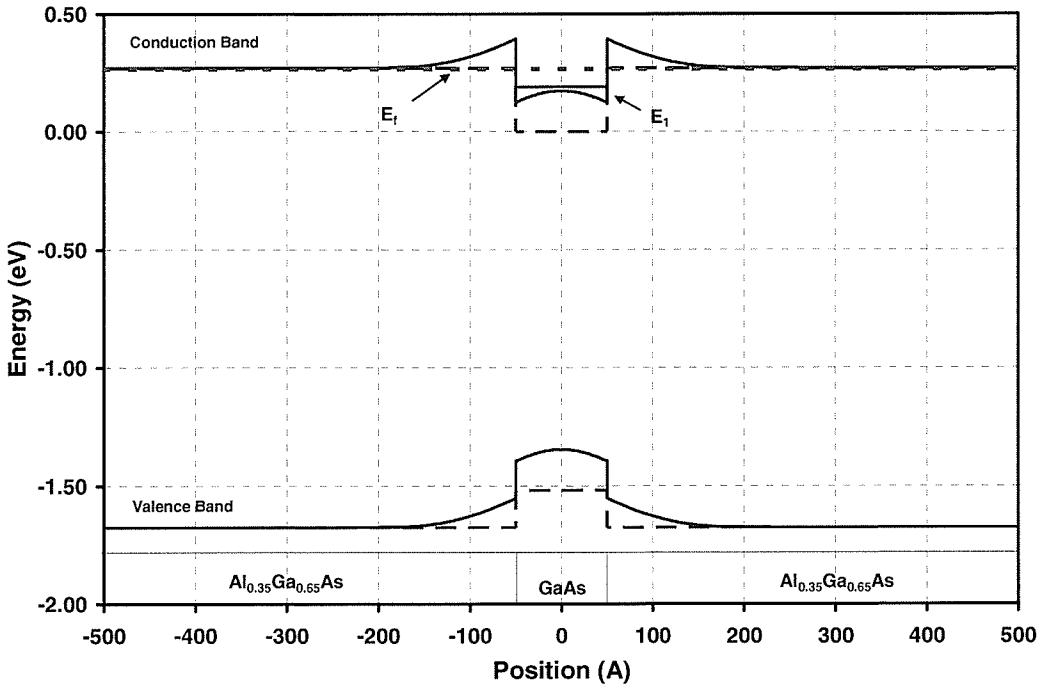

Figure 5.7: The conduction and valence band edge profile for the electron confining quantum well heterostructure of Figure 5.4. The solid (red) line represents the band edges. The large dashed (blue) line is the bulk band profile. The Fermi energy (small dashed green) and energy eigenvalues are shown. The bottom of the conduction band well is taken as the reference point.

5.2.2 Dependence of the Band Edge Profile on Donor Concentration

The self-consistent potential for the quantum well of Section 5.2.1 is calculated with *n*-doping concentrations of 10^{16} cm^{-3}, 10^{17} cm^{-3}, 10^{18} cm^{-3} and, 10^{19} cm^{-3} at a temperature of 5 K (a concentration of 10^{19} cm^{-3} or above may violate our assumption that the electron-electron interactions can be ignored). Figure 5.8 shows the conduction band edge profile for the different donor concentrations. From this figure it is clear that as the donor concentration increases the width of the depletion region decreases. Likewise the band edge exhibits sharper bending as the donor concentration increases. Figure 5.9 and 5.10 show the 'change-in-potential' resulting from the distribution of charges inside the heterostructure and the hole/electron number density across the device respectively. A smaller donor concentration has a wider depletion region which results in a larger 'change-in-potential'. From Figure 5.10 it is apparent that as the donor concentration increases so to do the number densities of holes and electrons.

The trends observed in Figures 5.8 - 5.10 can be explained by, at larger donor concentrations the corresponding depletion region is smaller. Subsequently the conclusion that the electric potential resulting from the charge displacement is much better 'screened out' due to the fact that the positive and negative charge is concentrated into a smaller region. Hence the band edge bending is reduced. Also, at larger donor concentrations, more electrons can enter into the well region as a conduction electron is more likely to tunnel through the smaller 'spiked' barrier at the well edge.

Table 5.1 lists the approximate width of the depletion region on either side of the quantum well, the Fermi energy, and the energy eigenvalues bound in the well region. Note that at large donor densities the well region can contain more than one energy eigenstate. These results agree with those found in the literature [1],[13].

Table 5.1: Depletion region, Fermi Energy and the Energy Eigenstates bound in the well region for a 100 Å, AlGaAs/GaAs/AlGaAs carrier confining quantum well with a Al impurity concentration of 0.35 and at T = 5 K for different donor concentrations.

Donor Concentration [cm^{-3}]	Depletion Region [Å]	Fermi Energy [meV]	Energy Eigenstates Bound in Well Region [meV]
10^{16}	1900	262.77	256.11
10^{17}	630	263.31	233.30
10^{18}	140	264.32	190.80
10^{19}	30	264.55	151.55 215.24

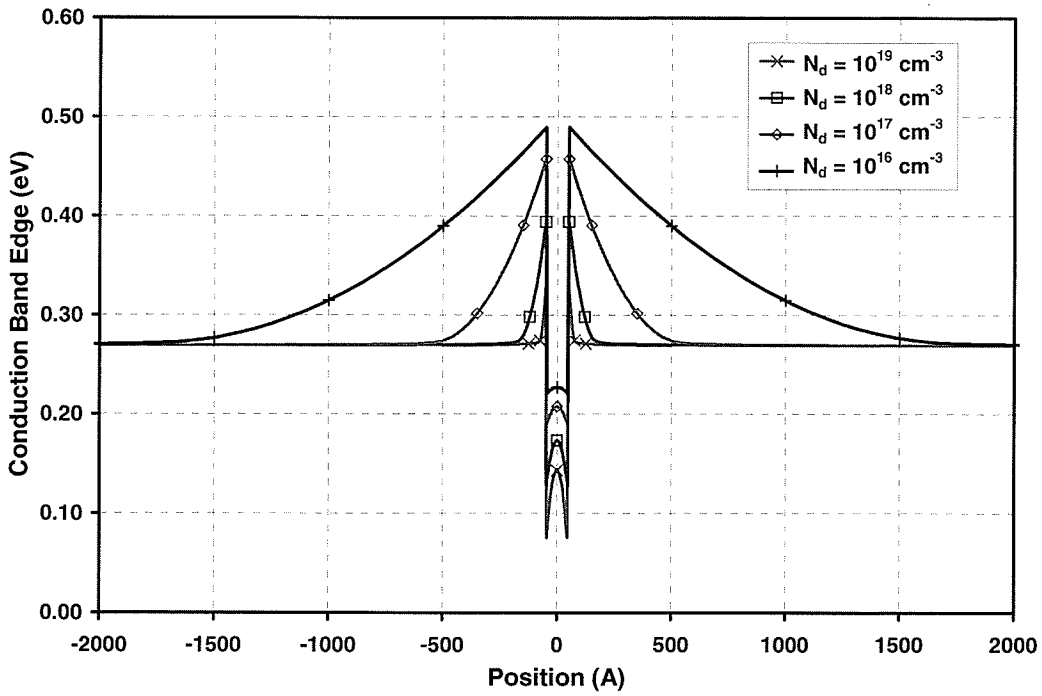

Figure 5.8: The effect of the *n*-type donor concentraton on the conduction band edge bending for a 100 Å, AlGaAs/GaAs/AlGaAs electron confining quantum well heterostructure at T = 5 K.

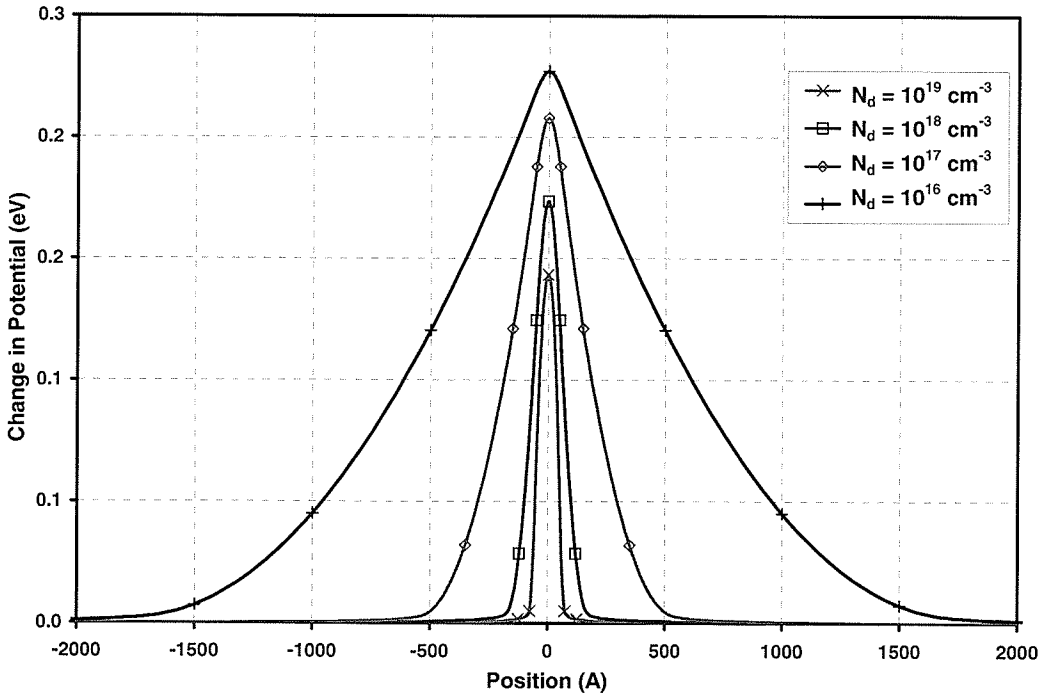

Figure 5.9: The effect of donor concentration on the 'change in potential' resulting from the distribution of charges inside a 100 Å, AlGaAs/GaAs/AlGaAs electron confining quantum well heterostructure at T = 5 K.

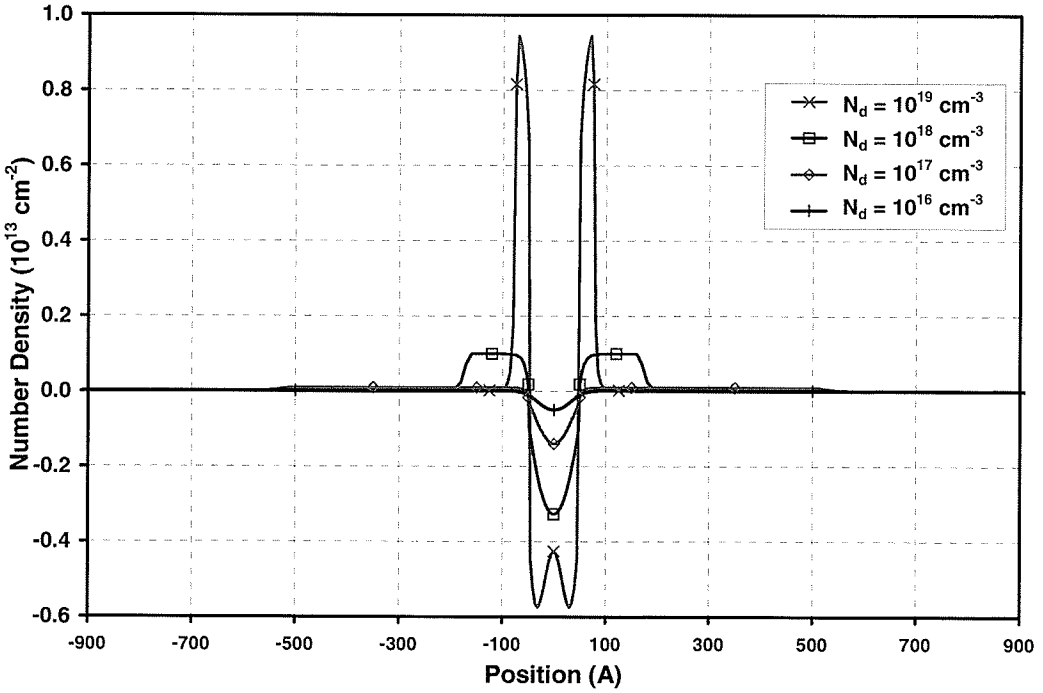

Figure 5.10: The effect of donor concentration on the hole and electron number density for the heterostructure of Figure 5.8. A positive number density represents holes and a negative number density represents electrons. Note that for a donor concentration of 10^{16} cm^{-3} the depletion region extends beyond the range of this plot.

5.2.3 Effect of Temperature on the Band Edge Profile

The self-consistent potential of the quantum well of Section 5.2.1 is calculated at temperatures 5 K, 100 K and, 300 K with a *n*-doping concentration of 10^{18} cm^{-3}. The bulk potential V_0 (conduction band) has a 269.5 meV deep well. To ensure that the depletion region was not effected by edge effects, the entire quantum well heterostructure device is assumed to be contained inside a 3000 Å wide infinite well. Donor doping is assumed to extend throughout the entire region (except for the well region). This is a reasonable assumption for a device of finite extent in air or vacuum.

Figure 5.11 shows the conduction band edge profile at different semiconductor temperatures. This figure illustrates that as temperature increases the conduction band edge bending increases in extent implying that as temperature increases the number of electrons occupying well states decreases. This occurs because as temperature increases electrons are thermally more energetic and thus are more likely to occupy the 'barrier' energy states in the AlGaAs conduction band. The net effect of these higher energy conduction electrons is to shift the conduction band edge up. As before, conduction electrons in the AlGaAs barrier material which are near to the well region are more likely to fall into the quantum well. Figure 5.12 illustrates that the transition between the depletion region and the neutral barrier regions becomes smoother as temperature increases. Note that even though donor atoms have been ionized and their electrons occupy the AlGaAs conduction band states, the AlGaAs regions are neutral. This is the case because even though electrons are excited into the conduction band they have not moved far from their parent donor atoms. Figure 5.12 also indicates that there is a charge build up at the device edges.

Table 5.2 lists the Fermi energy, the energy eigenvalues bound in the well region and the approximate width of the depletion region on either side of the quantum well. Figure 5.13 illustrates the hole and electron densities separately

when the heterostructure device is at T = 300 K. Ignoring edge effects, it can be seen that in the AlGaAs region, the number of electrons and holes are equal. These results agree with those found in the literature [1],[13].

Table 5.2: Fermi Energy, well energy state and approximate depletion region for a 100 Å, AlGaAs/GaAs/AlGaAs carrier confining quantum well with a Al impurity concentration of 0.35 and a donor concentration of 10^{18} cm^{-3} at different temperatures.

Temperature [K]	Fermi Energy [meV]	Well Energy State [meV]	Depletion Region [Å]
5	264.32	190.80	120
100	275.08	203.51	115
300	265.25	207.03	155

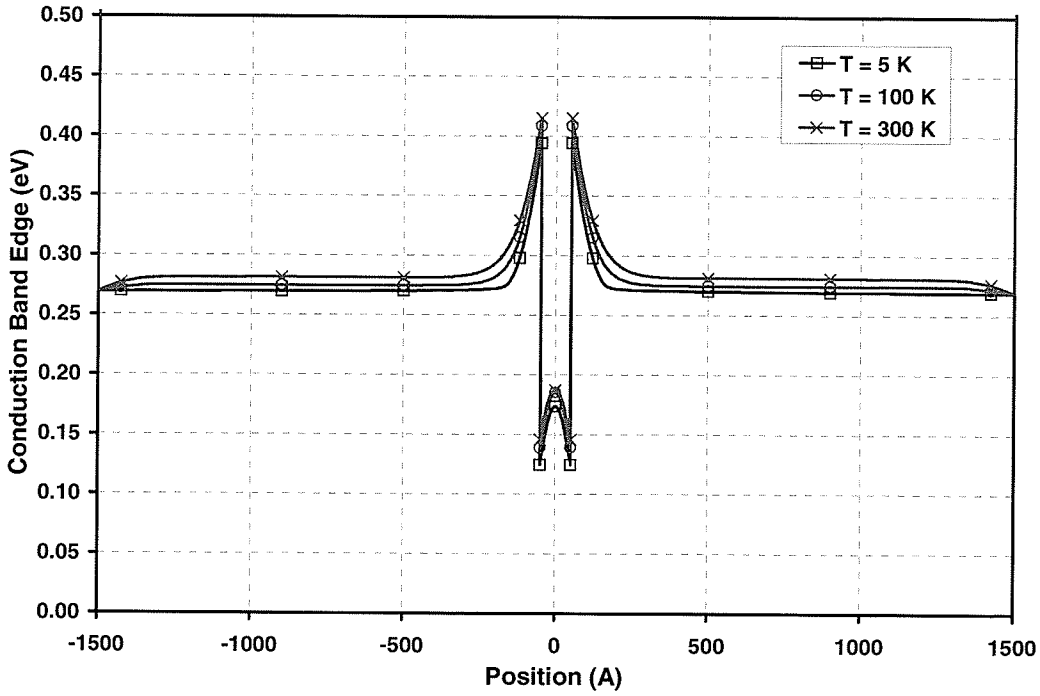

Figure 5.11: The effect of temperature on the bending of the conduction band edge for a 100 Å wide GaAs quantum well with $Al_{0.35}Ga_{0.65}As$ barriers that are *n*-doped to 10^{18} cm^{-3}.

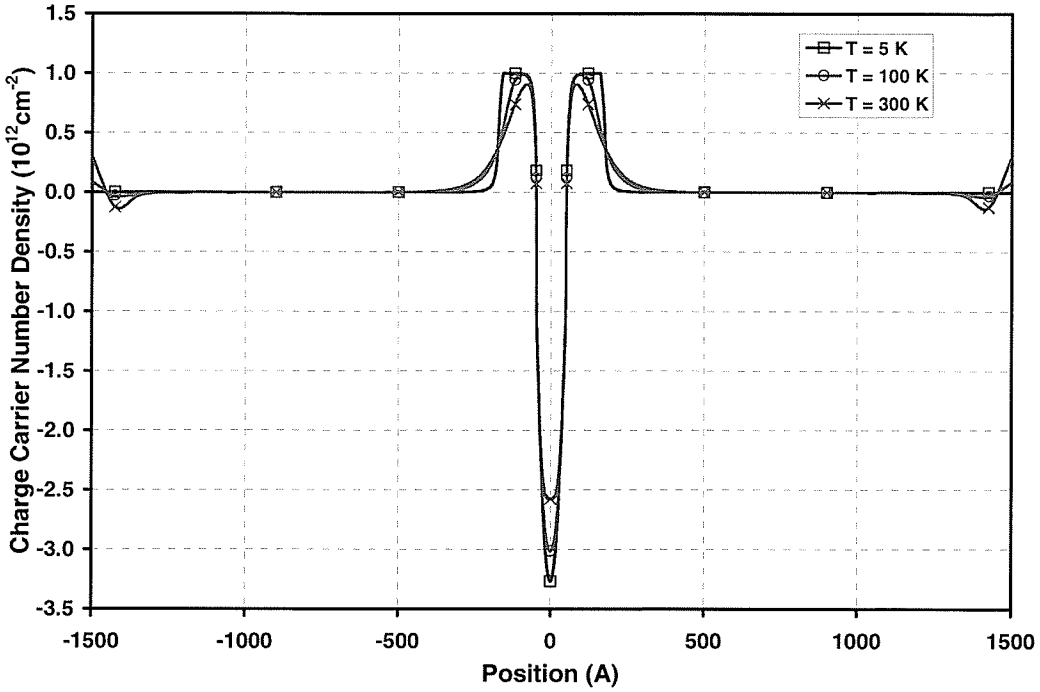

Figure 5.12: The effect of temperature on the number density of electrons and holes for the quantum well heterostructure of Figure 5.11. A positive number density represents holes and a negative number density represents electrons.

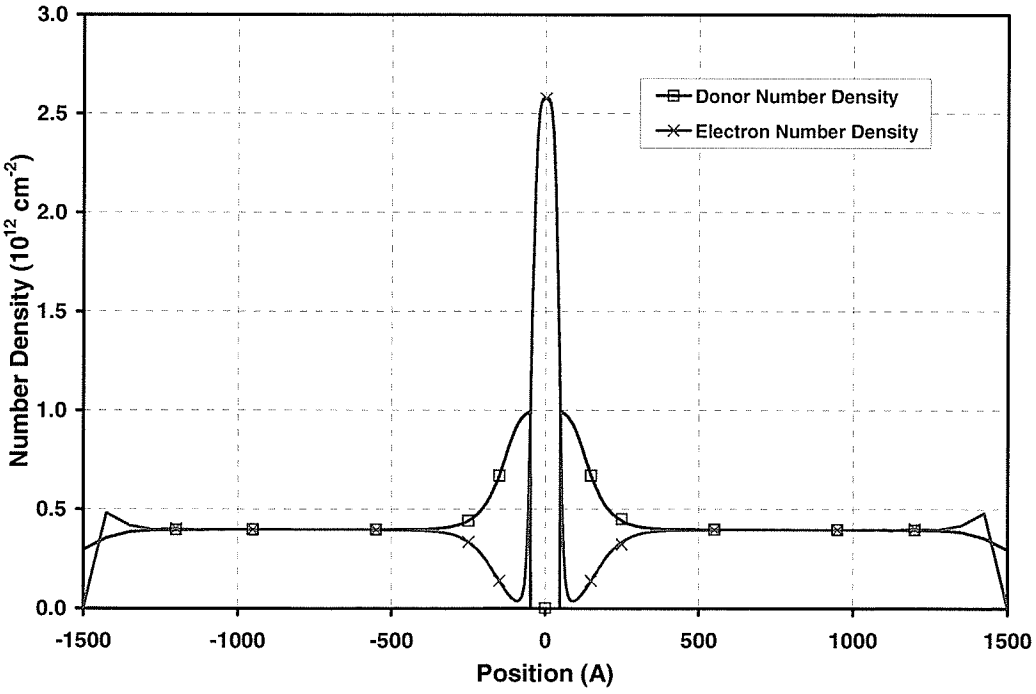

Figure 5.13: The effect of limited donors on the number density of electrons and holes for the quantum well heterostructure of Figure 5.11 at T = 300 K.

5.2.4 Effect of the Size of the Donor Region on the Band Edge Profile

The self-consistent potential of the quantum well of Section 5.1.3 is calculated with a *n*-doping concentration of 10^{18} cm^{-3}. The doping region is restricted to 950 Å on either side of the quantum well to model the effect of limited donor electrons. The self-consistent potential is calculated at temperatures 5 K, 100 K and, 300 K. The entire quantum well heterostructure device is assumed to be contained inside a 3000 Å wide infinite well.

Figure 5.14 and 5.15 show the conduction band edge profile at different semiconductor temperatures and the charge carrier number density, respectively. As before, as temperature increases the number of electrons occupying well states decreases. Figure 5.14 indicates that as temperature increases the conduction band edge begins to form 'satellite quantum wells' on either side of the GaAs quantum well in the AlGaAs donor (barrier) region. This is a unique feature not mentioned in the liturature. Figure 5.15 illustrates that the transition between the depletion region and the neutral barrier regions becomes smoother as temperature increases. It also indicates that there is a charge build up at the edge of the donor regions.

Figure 5.16 illustrates the hole and electron number densities separately when the heterostructure device is at T = 300 K. It can be seen that in the doped AlGaAs barrier regions (region of the satellite quantum wells) the number of electrons and holes are equal. This implies that with the formation of the satellite quantum wells at high temperatures, thermally excited electrons will occupy the bound states of the satellite quantum wells. This is supported by Figure 5.17 which is a plot of the first ten eigenfunctions of this device (not including the first eigenstate which is bound to the GaAs quantum well). These functions are clearly confined to the satellite quantum wells in barrier donor region. In the case where the barrier regions is completely doped, Section 5.2.2, these higher order wave functions are spread equally throughout the barrier region.

Table 5.3 lists the Fermi energy, the energy eigenvalues bound in the well region and the approximate width of the depletion region on either side of the quantum well. A comparison between this table and Table 5.2 for the completely doped barrier region, shows that both devices are identical for low temperatures. However, as temperature increases, the device with a restricted doner region exhibits well energy states which are significantly lower than those of the device with the barrier region which is completely doped. This is illustrated in Table 5.4.

Table 5.3: Fermi Energy, well energy eigenstate and approximate depletion region for a 100 Å, AlGaAs/GaAs/AlGaAs carrier confining quantum well with a Al impurity concentration of 0.35 and a restricted donor region with a concentration of 10^{18} cm^{-3} at different temperatures.

Temperature [K]	Fermi Energy [meV]	Well Energy State [meV]	Depletion Region [Å]
5	264.12	190.60	120
100	243.63	172.06	115
300	177.21	118.98	25

Table 5.4: Comparison beteen the well energy eigenstates for a 100 Å, AlGaAs/GaAs/AlGaAs carrier confining quantum well with a Al impurity concentration of 0.35 with a restricted donor region and a unrestricted donor region at different temperatures. The donor concentration is 10^{18} cm^{-3}

Temperature [K]	Unrestricted Donor Region [meV]	Restricted Donor Region [meV]
5	190.80	190.60
100	203.51	172.06
300	207.03	118.98

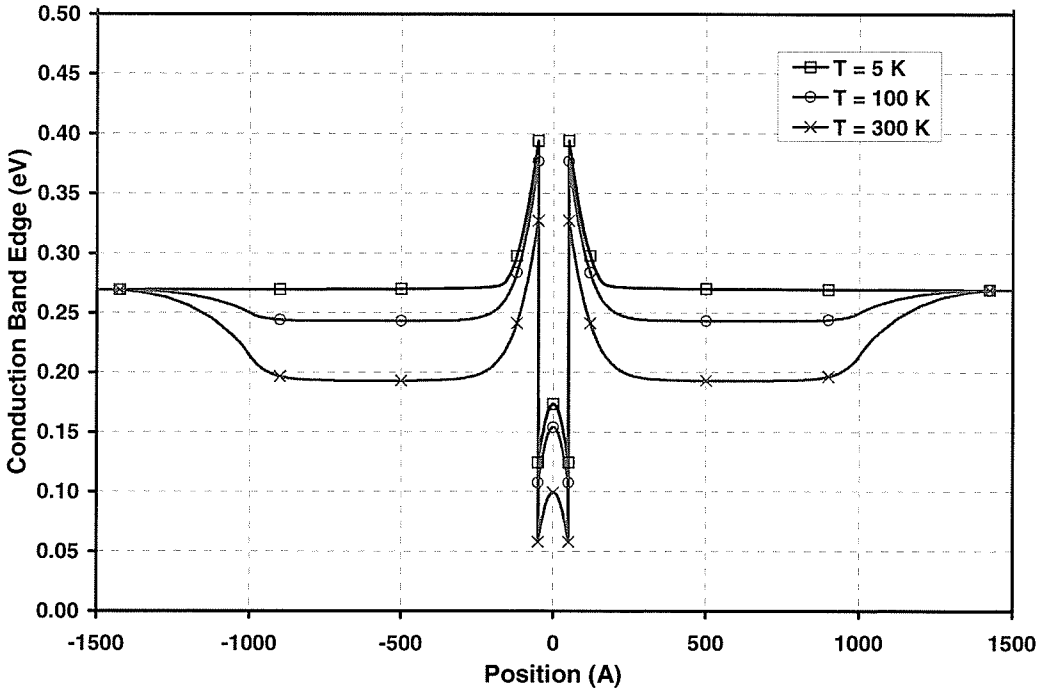

Figure 5.14: The effect of limited donors on the bending of the conduction band edge for a 100 Å wide GaAs quantum well with $Al_{0.35}Ga_{0.65}As$ barriers that are *n*-doped to 10^{18} cm^{-3}. The donor region only extends 950 Å on either side of the well region.

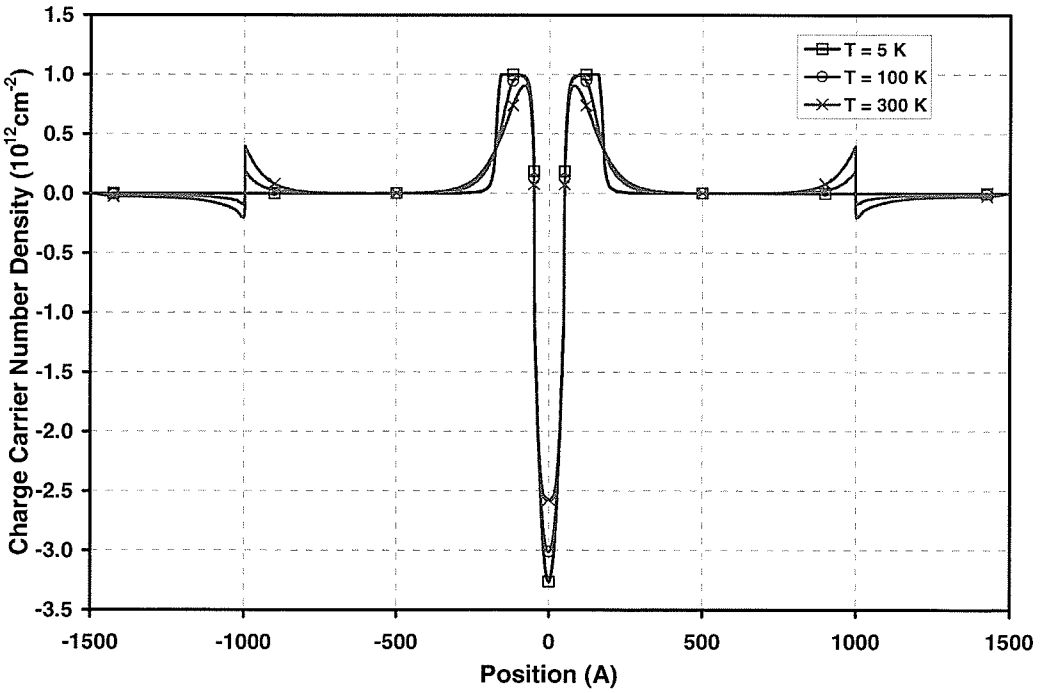

Figure 5.15: The effect of limited donors on the number density of electrons and holes for the quantum well heterostructure of Figure 5.14. A positive number density represents holes and a negative number density represents electrons.

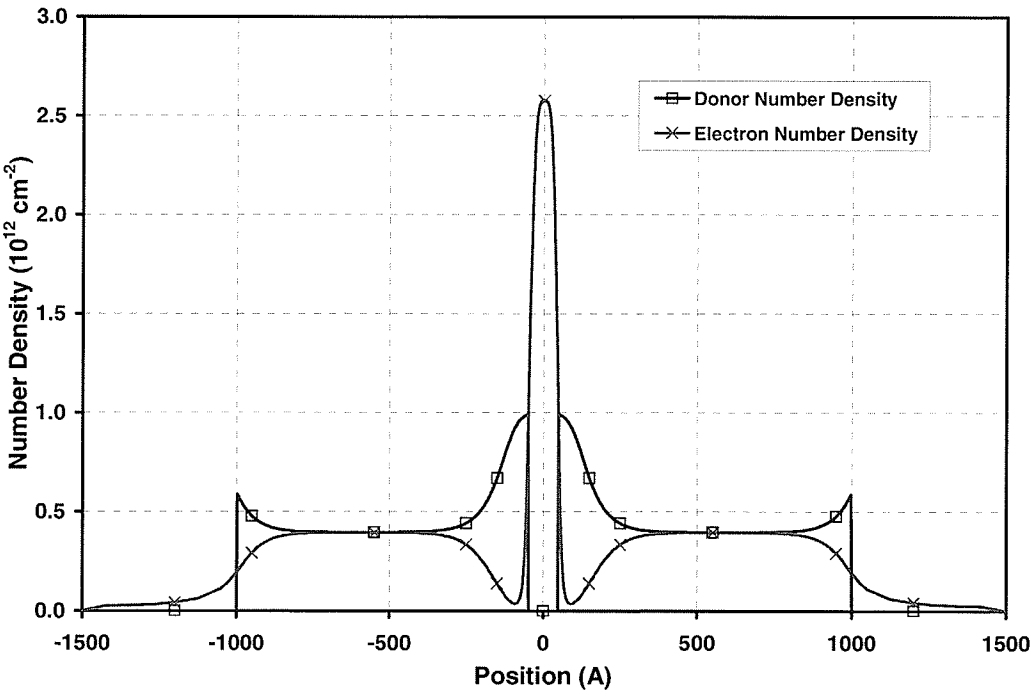

Figure 5.16: The effect of limited donors on the number density of electrons and holes for the quantum well heterostructure of Figure 5.14 at T = 300 K.

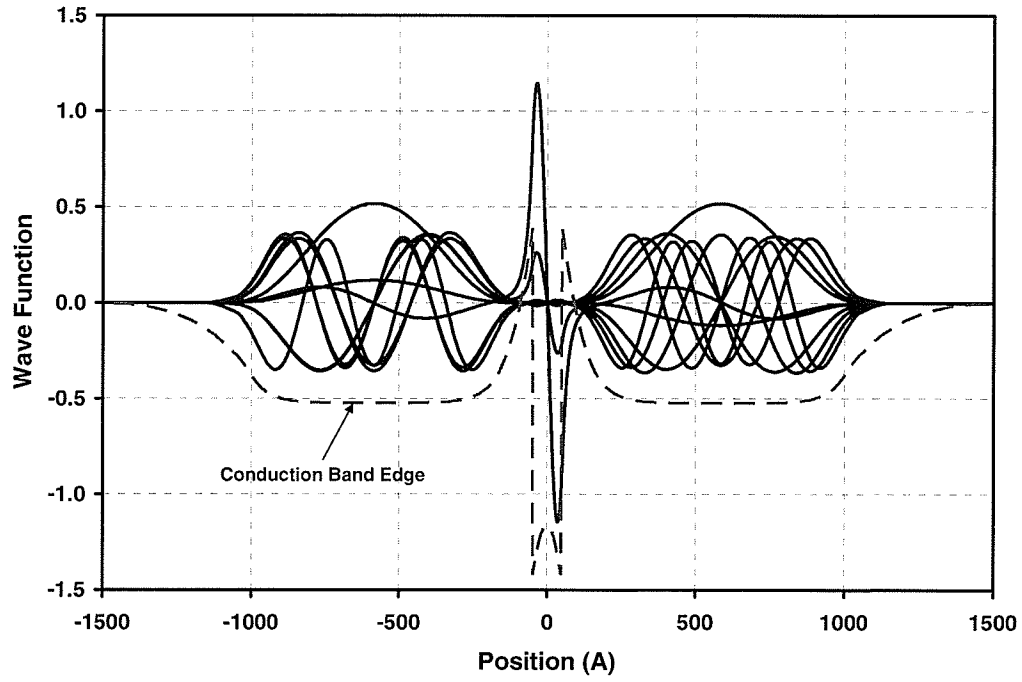

Figure 5.17: The first ten eigenfunctions for the quantum well heterostructure of Figure 5.14 at T = 300 K. These wave functions are clearly contained within the satellite quantum wells. The conduction band edge with satellite quantum wells is the dotted (red) line.

5.2.5 p-type Single Quantum Well

The self-consistent potential of a *p*-type modulation-doped $Al_{0.35}Ga_{0.65}As$/ $GaAs/Al_{0.35}Ga_{0.65}As$, 100 Å wide single quantum well is calculated for a *p*-doping concentration of 10^{19} cm^{-3}. At a temperature of 5 K, this corresponds to a bulk potential V_0 (valence band) with a 168 meV deep well. The valence band contains several different momentum modes (or bands) for holes including the heavy hole, light hole and, spin offset. Examination of all bands is called multi-band theory and involves coupled Schrödinger equations (one for each band). This is beyond the scope of this thesis and we will only consider a single band for heavy holes.

The self-consistent potential after considering the effect of heavy holes occupying the accessible states in the quantum well is shown in Figure 5.18. After the self-consistent calculation, this well is found to contain two distinct energy eigenvalues for the heavy holes confined in the well. The depletion region is about 30 Å on both sides of the well. Figure 5.19 shows the two wave electron wave functions corresponding to the two energy eigenstates. Inside the barrier regions the wave functions decay rapidly to zero implying that the heavy holes are confined to the well region only. The wave functions also indicate that this problem is really that of a double well. Holes are confined to the well region on either side of the centre 'hump' in the well.

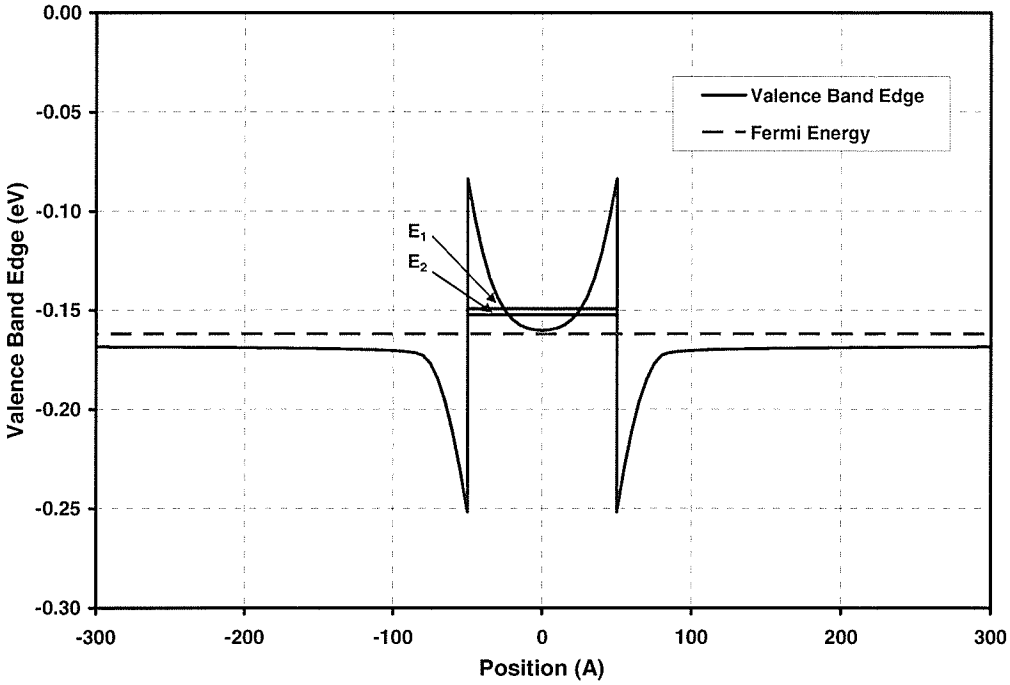

Figure 5.18: The valence band edge bending for a 100 Å, AlGaAs/GaAs/AlGaAs heavy-hole confining quantum well at T = 5 K and donor concentration of 10^{19} cm^{-3}. The corresponding heavy hole energy levels are also indicated.

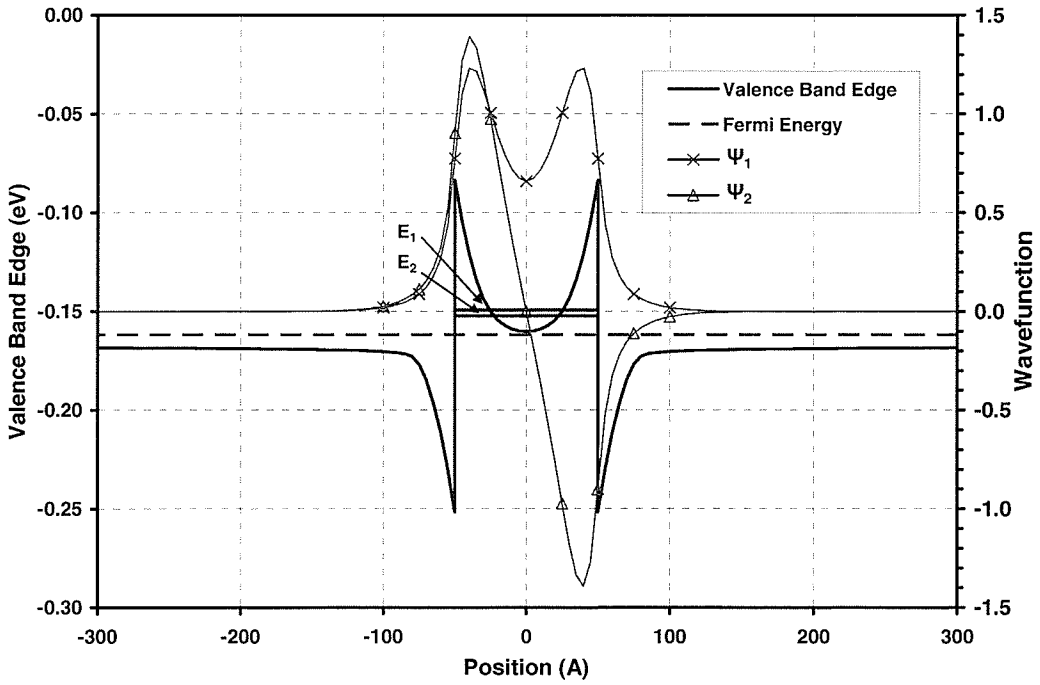

Figure 5.19: Wave functions corresponding to the heavy-hole energy eigenvalues for the quantum well of figure 5.18. Note the double well nature of the first wave function.

5.2.6 n-type Single Quantum Well with Non-Ohmic Metallic Contacts

The self-consistent potential of a *n*-type modulation-doped $Al_{0.35}Ga_{0.65}As$/ $GaAs/Al_{0.35}Ga_{0.65}As$, 100 Å wide single quantum well is calculated with metallic contacts on either side. The heterostructure is 3000 Å wide with a *n*-doping concentration of 10^{18} cm^{-3}, the heterostructure temperature was 5 K. The metallic contacts were Aluminum for this example (normally ohmic contacts are desired which reduces contact barrier to make a low resistance connection to the device).

At metal/semiconductor junctions the conduction band edge of the semiconductor bends so that the Fermi energy of the metal lines up with the Fermi energy of the semiconductor (recall that the Fermi energy of a metal lies within its conduction band). We will take the band bending between Aluminum and GaAs to be around 13.77 eV (this value varies greatly in the literature and depends on the manufacturing techniques, impurities, etc. [25] ,[26],[28]). This becomes the boundary condition for the Poisson solver.

The algorithm had to be modified to correctly account for the electrons which build up on the metal surface at the metal/semiconductor interface. This modification included calculating the depletion region at the device ends, the total number of holes then being the amount of electrons on the metal surface. These electrons were included in the algorithm which calculates the Fermi energy for charge neutralization.

Figure 5.20 shows the conduction band edge bending of the device. The 'spikes' in the conduction bend occur at the metal/semiconductor interface. Figure 5.21 shows the number density of holes and electrons (electron number density on the metal surface are not shown), clearly showing the depletion region in the heterostructure near the metal/semiconductor interface. Table 5.5 compares the Fermi energy, well energy eigenvalue and the depletion region near the GaAs well for metallic and infinite potential contacts. The table suggests that the infinite potential contacts (or boundary condition) used in the previous sections is

sufficient for most self-consistent calculations.

Table 5.5: A comparison of the Fermi Energy, well energy eigenvalue and approximate depletion region for different contacts.

Connector	Fermi Energy [meV]	Well Energy State [meV]	Depletion Region [Å]
Infinite Potential	264.32	190.80	120
Metallic	266.25	192.62	125

The solution for metallic contacts exhibited slightly poorer convergence and was simulated to a tolerance of $\tau < 7\ \mu\mathrm{eV}$. Extra elements had to be included at the boundaries to achieve acceptable tolerance and subsequently increased the computation time and number of iterations to convergence. These extra elements are necessary to properly model the band edge bending and to model the edge of the depletion region near the metal/semiconductor junction. Improved convergence can be achieved by adding more adaptive elements to this edge region and by developing a better algorithm to count the number of electrons accumulating on the metal surface.

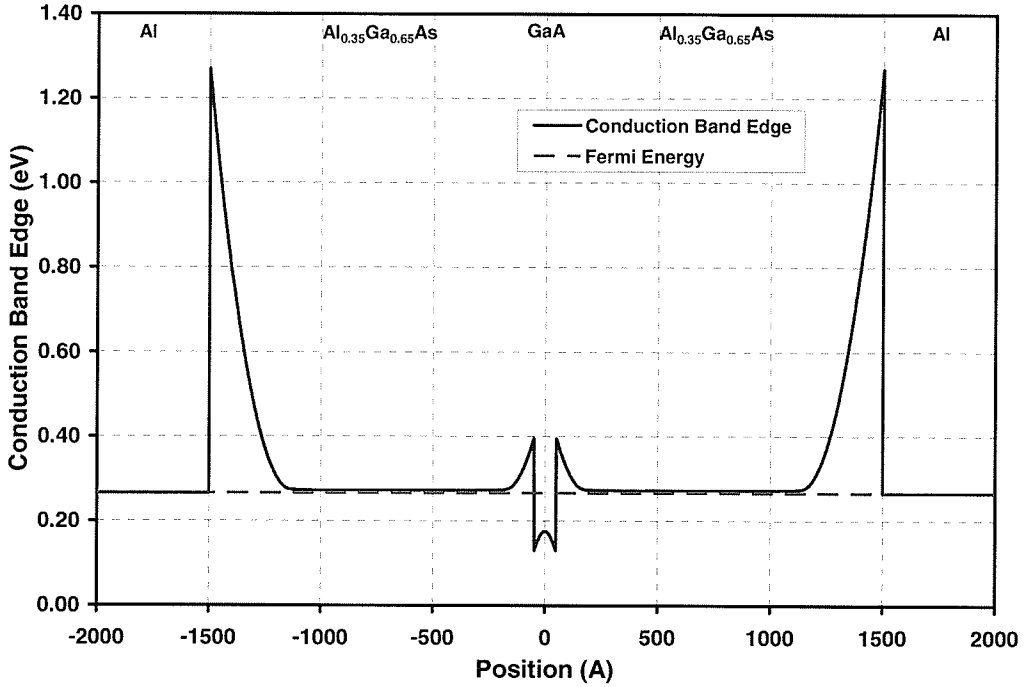

Figure 5.20: The conduction band edge bending of a 100 Å, AlGaAs/GaAs/AlGaAs electron confining quantum well heterostructure with Aluminum contacts. The device is at T = 5 K and has a donor concentration of 10^{18} cm^{-3}.

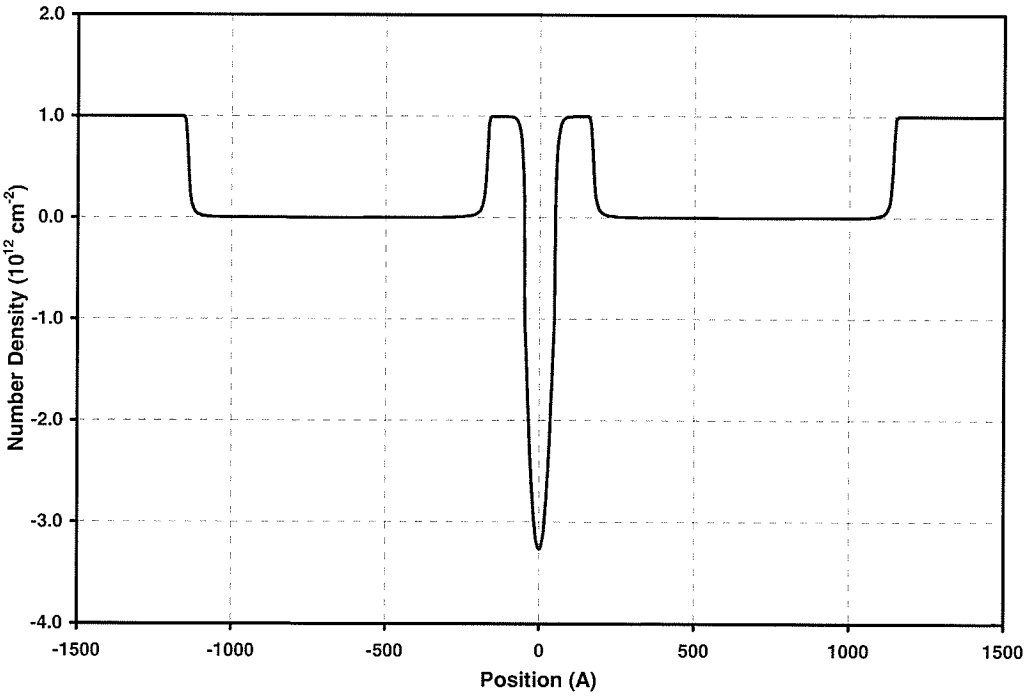

Figure 5.21: The number density of electrons and holes for the quantum well heterostructure with metallic contacts of Figure 5.20. A positive number density represents holes and a negative number density represents electrons.

5.3 Wave Function Engineering

As stated in the introduction wave function engineering promises to usher in a new generation of novel heterostructure devices. We will provide two simple examples of wave function engineering. First we will examine one method used to control the shape of the wave function and secondly we will examine a method to control electron tunnelling.

5.3.1 Asymmetric Quantum Well

The self-consistent potential of a *n*-type modulation-doped asymmetric quantum well with a *n*-doping concentration of 10^{18} cm^{-3} is calculated, the heterostructure temperature was 100 K. The device is composed of the following layers, a 1450 Å wide $Al_{0.35}Ga_{0.65}As$ barrier region, a 50 Å wide GaAs well region, a 50 Å wide $Al_{0.15}Ga_{0.85}As$ well region followed by another 1450 Å wide $Al_{0.35}Ga_{0.65}As$ barrier region. Both devices are contained in an infinite potential barrier region with the donors restricted to the 1450 wide $Al_{0.35}Ga_{0.65}As$ barrier regions.

Figure 5.22 shows the conduction band edge with the wave function and energy eigenstate overlayed. The peak of the wave function is shifted over to coincide with the 'deeper' GaAs well. Table 5.6 compares the Fermi energy, the energy eigenstate and the depletion region for the square well of Section 5.2.3 and the asymmetric well. We find that the Fermi level remained relatively constant. However, the energy eigenstates change as well shape changes. Thus by grading the edges of the quantum well we can control the shape of the wave function and the energy levels of a quantum well device. This is useful in a physical device by providing a means to control the distribution of charge in the device and the states available for transitions.

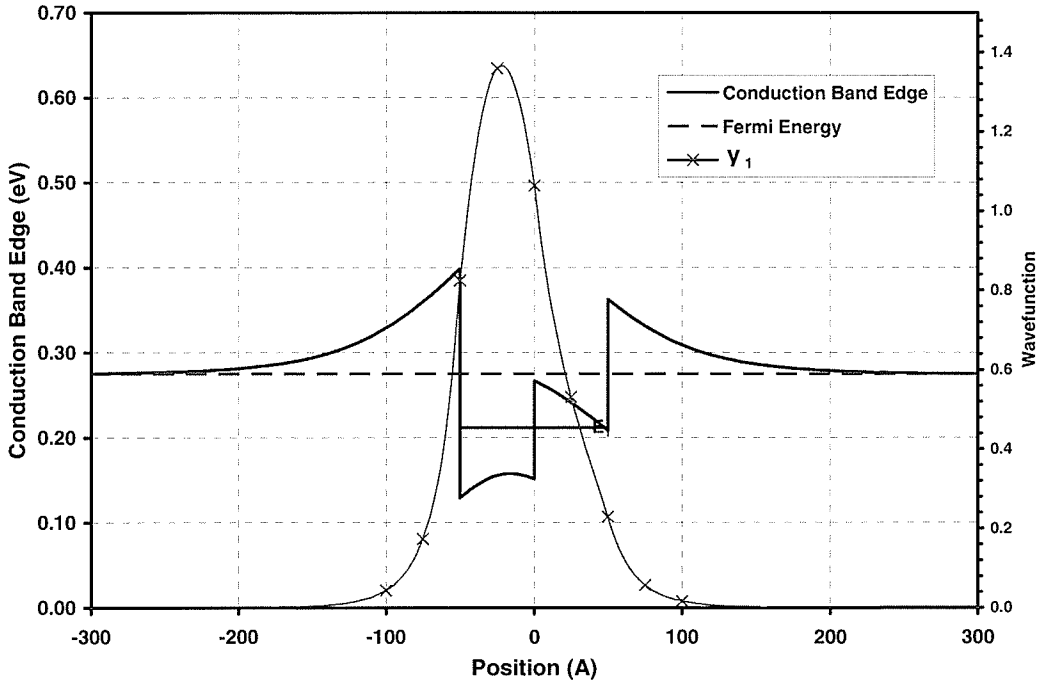

Figure 5.22: The conduction band edge bending of an asymmetric quantum well. The device is at T = 100 K and has a donor concentration of 10^{18} cm^{-3}. The wave function and corresponding energy eigenvalue are overlayed. The Fermi energy is indicated by the dashed line.

Table 5.6: A comparison of the Fermi Energy, well energy eigenvalue and approximate depletion region for a square well and the asymmetric well of Section 5.3.1.

Well Type	Fermi Energy [meV]	Well Energy State [meV]	Depletion Region [Å]
Square	275.08	203.51	115
Asymmetric	275.08	211.76	110

5.3.2 Double Quantum Well

The self-consistent potential of a *n*-type modulation-doped double quantum well with a *n*-doping concentration of 10^{18} cm^{-3} is calculated. The heterostructure temperature was 100 K. Three different double well structures will be compared. The first device is composed of the following layers, a 1450 Å wide $Al_{0.35}Ga_{0.65}As$ barrier region, a 35 Å wide GaAs well region, a 30 Å wide $Al_{0.35}Ga_{0.65}As$ barrier region, a 35 Å wide GaAs well region, followed by another 1450 Å wide $Al_{0.35}Ga_{0.65}As$ barrier region. The second device is composed of the following layers, a 1450 Å wide $Al_{0.35}Ga_{0.65}As$ barrier region, a 35 Å wide GaAs well region, a 30 Å wide $Al_{0.50}Ga_{0.50}As$ barrier region, a 35 Å wide GaAs well region, followed by another 1450 Å wide $Al_{0.35}Ga_{0.65}As$ barrier region. The third device is composed of the following layers, a 1450 Å wide $Al_{0.35}Ga_{0.65}As$ barrier region, a 35 Å wide GaAs well region, a 30 Å wide $Al_{0.65}Ga_{0.65}As$ barrier region, a 35 Å wide $Al_{0.15}Ga_{0.85}As$ well region, followed by another 1450 Å wide $Al_{0.35}Ga_{0.65}As$ barrier region. All devices were contained in an infinite potential barrier region with the donors restricted to the 1450 wide $Al_{0.35}Ga_{0.65}As$ barrier regions. In the first two examples the main difference is the height of the centre barrier. In the third example one quantum well (right hand well) is not as deep as the first (left hand well).

The conduction band edge with an overlay of the wave function, Fermi energy, and the well energy eigenstates are shown in Figures 6.23, 6.24 and 6.25 for the $Al_{0.35}Ga_{0.65}As/GaAs/Al_{0.35}Ga_{0.65}As/GaAs/Al_{0.35}Ga_{0.65}As$, $Al_{0.35}Ga_{0.65}As/GaAs/Al_{0.50}Ga_{0.50}As/GaAs/Al_{0.35}Ga_{0.65}As$, and $Al_{0.35}Ga_{0.65}As/GaAs/Al_{0.65}Ga_{0.65}As/Al_{0.15}Ga_{0.85}As/Al_{0.35}Ga_{0.65}As$ double well heterostructure devices respectively. With the smaller centre barrier electrons bound in the well are more likely to tunnel between the first two wells as indicated by the shape of the wave functions. Electrons are clearly confined in the left well for the example third well. These examples illustrate some techniques which can be employed to design a simple resonant tunnelling diode.

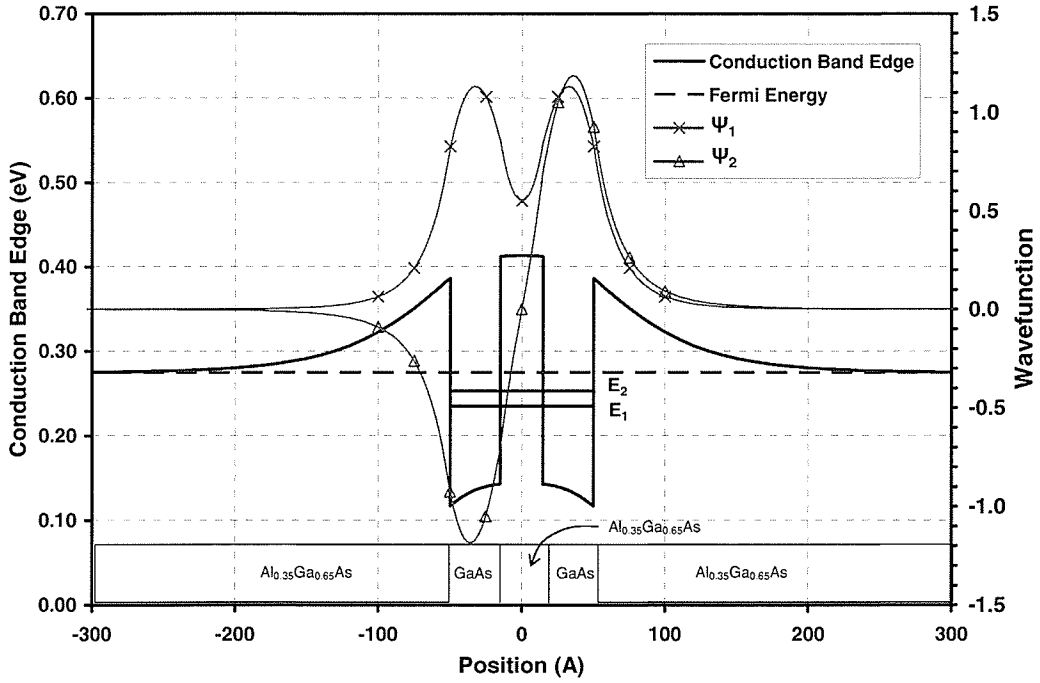

Figure 5.23: The conduction band edge, Fermi energy, wave functions and energy eigenvalues of a $Al_{0.35}Ga_{0.65}As/GaAs/Al_{0.35}Ga_{0.65}As/GaAs/Al_{0.35}Ga_{0.65}As$ double quantum well heterostructure at T = 100 K and donor concentration of 10^{18} cm^{-3}.

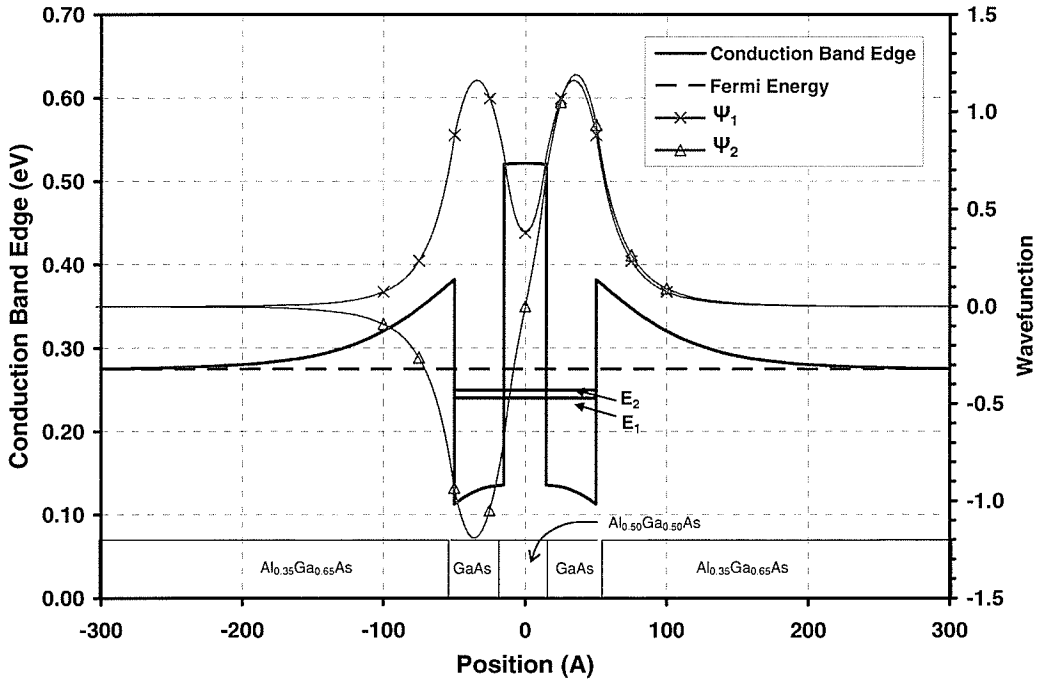

Figure 5.24: The conduction band edge, Fermi energy, wave functions and energy eigenvalues for a $Al_{0.35}Ga_{0.65}As/GaAs/Al_{0.50}Ga_{0.50}As/GaAs/Al_{0.35}Ga_{0.65}As$ double quantum well heterostructure at T = 100 K and donor concentration of 10^{18} cm^{-3}.

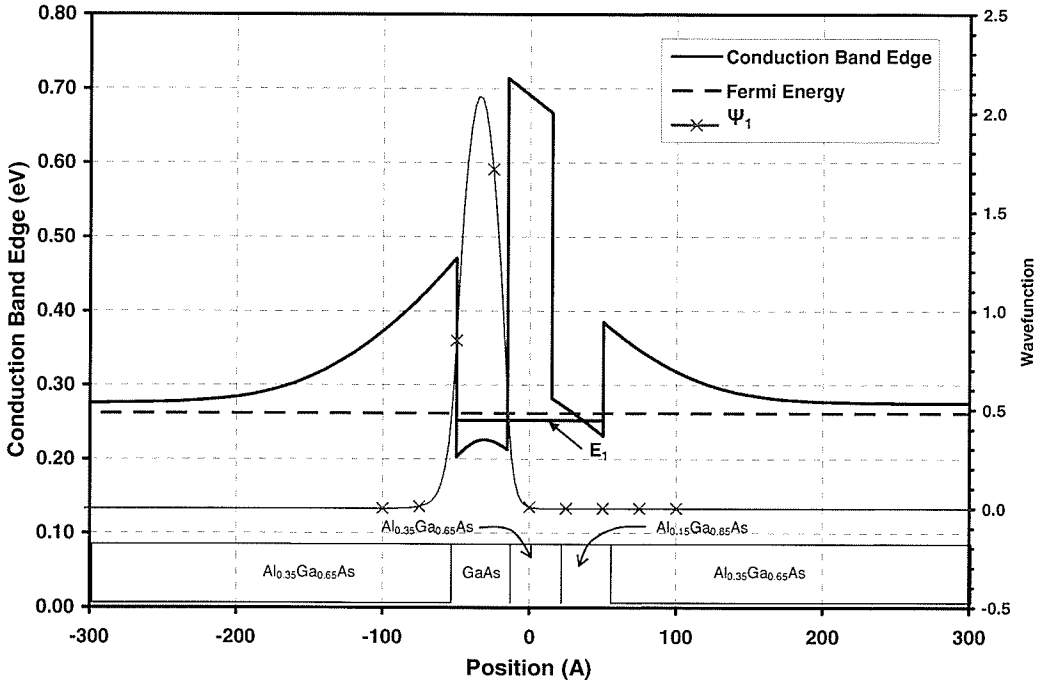

Figure 5.25: The conduction band edge, Fermi energy, wave functions and energy eigenvalues of a $Al_{0.35}Ga_{0.65}As/GaAs/Al_{0.65}Ga_{0.65}As/GaAs/Al_{0.15}Ga_{0.85}As/Al_{0.35}Ga_{0.65}As$ double quantum well heterostructure at T = 100 K and donor concentration of 10^{18} cm^{-3}.

6) Conclusions

The self-consistent algorithm was found to be robust when used to model a variety of heterostructure geometries, temperatures, acceptor/donor dopings, and initial seed potentials. The self-consistent solution yields not only the band edge bending, but also the quantum well energy levels and their corresponding wave functions. The wave functions and energy levels are key to the modelling and design of quantum well devices including tunnelling diodes and lasers. We can make the following conclusions:

1. The finite element method with Hermite shape functions lends itself well to self-consistently solving the Schrödinger-Poisson equations for the band structure of quantum well heterostructure devices. These shape functions naturally satisfy the continuity of the probability current across element boundaries. The same element pattern can be successfully used to solve both the Schrödinger and Poisson equations.

2. Decoupling the Schrödinger and Poisson equations by developing an approximate expression which relates the dependence of the charge carrier number density on the potential leads to superior solution convergence over attempts at a direct solution using the exact expression. This enables us to use an inner and faster iteration loop to solve for the change in the potential function and at the same time predict how the charge carrier number density varies from iteration to iteration as the potential function changes. The charge density can then be corrected by solving the Schrödinger eigenvalue equation in an outer and slower loop.

3. For the more realistic case of a physical device which is of finite extent and bound either by air/vacuum or metallic contacts, more elements and

subsequently more iterations are required to achieve a desired solution tolerance . A device which is of finite extent can be approximated by infinite potential boundaries and then requires the solution of the bound states in the 'barrier' regions. Adequate modelling of the 'barrier' regions becomes increasingly important for high temperatures and for the case of limited donor doping regions where 'satellite' quantum wells then form. More elements are required to adequately model the increasingly oscillatory wave functions of these bound states. Historically, these 'barrier' states were treated using either a classical expression for the charge carrier density or by a free electron solution (unbound problem), this is one of the features that this modelling approach offers.

Future work:

1. Develop an adaptive mesh algorithm which can potentially reduce the number of elements used in the solution yet maintain solution tolerance.

2. Extend the Schrödinger formulation to include a multi-band model of the heavy-hole, light-hole, spin-split offset valence bands and higher level conduction bands. This will enable the modelling of complex quantum well lasers and other optical devices.

3. Extending the algorithm to a 2 and 3-D model would further enable the modelling and design of novel quantum heterostructure devices such as quantum wires and quantum transistors.

Appendix A

Programming Considerations

Matrix Formulation:

The finite element solution to a partial differential equation involves reducing the problem into the matrix form $\mathbf{A}\psi = \mathbf{B}$ where we are solving for the unknown vector ψ. This matrix equation is defined over the entire domain of the problem,

$$\begin{pmatrix} a_{11} & a_{12} & \dots & a_{1N} \\ a_{21} & a_{22} & \dots & a_{2N} \\ \vdots & \vdots & \ddots & \vdots \\ a_{N1} & a_{N2} & \dots & a_{NN} \end{pmatrix} \begin{pmatrix} \psi_1 \\ \psi_2 \\ \vdots \\ \psi_N \end{pmatrix} = \begin{pmatrix} b_1 \\ b_2 \\ \vdots \\ b_N \end{pmatrix} \tag{A1}$$

where we defined,

$$a_{ij} = A\left(\varphi_i(x), \varphi_j(x)\right) = \left\{ \begin{array}{l} \int_\Omega \left[\frac{d}{dx}\varphi_i(x) \frac{d}{dx}\varphi_j(x) + t(x)\varphi_i(x)\varphi_j(x) \right] dx \\ + \varphi_i(x) \frac{d}{dx}\varphi_j(x)\Big|_{\Gamma_N} \end{array} \right\}, \tag{A2}$$

$$b_i = B\left(\varphi_i(x)\right) = \int_\Omega \left[r(x)\varphi_i(x) \right] dx.$$

Recall from Section 2.6 that we defined the shape functions $\varphi_i(x)$ locally over a standard element. First this means that the shape functions are really defined in terms of the local element coordinates ξ, thus we will have to map them to the global coordinate system. Secondly this means when we implement equation (A2), the we should really set the limits of integration to be over one element only and therefore generate a set of elemental matrix equations which we will later map into the global matrix of equation (A1). In terms of local elemental coordinates

we can write equation (A2) as,

$$a_{ij}^{(m)} = A^{(m)}\left(\varphi_i(\xi),\varphi_j(\xi)\right) = \left\{ \int_{\Omega^{(m)}} \left[\begin{array}{l} \left(\frac{d}{d\xi}\varphi_i(\xi)\frac{d\xi}{dx}\right)\left(\frac{d}{d\xi}\varphi_j(\xi)\frac{d\xi}{dx}\right) + \\ t\left(x^{(m)}(\xi)\right)\varphi_i(\xi)\varphi_j(\xi) \\ \qquad + \varphi_i(\xi)\frac{d}{d\xi}\varphi_j(\xi)\frac{d\xi}{dx}\Big|_{\Gamma_N} \end{array} \right] \left|J^{(m)}\right| d\xi \right\} \quad \textbf{(A3)}$$

$$b_i^{(m)} = B^{(m)}\left(\varphi_i(\xi)\right) = \int_{\Omega} \left[r\left(x^{(m)}(\xi)\right)\varphi_i(\xi) \right] d\xi$$

where $J^{(m)}$ is the Jacobian of the m^{th} element given by,

$$\left|J^{(m)}\right| = \left|\frac{d}{d\xi}x^{(m)}(\xi)\right| = \left|\frac{1}{2}\left(x_2^{(m)} - x_1^{(m)}\right)\right|. \quad \textbf{(A4)}$$

and x_1 and x_2 are the end points of the m^{th} element. Historically the finite element method has been first used by the field of mechanical engineering and have identified the following matrices which allow flexibility when programming [9],[32],[33]. These equations come directly from Equation (A3); the stiffness matrix for the m^{th} element,

$$\mathscr{K}_{\ell,k}^{(m)} = \int_{-1}^{+1} \left(\frac{d}{d\xi}\varphi_\ell(\xi)\frac{d\xi}{dx}\right)\left(\frac{d}{d\xi}\varphi_k(\xi)\frac{d\xi}{dx}\right)\left|J^{(m)}\right| d\xi. \quad \textbf{(A5)}$$

The mass matrix for the m^{th} element,

$$\mathscr{M}_{\ell,k}^{(m)} = \int_{-1}^{+1} c\left(x^{(m)}(\xi)\right)\varphi_\ell(\xi)\varphi_k(\xi)\left|J^{(m)}\right| d\xi. \quad \textbf{(A6)}$$

The load vector for the m^{th} element,

$$\mathscr{F}_\ell^{(m)} = \int_{-1}^{+1} f\left(x^{(m)}(\xi)\right)\varphi_\ell(\xi)\left|J^{(m)}\right| d\xi. \quad \textbf{(A7)}$$

Neumann boundary conditions are considered in the linear functional,

$$\mathscr{G}_{\ell,k}^{(m)} = \varphi_\ell(\xi)\frac{d}{dx}\varphi_k(\xi)\Big|_{\Gamma_N} \tag{A8}$$

where λ, k for all equations are summed over all the local shape functions as defined on the local element. Each row and column of the above matricies corresponds to a specific combination of the local shape functions. The local matrix equation terms are given by,

$$\begin{aligned} \mathbf{A}^{(m)} &= \mathscr{K}^{(m)} + \mathscr{M}^{(m)} + \mathscr{G}^{(m)}, \\ \mathbf{B}^{(m)} &= \mathscr{F}^{(m)}. \end{aligned} \tag{A9}$$

Using this formulation has many advantages as error analysis and certain boundary conditions require access and/or changes to the elements of the mass or stiffness matrices.

Populating The Global Matrix:

Section 2.8 illustrates how to map the local matrices to the global matrices. This mapping is dependant upon the shape functions used in the problem formulation. Simply put for the one dimensional problem shape functions defined on the common node between two neighbouring elements must be matched up. The corresponding matrix elements of the local matrices are then added together in the global matrix.

Due to the conditions presented in Section 2.6 for the shape functions, the global matrix $\mathbf{A}$ is sparse and diagonal. The application of boundary conditions may however break the symmetry of the matrix.

Dirichlet Boundary Conditions:

For the one dimensional case there are only two nodes which boundary conditions can be applied to, these are the first and last nodes of the domain. Dirichlet boundary conditions are imposed after the global matrices have been assembled. The procedure of applying Dirichlet boundary conditions involves multiplying the column of the global **A** matrix which corresponds to the shape function of the boundary node by the Dirichlet boundary value, this column is then transferred to the right had side of equation (A1) by adding it (with the appropriate sign) to the corresponding elements of the **B** vector. Next the elements for the row of the global **A** matrix that correspond to the boundary node shape function are set to zero. We next set element of the **B** vector that corresponds to the shape function of the boundary node to the Dirichlet boundary value. This is ensures that the solution composed of the summation of basis functions over that node, $\Psi(x_{\Gamma_D}) = \sum_{i=1}^{N} c_i \varphi_i(x_{\Gamma_D})$, is equal to the Dirichlet boundary value. Finally the diagonal elements of the global **A** matrix are set to one.

Consider the following two element example of Figure (A1). The shape functions are cubic Hermite polynomials; meaning two degrees of freedom per node. Let the boundary conditions of the end nodes be $\Psi(x_1) = g_1$ and $\Psi(x_3) = g_2$. Note that we have not specified any value for the derivative terms at the endpoints.

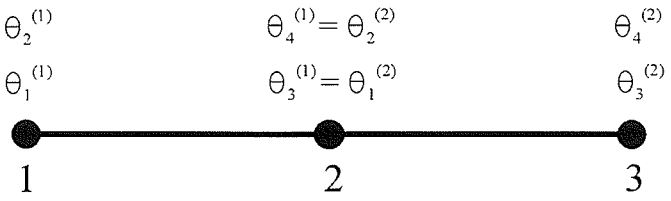

Figure A1: Two element problem with cubic Hermit polynomials. Dirichlet boundary conditions are on the end nodes, 1 and 3.

Applying the procedure presented above for the Dirichlet boundary conditions the global matrix equation becomes,

$$\begin{pmatrix} 1 & 0 & 0 & 0 & 0 & 0 \\ 0 & a_{22} & a_{23} & a_{24} & 0 & a_{26} \\ 0 & a_{32} & a_{33} & a_{34} & 0 & a_{36} \\ 0 & a_{42} & a_{43} & a_{44} & 0 & a_{46} \\ 0 & 0 & 0 & 0 & 1 & 0 \\ 0 & a_{62} & a_{63} & a_{64} & 0 & a_{66} \end{pmatrix} \begin{pmatrix} \psi_1 \\ \psi_2 \\ \psi_3 \\ \psi_4 \\ \psi_5 \\ \psi_6 \end{pmatrix} = \begin{pmatrix} -g_1 \\ b_2 - a_{21}\, g_1 - a_{25}\, g_2 \\ b_3 - a_{31}\, g_1 - a_{35}\, g_2 \\ b_4 - a_{41}\, g_1 - a_{45}\, g_2 \\ -g_2 \\ b_6 - a_{61}\, g_1 - a_{65}\, g_2 \end{pmatrix} \tag{A10}$$

in which we solve for the vector ψ.

Neumann Boundary Conditions:

Neumann boundary conditions are considered in the term,

$$\mathcal{G}^{(m)}\psi^{(m)} = \varphi_\ell(\xi)\sum_{k=1}^{N}\psi_k \tfrac{d}{dx}\varphi_k(\xi)\Big|_{\Gamma_N} \tag{A11}$$

where N is the total number of global shape functions. From the definitions of the Hermite shape functions $\varphi_i(x)$ we can recognize that this term is zero for all ℓ, k except for ℓ and k which correspond to the first and last nodes, x_l and x_r, where this term reduces to ψ_k. Thus we can write this term as,

$$\varphi_{N-1}(x_r)\psi_N \tfrac{d}{dx}\varphi_N(x_r) - \varphi_1(x_l)\psi_2 \tfrac{d}{dx}\varphi_2(x_l) \tag{A12}$$

where N is the total number of global shape functions. In matrix form (local matrix) this can we written as,

$$\begin{pmatrix} 0 & -1 & \cdots & 0 & 0 \\ 0 & 0 & \cdots & 0 & 0 \\ \vdots & \vdots & \ddots & \vdots & \vdots \\ 0 & 0 & \cdots & 0 & 1 \\ 0 & 0 & \cdots & 0 & 0 \end{pmatrix} \begin{pmatrix} \psi_1 \\ \psi_2 \\ \vdots \\ \psi_{N-1} \\ \psi_N \end{pmatrix}. \tag{A13}$$

Which is easily incorporated into the global **A** matrix as below,

$$\begin{pmatrix} a_{11} & a_{12}-1 & \cdots & a_{1,N-1} & a_{1,N} \\ a_{21} & a_{22} & \cdots & a_{2,N-1} & a_{2,N} \\ \vdots & \vdots & \ddots & \vdots & \vdots \\ a_{N-1,1} & a_{N-1,2} & \cdots & a_{N-1,N-1} & a_{N-1,N}+1 \\ a_{N,1} & a_{N,2} & \cdots & a_{N,N-1} & a_{N,N} \end{pmatrix} \begin{pmatrix} \psi_1 \\ \psi_2 \\ \vdots \\ \psi_{N-1} \\ \psi_N \end{pmatrix} = \begin{pmatrix} b_1 \\ b_2 \\ \vdots \\ b_{N-1} \\ b_N \end{pmatrix}. \tag{A14}$$

Appendix B

Example Implementing the Finite Element Algorithm

Consider the square well potential, the Schrödinger Equation for the one dimension square well is given by,

$$\frac{-\eta^2}{2m}\frac{d^2\Psi(x)}{dx^2}+V(x)\Psi(x)=E\,\Psi(x) \qquad \textbf{(B1)}$$

where the potential for a well is given by,

$$V(x)=\begin{cases} V_0 & \text{for } x\le \frac{-\lambda}{2} \text{ and } \quad x\le \frac{\lambda}{2} \\ 0 & \text{for } \frac{-\lambda}{2}<x<\frac{\lambda}{2} \end{cases} \qquad \textbf{(B2)}$$

and ℓ is the width of the well. The problem we are interested in here is for the case when $E<V_0$, which corresponds to a neutral particle trapped inside of the potential well. This is an eigenvalue problem where E is an eigenvalue, and $\Psi(x)$ is the corresponding eigenfunction.

Using the procedure of Section 2, equation (B1) is converted into the weak form by multiply through by arbitrary test functions $\varphi_n(x)$, integrating over the domain Ω, and then integrating by parts to yield,

$$\int_\Omega\left[\tfrac{d}{dx}\varphi_n(x)\tfrac{d}{dx}\Psi(x)+\frac{2m}{\hbar^2}\left(V(x)-E\right)\varphi_n(x)\Psi(x)\right]dx-\varphi_n(x)\tfrac{d}{dx}\Psi(x)\Big|_{B.C.}=0. \qquad \textbf{(B3)}$$

The last term is the Neumann boundary conditions; for the one dimensional quantum well there are no Neumann boundary conditions to impose so this term is set to zero.

Using Galerkin's method we chose the weighting functions to be the same as the basis or shape functions, $\theta(x) = \varphi(x)$ to get a solution of the form,

$$\Psi(x) = \sum_{i=1}^{N} c_i \varphi_i(x). \tag{B4}$$

Substituting the solution, Equation (B4) into Equation (B3) yields,

$$\sum_{j=1}^{N} \int_{\Omega} \left[\tfrac{d}{dx}\varphi_i(x)\, c_j \tfrac{d}{dx}\varphi_j(x) + \frac{2m}{\hbar^2} V(x)\, \varphi_i(x)\, c_j \varphi_j(x) \right] dx = \sum_{j=1}^{N} \int_{\Omega} \frac{2m}{\hbar^2} E\, \varphi_i(x)\, c_j\, \varphi_j(x)\, dx. \tag{B5}$$

Writing Equation (B5) as a matrix equation where the elements of the matricies are given by,

$$\left.\begin{aligned} A_{ij} &= \sum_{j=1}^{N} \int_{\Omega} \left[\tfrac{d}{dx}\varphi_i(x) \tfrac{d}{dx}\varphi_j(x) + \frac{2m}{\hbar^2} V(x)\, \varphi_i(x)\, \varphi_j(x) \right] dx \\ D_{ij} &= \sum_{j=1}^{N} \int_{\Omega} \left[\frac{2m}{\hbar^2} \varphi_i(x)\, \varphi_j(x) \right] dx \end{aligned}\right\} \tag{B6}$$

and the c_j form a vector of unknowns. In matrix form we must solve the eigenvalue equation,

$$\mathbf{A}\mathbf{c} = E\mathbf{D}\mathbf{c}, \tag{B7}$$

for the unknown eigenvalues E and eigenvector $\mathbf{c}$.

Populating the Matrix Equation.

Populating the matrix equation first requires us to divide the domain into sub-domains or elements. The choice of elements is arbitrary except for the condition that every element must contain only one type of region (or media). This implies that region boundaries must coincide with element boundaries. At a minimum the square well problem requires three elements, one for each region. To illustrate the process of populating the matrix equation we will divided the domain into three elements. Our choice of three elements means that the first element is

composed entirely of the left hand potential barrier, the second element is entirely inside of the well region, and the third element is entirely composed of the right hand potential barrier.

For illustrative purposes we will use cubic Hermite interpolation polynomials as our shape or test functions. This will reduce the number of degrees of freedom we have to keep track of, as there are 4 polynomials per element (two nodes and two degrees of freedom per node). Recall from Chapter 2 that the test functions are defined on a standard local element and we use the mapping function of equation (2.23) to map the local coordinates to global coordinates. Thus can re-write equation (B6) as elemental matrices,

$$\left.\begin{aligned} A_{ij}^{(k)} &= \sum_{j=1}^{4} \int_{-1}^{+1} \left[\tfrac{d}{dx}\varphi_i(x) \tfrac{d}{dx}\varphi_j(x) + \frac{2m^{(k)}}{\hbar^2} V^{(k)}(x)\varphi_i(x)\varphi_j(x) \right] dx \\ D_{ij}^{(k)} &= \sum_{j=1}^{4} \int_{-1}^{+1} \left[\frac{2m^{(k)}}{\hbar^2} V^{(k)}(x)\varphi_i(x)\varphi_j(x) \right] dx \\ c_j &= c_j^{(k)} \end{aligned}\right\} \qquad \textbf{(B8)}$$

where k is the index telling us which element we are on. The matrices of Equation (B8) are 4×4 matrices defined on the k^{th} element,

$$\mathbf{A}^{(k)} = \begin{pmatrix} A_{11}^{(k)} & A_{12}^{(k)} & A_{13}^{(k)} & A_{14}^{(k)} \\ A_{21}^{(k)} & A_{22}^{(k)} & A_{23}^{(k)} & A_{24}^{(k)} \\ A_{31}^{(k)} & A_{32}^{(k)} & A_{33}^{(k)} & A_{34}^{(k)} \\ A_{41}^{(k)} & A_{42}^{(k)} & A_{43}^{(k)} & A_{44}^{(k)} \end{pmatrix},$$

$$\mathbf{D}^{(k)} = \begin{pmatrix} D_{11}^{(k)} & D_{12}^{(k)} & D_{13}^{(k)} & D_{14}^{(k)} \\ D_{21}^{(k)} & D_{22}^{(k)} & D_{23}^{(k)} & D_{24}^{(k)} \\ D_{31}^{(k)} & D_{32}^{(k)} & D_{33}^{(k)} & D_{34}^{(k)} \\ D_{41}^{(k)} & D_{42}^{(k)} & D_{43}^{(k)} & D_{44}^{(k)} \end{pmatrix}, \qquad \textbf{(B9-a)}$$

and

$$\mathbf{c}^{(k)} = \begin{pmatrix} c_1^{(k)} \\ c_2^{(k)} \\ c_3^{(k)} \\ c_4^{(k)} \end{pmatrix}. \qquad \textbf{(B9-b)}$$

We map from the local matrices of equation (B9) to the global matrix of equation (B7) using the mapping tables of Section 2.8. Figure B1 illustrates the mappings for our three element square well problem. Using cubic Hermite polynomials for the local shape functions will correspond to eight global shape functions. The mapping table between local and global shape function is given in Table B1 below.

Table B1: Shape Function Mapping Table

Local Shape Function Index	Element Number	Global Shape Function Index
1	1	1
2	1	2
3	1	3
4	1	4
1	2	3
2	2	4
3	2	5
4	2	6
1	3	5
2	3	6
3	3	7
4	3	8

The local matrices of equation (B9) are overlayed into a global matrix such that those local matrix entries (matrix element) which correspond to the same local shape function on neighbouring elements are summed into one global matrix entry. Using Table B1 we can write the global matrix equation as the sum of the entries from the element matrices of equation (B9),

$$\begin{pmatrix} A_{11}^1 & A_{12}^1 & A_{13}^1 & A_{14}^1 & 0 & 0 & 0 & 0 \\ A_{21}^1 & A_{22}^1 & A_{23}^1 & A_{24}^1 & 0 & 0 & 0 & 0 \\ A_{31}^1 & A_{32}^1 & A_{33}^1 + A_{11}^2 & A_{34}^1 + A_{12}^2 & A_{13}^2 & A_{14}^2 & 0 & 0 \\ A_{41}^1 & A_{42}^1 & A_{43}^1 + A_{21}^2 & A_{44}^1 + A_{22}^2 & A_{23}^2 & A_{24}^2 & 0 & 0 \\ 0 & 0 & A_{31}^2 & A_{32}^2 & A_{33}^2 + A_{11}^3 & A_{34}^2 + A_{12}^3 & A_{13}^3 & A_{14}^3 \\ 0 & 0 & A_{41}^2 & A_{42}^2 & A_{43}^2 + A_{21}^3 & A_{44}^2 + A_{22}^3 & A_{23}^3 & A_{24}^3 \\ 0 & 0 & 0 & 0 & A_{31}^3 & A_{32}^3 & A_{33}^3 & A_{34}^3 \\ 0 & 0 & 0 & 0 & A_{41}^3 & A_{42}^3 & A_{43}^3 & A_{44}^3 \end{pmatrix} \begin{pmatrix} c_1 \\ c_2 \\ c_3 \\ c_4 \\ c_5 \\ c_6 \\ c_7 \\ c_8 \end{pmatrix} =$$

$$E \begin{pmatrix} D_{11}^1 & D_{12}^1 & D_{13}^1 & D_{14}^1 & 0 & 0 & 0 & 0 \\ D_{21}^1 & D_{22}^1 & D_{23}^1 & D_{24}^1 & 0 & 0 & 0 & 0 \\ D_{31}^1 & D_{32}^1 & D_{33}^1 + D_{11}^2 & D_{34}^1 + D_{12}^2 & D_{13}^2 & D_{14}^2 & 0 & 0 \\ D_{41}^1 & D_{42}^1 & D_{43}^1 + D_{21}^2 & D_{44}^1 + D_{22}^2 & D_{23}^2 & D_{24}^2 & 0 & 0 \\ 0 & 0 & D_{31}^2 & D_{32}^2 & D_{33}^2 + D_{11}^3 & D_{34}^2 + D_{12}^3 & D_{13}^3 & D_{14}^3 \\ 0 & 0 & D_{41}^2 & D_{42}^2 & D_{43}^2 + D_{21}^3 & D_{44}^2 + D_{22}^3 & D_{23}^3 & D_{24}^3 \\ 0 & 0 & 0 & 0 & D_{31}^3 & D_{32}^3 & D_{33}^3 & D_{34}^3 \\ 0 & 0 & 0 & 0 & D_{41}^3 & D_{42}^3 & D_{43}^3 & D_{44}^3 \end{pmatrix} \begin{pmatrix} c_1 \\ c_2 \\ c_3 \\ c_4 \\ c_5 \\ c_6 \\ c_7 \\ c_8 \end{pmatrix}. \quad \textbf{(B10)}$$

Imposing Boundary Conditions

The boundary conditions for this type of problem require that the wave function $\Psi(x) \rightarrow 0$ as $x \rightarrow \pm\infty$. However computationally we can not handle infinite domains hence we must truncate the domain Ω to some finite but reasonable region (this becomes a source of truncation error). Thus we set the wave function at the end nodes of our truncated region to zero, $\Psi(\pm x_t) = 0$. This is a Dirichlet boundary condition which must be explicitly imposed in our matrix equation. Using the definition of the local Hermite shape functions from Section 2.8 and equation (B4) we can write the wave functions at the end points as,

$$\begin{aligned} \Psi(-x_t) &= c_1 \varphi_1(-x_t) = c_1 = 0 \\ \Psi(+x_t) &= c_7 \varphi_3(+x_t) = c_7 = 0 \end{aligned} \qquad \textbf{(B11)}$$

for our three element problem. We force this condition by altering the columns and rows of the **A** and **D** matrices so as not to include any contribution from the local shape functions $\varphi_1^{(1)}(-x_t)$ and $\varphi_3^{(3)}(+x_t)$. This is done by explicitly setting the 1st and 7th rows and columns of the **A** and **D** matrices to zero. Computationally it is inconvenient to reduce the order of a matrix once its dimension has been defined so we are force to set the diagonal elements of the **A** and **D** matrices to some non-zero value. Thus we set the diagonal elements of **A** to some arbitrary large number (say 10^9) while the related diagonal elements of **B** are set to one. This enables us to keep the same matrix dimensioning. Numerically this will cause two unrealistically large eigenvalues which are easily identified and omitted from the final solution. The value of the wave function at the two nodal points will be some small number (10^{-9} if we had chosen 10^9 to populate the corresponding elements of the **A** matrix). The final matrix equation to solve is,

$$\begin{pmatrix} 10^9 & 0 & 0 & 0 & 0 & 0 & 0 & 0 \\ 0 & A^1_{22} & A^1_{23} & A^1_{24} & 0 & 0 & 0 & 0 \\ 0 & A^1_{32} & A^1_{33}+A^2_{11} & A^1_{34}+A^2_{12} & A^2_{13} & A^2_{14} & 0 & 0 \\ 0 & A^1_{42} & A^1_{43}+A^2_{21} & A^1_{44}+A^2_{22} & A^2_{23} & A^2_{24} & 0 & 0 \\ 0 & 0 & A^2_{31} & A^2_{32} & A^2_{33}+A^3_{11} & A^2_{34}+A^3_{12} & 0 & A^3_{14} \\ 0 & 0 & A^2_{41} & A^2_{42} & A^2_{43}+A^3_{21} & A^2_{44}+A^3_{22} & 0 & A^3_{24} \\ 0 & 0 & 0 & 0 & 0 & 0 & 10^9 & A^3_{34} \\ 0 & 0 & 0 & 0 & A^3_{41} & A^3_{42} & 0 & A^3_{44} \end{pmatrix} \begin{pmatrix} c_1 \\ c_2 \\ c_3 \\ c_4 \\ c_5 \\ c_6 \\ c_7 \\ c_8 \end{pmatrix} = E \begin{pmatrix} 1 & 0 & 0 & 0 & 0 & 0 & 0 & 0 \\ 0 & D^1_{22} & D^1_{23} & D^1_{24} & 0 & 0 & 0 & 0 \\ 0 & D^1_{32} & D^1_{33}+D^2_{11} & D^1_{34}+D^2_{12} & D^2_{13} & D^2_{14} & 0 & 0 \\ 0 & D^1_{42} & D^1_{43}+D^2_{21} & D^1_{44}+D^2_{22} & D^2_{23} & D^2_{24} & 0 & 0 \\ 0 & 0 & D^2_{31} & D^2_{32} & D^2_{33}+D^3_{11} & D^2_{34}+D^3_{12} & 0 & D^3_{14} \\ 0 & 0 & D^2_{41} & D^2_{42} & D^2_{43}+D^3_{21} & D^2_{44}+D^3_{22} & 0 & D^3_{24} \\ 0 & 0 & 0 & 0 & 0 & 0 & 1 & D^3_{34} \\ 0 & 0 & 0 & 0 & D^3_{41} & D^3_{42} & 0 & D^3_{44} \end{pmatrix} \begin{pmatrix} c_1 \\ c_2 \\ c_3 \\ c_4 \\ c_5 \\ c_6 \\ c_7 \\ c_8 \end{pmatrix} \quad \textbf{(B12)}$$

which we can solve for the eigenvalues E and vector c using the ISML [38] subroutine 'DGVCSP'.

Appendix C

Application of the Mass Derivative Boundary Condition

The mass derivative boundary condition is applied at the local level. The form of the finite element solution, equation (2.10), and the properties of the Hermite shape functions, Section 2.7, allow us to write the first derivative of the wave function at the barrier/well interface as,

$$\frac{d}{dx}\Psi(x_{\text{interface}}) = \psi^{\text{interface}} \frac{d\xi}{dx}\frac{d}{d\xi}\varphi(\pm 1) = \psi^{\text{interface}} \tag{C1}$$

where only the constant coefficient remains. Thus continuity of the mass derivative requires that those local constant coefficients corresponding to the derivative terms be continuous,

$$\frac{1}{m_1^*}\overline{\psi}_1^{\text{interface}} = \frac{1}{m_2^*}\overline{\psi}_2^{\text{interface}} \tag{C2}$$

(the bar over top representing those coefficients which correspond to derivative shape functions). Also recall that at the local level the derivative information is contained in the stiffness matrix which is constructed from the equation,

$$\mathcal{K}_{\ell,k}^{(n)} = \int_{-1}^{+1} \frac{1}{m^{*(n)}(\xi)}\left(\frac{d}{d\xi}\varphi_\ell(\xi)\frac{d\xi}{dx}\right)\left(\frac{d}{d\xi}\varphi_k(\xi)\frac{d\xi}{dx}\right)\left|J^{(n)}d\xi\right|. \tag{C3}$$

Thus a natural way of applying the continuity of the mass derivative is to change those elements of the local stiffness matrix that are evaluated with the derivative shape functions for one of the elements on the barrier well interface. For example if we choose to change the local stiffness matrix for an element in the well region which is on the left interface we must multiply the second row and column by the factor $\frac{m_2^*}{m_1^*}$. Likewise for an element in the well region which is on the right interface we must multiply the sixth row and column (assuming quintic Hermite polynomials) by the factor $\frac{m_2^*}{m_1^*}$.

Appendix D

Sample Analytical Problems used to test the Finite Element Algorithm

This section covers initial work to develop a finite element method to solve Schrödinger's equation. Here we study the algorithm and verify its performance and accuracy on a simple heterostructure where an analytical solutions are available.

D.1 Square Well Potential

Starting from the Schrödinger Equation in one dimension[11],[40],[42],

$$\frac{-\hbar^2}{2m}\frac{d^2\Psi(x)}{dx^2}+V(x)\Psi(x)=E\,\Psi(x) \tag{D.1}$$

with a square well potential the potential,

$$V(x)=\begin{cases} V_0 & \text{for } x\le \frac{-\ell}{2} \text{ and } \quad x\le \frac{\ell}{2} \\ 0 & \text{for } \frac{-\ell}{2}<x<\frac{\ell}{2} \end{cases} \tag{D.2}$$

where ℓ is the width of the well. The problem we are interested in here is for the case when $E<V_0$, which corresponds to a single electron trapped inside of the potential well. The unique feature for this type of problem is that only certain particle energies are allowed for the trapped electron, that is this is an eigenvalue problem with energy E as the eigenvalue. Equation (D.2) is plotted in Figure D.1.

Equation (D.1) is converted into a reduced form by multiplying through by $\frac{2m}{\hbar^2}$, by defining a dimensionless coordinate as, ξ $x=\ell\xi$ and dimensionless energy variables ε, as $E=V_0\,\varepsilon$ and $v(\xi)$ as, $V(\xi)=V_0\,v(\xi)$. The time-independent Schrödinger equation for the square well potential is written in reduced form as,

$$-\frac{d^2}{d\xi^2}\Psi(\xi)+\frac{2m\ell^2 V_0}{\hbar^2}\left(v(\xi)-\varepsilon\right)\Psi(\xi)=0. \qquad \textbf{(D.3)}$$

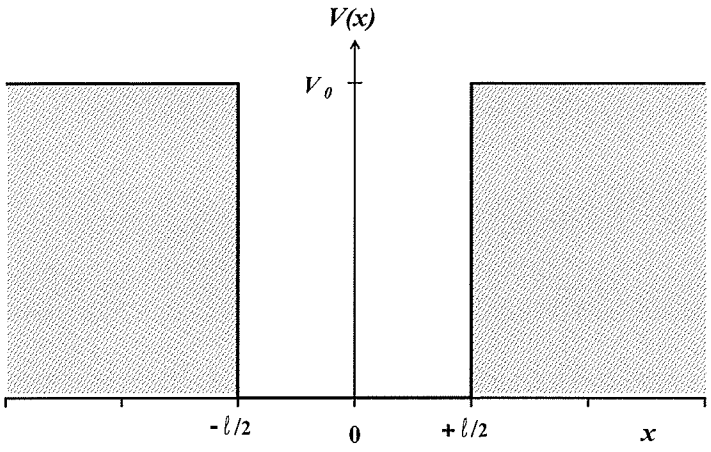

Figure D.1: Square well potential for electron energies E < V_0.

Equation (D.3) is easily converted into a variational form by multiplying through by test functions $\varphi_n(\xi)$ and integrating over the problem domain Ω.

$$\int_\Omega\left[-\varphi_n(\xi)\frac{d^2}{d\xi^2}\Psi(\xi)+\frac{2m\ell^2 V_0}{\hbar^2}\left(v(\xi)-\varepsilon\right)\varphi_n(\xi)\Psi(\xi)\right]d\xi=0. \qquad \textbf{(D.4)}$$

To solve this problem we also need to choose a domain for the problem [45]. Inside the barrier region the wave function $\psi(x)\to 0$ as $x\to\pm\infty$. Computationally we can not handle infinite domains and are forced to choose some suitably truncated region $x\in\Omega=(-x_{trun.}, x_{trun.})$ where we force the wave function to be zero at the 'ends', $\psi(\pm x_{trun.})=0$ [1],[39]. Details on how Equation (D.4) is implemented into the finite element algorithm are found in Appendix B.

We use our finite element algorithm to determine the energy eigenvalues and wave functions (eigenfunctions) for the square well with $m=0.067\,m_0$,

$V_0 = 0.34\,[\mathbf{eV}]$, and $\ell = 100\left[\mathring{\mathrm{A}}\right]$ (m_0 is the electron rest mass). We examine the effect of the size of the truncation region and the number of elements on the accuracy of the finite element solution. In all cases the solutions were approximated using quintic Hermite Polynomials from Section 3.8.

Boundary Conditions:

Boundary conditions for this problem are the continuity of the wave function and its first derivative across the boundaries, that is,

$$\begin{aligned} \Psi^{(A)}(\pm\tfrac{\ell}{2}) &= \Psi^{(B)}(\pm\tfrac{\ell}{2}), \\ \left.\frac{d\Psi^{(A)}(\xi)}{d\xi}\right|_{\pm\frac{\ell}{2}} &= \left.\frac{d\Psi^{(B)}(\xi)}{d\xi}\right|_{\pm\frac{\ell}{2}}. \end{aligned} \tag{D.5}$$

In this problem we are assuming that the electron effective mass has the same value throughout all regions, that is the barrier and well regions. These boundary conditions are satisfied naturally with our choice of shape functions, the quintic Hermit Polynomials.

Exact Solution:

The exact solutions for the square well problem are given by Eisberg [40] and Brehm [42]. When the square well is located symmetrically about the origin the solutions are in terms of even and odd functions commonly referred to as 1st and 2nd class solutions. The energy eigenvalues are given by the following transendental equations for 1st and 2nd class solutions respectively,

$$\begin{aligned} \mathscr{E}\,\tan(\mathscr{E}) &= \sqrt{\frac{mV_0\ell^2}{2\hbar^2} - \mathscr{E}^2}, \\ -\mathscr{E}\,\cot(\mathscr{E}) &= \sqrt{\frac{mV_0\ell^2}{2\hbar^2} - \mathscr{E}^2}, \end{aligned} \tag{D.6}$$

where we have defined $\mathscr{E} = \sqrt{\frac{m E \ell^2}{2\hbar^2}}$. The energy eigenvalues E are those values where these two equations are satisfied and are typically found using a 'root' finding algorithm. We used Brent's algorithm [44] to find the energy eigenvalues within a tolerance of 10^{-10}. The corresponding wave functions for 1st class solutions are given by,

$$\Psi(x) = \begin{cases} \left[A\cos(k_1 \frac{\lambda}{2})\exp(k_2 \frac{\lambda}{2})\right]\exp(k_2 x) & x < -\frac{\lambda}{2} \\ A\cos(k_1 x) & -\frac{\lambda}{2} < x < \frac{\lambda}{2} \\ \left[A\cos(k_1 \frac{\lambda}{2})\exp(k_2 \frac{\lambda}{2})\right]\exp(-k_2 x) & x > \frac{\lambda}{2} \end{cases} \quad \textbf{(D.7)}$$

and 2nd class solutions by,

$$\Psi(x) = \begin{cases} \left[-B\sin(k_1 \frac{\lambda}{2})\exp(k_2 \frac{\lambda}{2})\right]\exp(k_2 x) & x < -\frac{\lambda}{2} \\ B\sin(k_1 x) & -\frac{\lambda}{2} < x < \frac{\lambda}{2} \\ \left[B\sin(k_1 \frac{\lambda}{2})\exp(k_2 \frac{\lambda}{2})\right]\exp(-k_2 x) & x > \frac{\lambda}{2} \end{cases} \quad \textbf{(D.8)}$$

where $k_1 = \sqrt{\frac{2mE}{\eta^2}}$ and $k_2 = \sqrt{\frac{2m}{\eta^2}(V_0 - E)}$. A and B are normalization constants.

Results:

Based on the parameters listed above we find that our square well problem contains three bound states. Figure D.2 and Figure D.3 are plots of the wave functions and the first derivative of the wave functions for each of these eigenstates using 24 equally spaced elements. Figure D.3 illustrates the continuous nature of the first derivative across the well-barrier boundary. This is one of the boundary conditions for this type of problem and is equivalent to saying that the probability current across the well boundary is conserved.

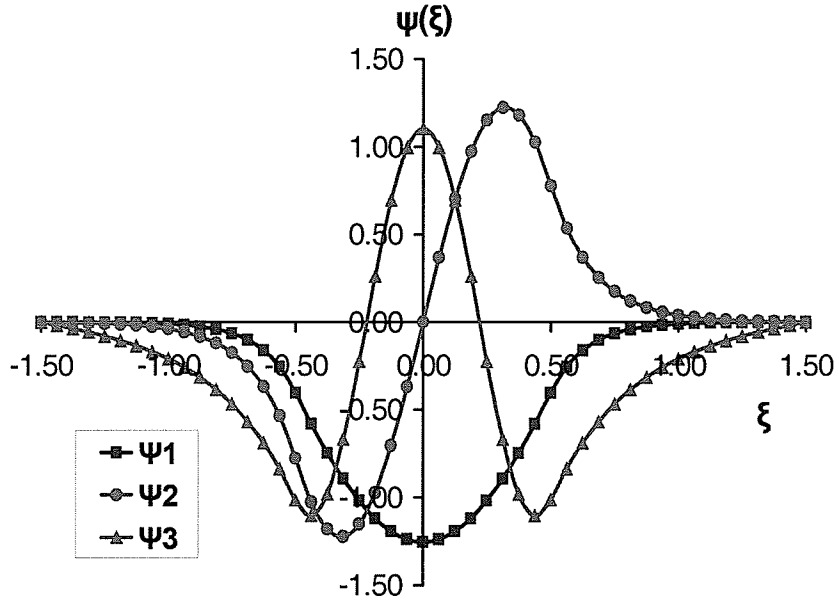

Figure D.2: The wave functions (eigenfunctions) for the square well. Solved using 24 equally spaced elements and $\Omega = (-1.5, 1.5)$.

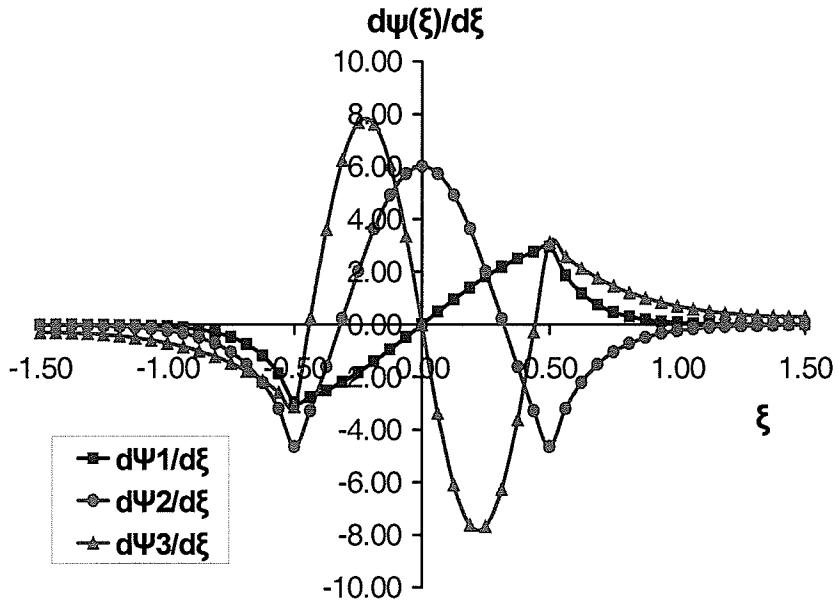

Figure D.3: First derivative of the wave functions for our square well. Solved using 24 equally spaced elements and $\Omega = (-1.5, 1.5)$.

Size of the Domain:

The effect of the size of the domain on the finite element solution was examined. For illustrative purposes we found the finite element solution using equally spaced elements and compare the results for two different sized truncation regions, $\Omega = (-1, 1)$ and $\Omega = (-3, 3)$. For this comparison we kept the same step or element size of $h = \Delta\xi = 0.1$. This means that for the larger domain the number of elements used in the finite element calculation increased.

Table D.1 and Table D.2 compare the exact analytical and calculated energy eigenvalues for the two different domains. From these tables it can be seen that the choice of the domain has an effect on the accuracy of the finite element solution. The accuracy is improved for the case where we used a larger domain. Figure D.4 and Figure D.5 compare the wave functions for these two different choices of domain for the $n = 1$ and $n = 3$ energy eigenstates respectively for the square well described above.

Table D.1: Comparison of the exact and calculated energy eigenvalues for $\xi \in \Omega = (-1, 1)$. This corresponds to 20 equally spaced elements.

State n	E_n (Exact)	E_n (F.E.M.)	% Difference between exact and calculated
1	0.1034272003	0.103480	-0.05087
2	0.4028661847	0.403481	-0.15269
3	0.8427820206	0.853689	-1.29412

Table D.2: Comparison of the exact and calculated energy eigenvalues for $\xi \in \Omega = (-3, 3)$. This corresponds to 60 equally spaced elements.

State n	E_n (Exact)	E_n (F.E.M.)	% Difference between exact and calculated
1	0.1034272003	0.103427	0.0000037
2	0.4028661847	0.402866	-0.0000002
3	0.8427820205	0.842782	-0.0000074

These plots illustrate the reason for the improvement in accuracy as we increase the size of the domain. It can be seen that as the eigenstate increases the energy eigenvalue increases. Figure D.5 illustrates that for the lowest eigenstate the particle and hence the wave function are limited to the well region, thus the smaller domain is sufficient for calculating the particle energy and wave function. On the other hand Figure D.5 illustrates that as the eigenstate increases, the corresponding increase in particle energy also corresponds to an increased probability of the particle and hence the wave function tunnelling into the barrier regions. We can see that choosing a domain which is too small artificially forces the wave function to zero thus producing an eigenvalue which is greater than the actual value. Thus to accurately approximate the wave function in the barrier region it is important to choose a domain which is large enough to reasonably contain all wave functions.

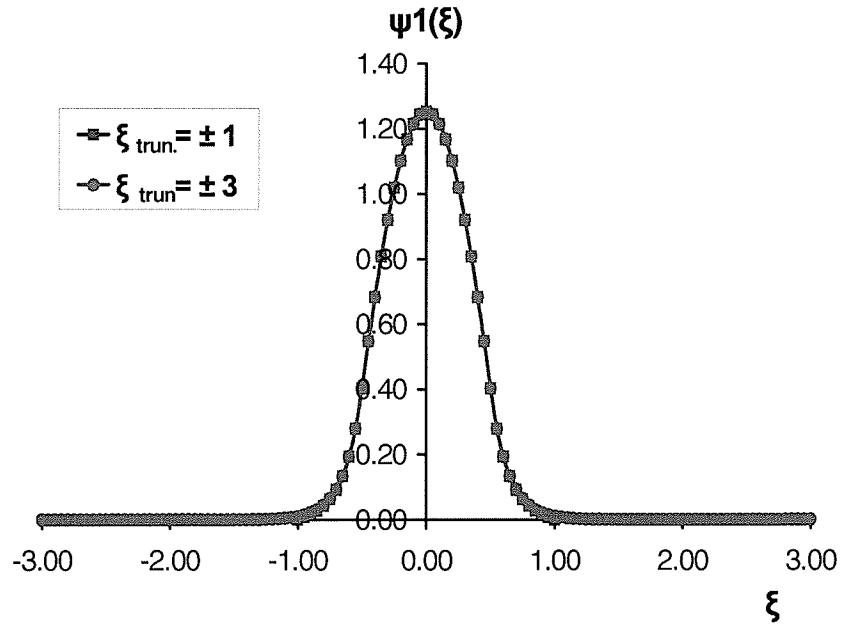

Figure D.4: Comparison of the wave function for different sized domains for the 1st eigenstate of our one dimensional square well. Here we find excellent agreement.

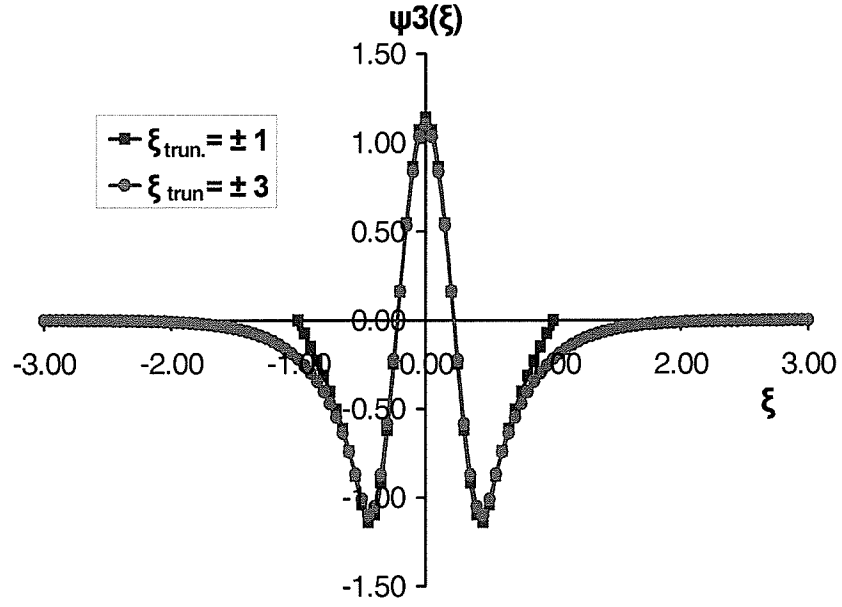

Figure D.5: Comparison of the wave function for different sized domains for the 3rd eigenstate of our one dimension square well. Here we see that truncating the region too small artificially forces the wave function to zero too soon.

Number of Elements:

The effect of the number of elements on the finite element solution was examined. We calculate the finite element solution using 3, 15, and 24 elements in the domain $\Omega = (-1.5, 1.5)$. The element length was kept constant for each scenario. This means that as the number of elements increases the element length decreases.

Table D.3, D.4, and D.5 are comparisons between the exact analytical and the finite element energy eigenvalue for 3, 15, and 24 elements respectively. From these tables it can be seen that as the number of elements increases so to does the accuracy of the finite element solution.

Table D.3: Comparison of the exact and calculated energy eigenvalues for 3 equally spaced elements. Domain $\xi \in \Omega = (-1.5, 1.5)$.

State n	E_n (Exact)	E_n (F.E.M.)	% Difference between exact and calculated
1	0.1034272003	0.103470	-0.04110
2	0.4028661847	0.402905	-0.00974
3	0.8427820206	0.855983	-1.56638

Table D.4: Comparison of the exact and calculated energy eigenvalues for 15 equally spaced elements. Domain $\xi \in \Omega = (-1.5, 1.5)$.

State n	E_n (Exact)	E_n (F.E.M.)	% Difference between exact and calculated
1	0.1034272003	0.103427	-0.00003
2	0.4028661847	0.402868	-0.00039
3	0.8427820206	0.843241	-0.05443

Table D.5: Comparison of the exact and calculated energy eigenvalues for 24 equally spaced elements. Domain $\xi \in \Omega = (-1.5, 1.5)$.

State n	E_n (Exact)	E_n (F.E.M.)	% Difference between exact and calculated
1	0.1034272003	0.103427	-0.00003
2	0.4028661847	0.402868	-0.00039
3	0.8427820206	0.843241	-0.05443

Figure D.6, D.7, and D.8 are plots which compare the difference between the exact and the numerical wave functions using 3, 15, and 24 elements for each of the three states. From these plots we can see that as the number of elements increases so to does the accuracy of the finite element solution (note that in Figures D.6 and D.8 the difference curve for 3 elements had to be scaled in order to be included on the plot). These plots also illustrate a difference between the even and odd functions. The plots suggest that more elements are required in the well region to approximate the odd functions while more elements are required in the barrier region to approximate the even functions.

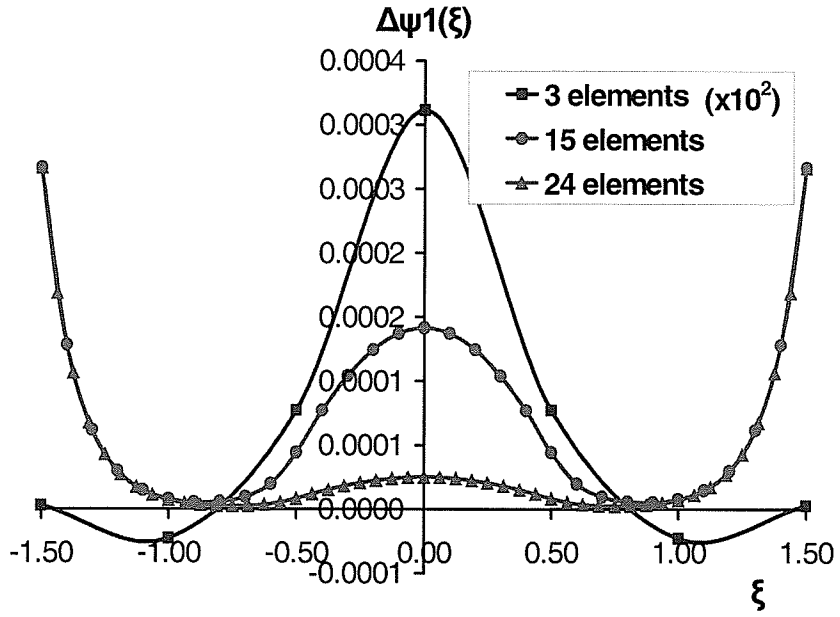

Figure D.6: Plot of the difference between the exact and calculated wave functions for the 1st state calculated with different numbers of elements.

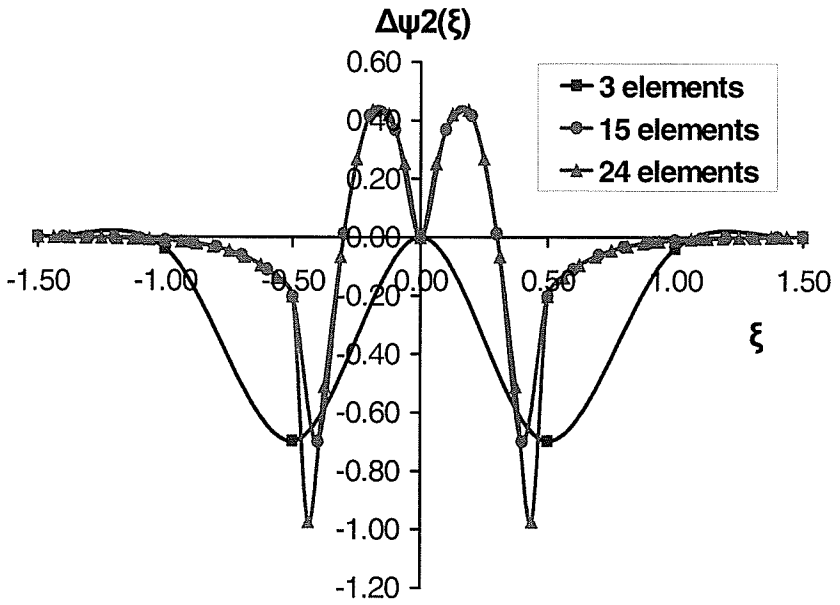

Figure D.7: Plot of the difference between the exact and calculated wave function for the 2nd state calculated with different numbers of elements.

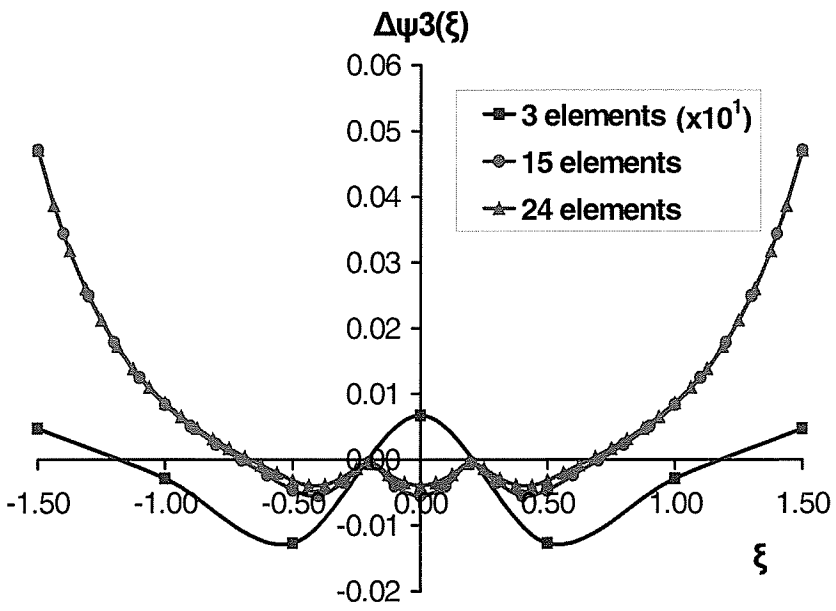

Figure D.8: Plot of the difference between the exact and calculated wave function for the 3rd state calculated with different numbers of elements.

Another option to increase the accuracy of the finite element solution is to vary the size of the elements. In this case the element size is chosen such that the function we are solving for is varying slowly within each element. This means we use more elements for regions where the function is oscillatory and less where it is not oscillatory. We did not examine this possibility.

D.2 Semiconductor Quantum Well Device

The semiconductor quantum well is a layered AlGaAs/GaAs/AlGaAs semiconductor structure constructed by varying the aluminum concentration in the semiconductor substrate. For this type of structure the effective mass of the electron or the hole will depend on its position in the structure. Otherwise this is the square well problem again. In the effective mass approximation the 1-D Schrödinger equation for the semiconductor quantum well is given by,

$$\frac{-\hbar^2}{2}\frac{d}{dx}\frac{1}{m(x)}\frac{d\Psi(x)}{dx}+V(x)\Psi(x)=E\,\Psi(x). \qquad \textbf{(D.9)}$$

The potential is given by,

$$V(x)=\begin{cases} V_0 & \text{for } x\le\frac{-\ell}{2} \text{ and } \quad x\le\frac{\ell}{2} \\ 0 & \text{for } \frac{-\ell}{2}<x<\frac{\ell}{2} \end{cases} \qquad \textbf{(D.10)}$$

where ℓ is the width of the well and $m(x)$ is the mass which also a function of position. The mass is assumed to change abruptly at the well interfaces,

$$m(x)=\begin{cases} m^*_{barrier}\ m_0 & x<-\frac{\ell}{2} \\ m^*_{well}\ m_0 & -\frac{\ell}{2}<x<-\frac{\ell}{2} \\ m^*_{barrier}\ m_0 & x>\frac{\ell}{2} \end{cases} \qquad \textbf{(D.11)}$$

where m_0 is the electron rest mass and $m^*_{barrier}$ and m^*_{well} are the effective mass of the hole or electron in the barrier or well region respectively. Again we are interested in bound states which is the case when $E<V_0$.

Equation (D.9) is converted into a reduced form as before with the position dependent effective mass remaining with the derivative term,

$$-\frac{d}{d\xi}\frac{1}{m^*(\xi)}\frac{d}{d\xi}\Psi(\xi)+\frac{2m_0\ell^2V_0}{\hbar^2}\big(v(\xi)-\varepsilon\big)\Psi(\xi)=0. \qquad \textbf{(D.12)}$$

This is easily converted into a variational using techniques discussed before,

$$\int_{\Omega} \frac{1}{m^*(\xi)} \frac{d}{d\xi} \varphi_n(\xi) \frac{d}{d\xi} \Psi(\xi)\, d\xi - \varphi_n(\xi) \frac{1}{m^*(\xi)} \frac{d}{d\xi} \Psi(\xi) \Big|_a^b$$
$$+ \frac{2m_0 \ell^2 V_0}{\hbar^2} \int_{\Omega} \varphi_n(\xi) v(\xi) \Psi(\xi)\, d\xi \qquad \textbf{(D.13)}$$
$$= \frac{2m_0 \ell^2 V_0}{\hbar^2} \varepsilon \int_{\Omega} \varphi_n(\xi) \Psi(\xi)\, d\xi.$$

In matrix form we define,

$$\mathbf{A} = \int_{\Omega} \left[\frac{1}{m^*(\xi)} \frac{d}{d\xi} \varphi_n(\xi) \frac{d}{d\xi} \Psi(\xi) + \frac{2m_0 \ell^2 V_0}{\hbar^2} \varphi_n(\xi) v(\xi) \Psi(\xi) \right] d\xi$$
$$- \varphi_n(\xi) \frac{1}{m^*(\xi)} \frac{d}{d\xi} \Psi(\xi) \Big|_a^b, \qquad \textbf{(D.14)}$$
$$\mathbf{D} = \frac{2m_0 \ell^2 V_0}{\hbar^2} \varepsilon \int_{\Omega} \varphi_n(\xi) \Psi(\xi)\, d\xi.$$

Boundary Conditions.

The most important difference between the quantum mechanical square well problem of Section D.1 and the semiconductor quantum square well are the implementation of boundary conditions across layer interfaces. The boundary conditions are that the wave function and its first derivative (probability current) be continuous across the well/barrier interface. When considering the boundary condition of first derivative at the interface however, there is a subtlety we must consider. The boundary condition for the first derivative is derived from considering the conservation of probability current across the interface. For the time independent Schrödinger equation the probability current is given by,

$$j(x) = \frac{\eta}{2m\, i} \left(\Psi^*(x) \frac{\partial \Psi(x)}{\partial x} - \frac{\partial \Psi^*(x)}{\partial x} \Psi(x) \right) \qquad \textbf{(D.15)}$$

where the * represents the complex conjugate. If we let Ψ_1 be the wave function in the barrier region and Ψ_2 be the wave function in the well region, then at the interface the conservation of probability current requires,

$$\frac{\hbar}{2m_1 i}\left(\Psi_1^* \frac{d\Psi_1}{dx} - \frac{d\Psi_1^*}{dx}\Psi_1\right) = \frac{\hbar}{2m_2 i}\left(\Psi_2^* \frac{d\Psi_2}{dx} - \frac{d\Psi_2^*}{dx}\Psi_2\right). \qquad \textbf{(D.16)}$$

Using the first condition that the wave function must be continuous across the boundary, $\Psi_1 = \Psi_2$ we can write,

$$\Psi^*\left(\frac{1}{m_1}\frac{d\Psi_1}{dx} - \frac{1}{m_2}\frac{d\Psi_2}{dx}\right) + \Psi\left(\frac{1}{m_2}\frac{d\Psi_2^*}{dx} - \frac{1}{m_1}\frac{d\Psi_1^*}{dx}\right) = 0. \qquad \textbf{(D.17)}$$

Thus we find that the first derivative boundary condition is given by,

$$\frac{1}{m_1}\frac{d\Psi_1}{dx} = \frac{1}{m_2}\frac{d\Psi_2}{dx}, \qquad \textbf{(D.18)}$$

which we call a boundary condition on the mass derivative at the well/barrier interface. The application of this boundary condition is illustrated in Appendix C.

Results

We use our finite element algorithm to determine the energy eigenvalues for the semiconductor quantum well with the parameters specified in Nakamura et. al. [39]; $m^*_{barrier} = 0.0919$, $m^*_{well} = 0.067$, $V_0 = 0.225\left[\mathbf{eV}\right]$, and $\lambda = 200\left[\mathring{\mathbf{A}}\right]$. We choose the domain for the problem to be the truncated region, $\xi \in \Omega = (-3, 3)$ and force the wave function to be zero at the 'ends', $\Psi(\pm 3) = 0$. Quintic Hermit Polynomials were used as the shape functions. The energy eigenvalues which were determined by our finite element algorithm are

given in Table D.6 and compared with the exact results [39]. We find excellent agreement between our calculated result and the exact value given in Nakaura [39].

Table D.6: Comparison of the exact and calculate eigenvalue calculation.

State n	E_n [39] (Exact)	E_n (F.E.M.)	Percent Difference (%)
1	0.04429856044	0.0442917	0.01560
2	0.1767635987	0.176736	0.01553
3	0.3952601369	0.395200	0.01532
4	0.6915909027	0.691490	0.01462

Figure D.9 is a plot of the wave function and its first derivative for the first eigenvalue. This figure illustrates a unique feature of this problem. It can be seen that the wave function is smooth and continuous across the barrier/well interface. However the first derivative of the wave function while continuous, is not smooth at the interface. It is the abrupt change in the effective mass of the electron at the interface which causes this characteristic. To improve the accuracy for problems of this type it is necessary to increase the number of elements at the interface.

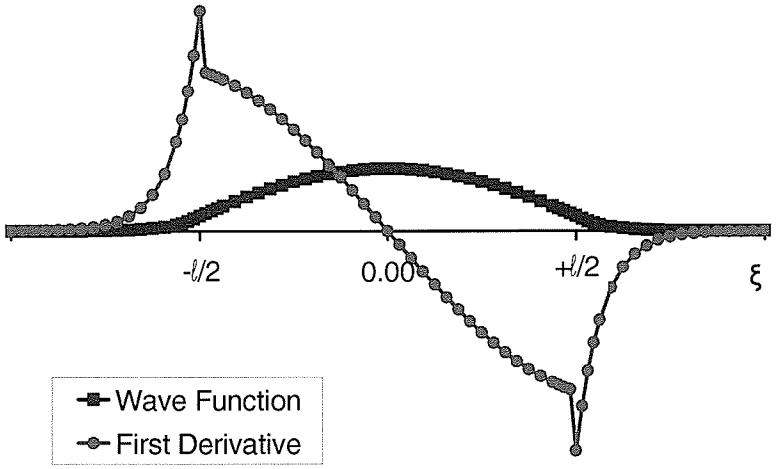

Figure D.9: Plot of the wave function and its first derivative for the 1st eigenstate for the semiconductor quantum well.

D.3 Square Potential Barrier

For quantum mechanical tunnelling problems we solve the one dimensional Schrödinger Equation,

$$\frac{-\eta^2}{2m}\frac{d^2\Psi(x)}{dx^2}+V(x)\Psi(x)=E\Psi(x) \tag{D.19}$$

with the square potential barrier,

$$V(x)=\begin{cases}0 & x\le d_1\\ V_0 & d_1\le x\le d_2.\\ 0 & x\ge d_2\end{cases} \tag{D.20}$$

The potential barrier is illustrated in Figure (D.10).

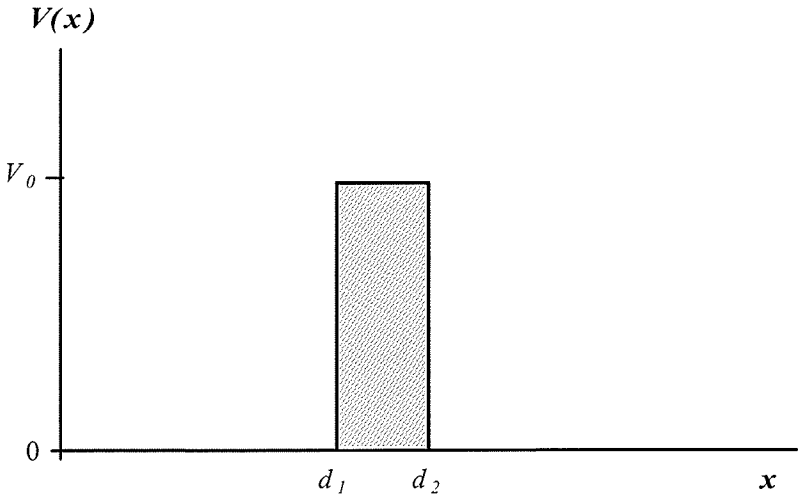

Figure D.10: Square potential barrier. The blue shading indicating the classically forbidden region when $E < V_0$.

The solution to the tunnelling problem involves solving for the particle wave functions inside of the barrier region for some energy E. To simplify the form of the wave functions and the application of related boundary conditions the domain is restricted to include only the positive x-axis, and we assume that the particle is incident from the left hand side of the barrier. The typical quantities of interest for barrier problems are the transmission and reflection coefficients which tell us the percent of the incident wave which is transmitted or reflected by the barrier. These quantities will be developed below. At the barrier interface we require the continuity of the wave function and its first derivative. These boundary conditions are written as,

$$\begin{aligned} \Psi_I(d_1) &= \Psi_{II}(d_1), \\ \Psi_{II}(d_2) &= \Psi_{III}(d_2), \\ \frac{d}{dx}\Psi_I(x)\Big|_{d_1} &= \frac{d}{dx}\Psi_{II}(x)\Big|_{d_1}, \\ \frac{d}{dx}\Psi_{II}(x)\Big|_{d_2} &= \frac{d}{dx}\Psi_{III}(x)\Big|_{d_2}. \end{aligned} \tag{D.21}$$

If we let,

$$\begin{aligned} k_1 = k_3 &= \sqrt{\frac{2mE}{\hbar^2}} \\ k_2 &= \sqrt{\frac{2m}{\hbar^2}(V(x)-E)} \end{aligned} \tag{D.22}$$

we can write the solution for the particle in each region in terms of travelling waves. For the geometry given in Figure D.10 the travelling wave solutions are given by [13],[40],[42],[41]:

Region I: $(x \leq d_1)$

To the left of the barrier,

$$\Psi_I(x) = A e^{ik_1 x} + r e^{-ik_1 x}. \qquad \textbf{(D.23)}$$

It can be seen from this solution that the particle wave function in this region is composed of two components. The first component, $A e^{ik_1 x}$, represents the incident wave for a free particle which is travelling in positive x direction. The coefficient or amplitude A is known. The second component, $r e^{-ik_1 x}$, represents a wave which is reflected by the barrier for a free particle travelling in the negative x direction. The coefficient r is an unknown to be determined.

Region II: $(d_1 \leq x \leq d_2)$

Inside the barrier,

$$\Psi_{II}(x) = C e^{k_2 x} + D e^{-k_2 x}. \qquad \textbf{(D.24)}$$

The wave function in this region is again composed of two components. The first component, $C e^{k_2 x}$, is an exponentially decreasing wave for a particle travelling in the negative x direction. The second component, $D e^{-k_2 x}$, is an exponentially decreasing wave for a particle travelling in the positive x direction. Both constant coefficients C and D are unknowns.

Region III: $(x \geq d_2)$

To the right of the barrier,

$$\Psi_{III}(x) = t\, e^{ik_3 x}. \tag{D.25}$$

In this region the particle wave function is composed of only one component. This is called the transmitted wave function and it represents a particle travelling in the positive x direction. The constant coefficient t is unknown and to be determined.

Transmission and Reflection Coefficients.

The transmission and reflection coefficients are derived from the continuity of the probability current across the barrier interface [1],[40],[42]. The probability current is given by,

$$j(x) = \tfrac{\hbar}{2mi}\left(\psi^*(x)\tfrac{d}{dx}\psi(x) - \left(\tfrac{d}{dx}\psi^*(x)\right)\psi(x)\right). \tag{D.26}$$

The incident probability current is found by substituting the incident wave function, $Ae^{ik_1 x}$ into Equation (D.26),

$$j_{inc.}(x) = \frac{k_1\hbar}{m}|A|^2. \tag{D.27}$$

Likewise we can find the transmitted and reflected probability current densities,

$$\begin{aligned} j_{trans.}(x) &= \frac{k_3\hbar}{m}|t|^2, \\ j_{refl.}(x) &= \frac{k_1\hbar}{m}|r|^2. \end{aligned} \tag{D.28}$$

The transmission and reflection coefficients are defined as,

$$T = \frac{j_{trans.}}{j_{inc.}} = \frac{k_3 |t|^2}{k_1 |A|^2}$$
$$R = \frac{j_{refl.}}{j_{inc.}} = \frac{|r|^2}{|A|^2} \qquad \textbf{(D.29)}$$

respectively. The coefficients satisfy the following property,

$$T = 1 - R. \qquad \textbf{(D.30)}$$

Finite Element Implementation.

Refer to Appendix A for details on the matrix formulation.

In tunnelling problems it is often more convenient to find a solution in terms of the travelling wave functions given in Equations (D.23), (D.24) and, (D.25). This will allow us to directly solve for the coefficients *t* and *r*. From the boundary conditions in Equation (D.23) we can write,

$$\Psi(d_1) = \sum_n \psi_n \, \varphi_n(d_1) = \psi_1 = A\, e^{ik_1 d_1} + r\, e^{-ik_1 d_1}$$
$$\tfrac{d}{dx}\Psi(x)\big|_{d_1} = \sum_n \psi_n \, \tfrac{d}{dx}\varphi_n(x)\big|_{d_1} = \psi_2 = ik_1 A\, e^{ik_1 d_1} - ik_1 r\, e^{-ik_1 d_1} \qquad \textbf{(D.31)}$$

and,

$$\Psi(d_2) = \sum_n \psi_n \, \varphi_n(d_2) = \psi_{N-1} = t\, e^{ik_3 d_2}$$
$$\tfrac{d}{dx}\Psi(x)\big|_{d_2} = \sum_n \psi_n \, \tfrac{d}{dx}\varphi_n(x)\big|_{d_2} = \psi_N = ik_3\, t\, e^{ik_3 d_2} \qquad \textbf{(D.32)}$$

where *N* is the total number of global shape functions used to approximate the solution. These equations can be written in a matrix form as,

$$\begin{pmatrix} \psi_1 \\ \psi_2 \end{pmatrix} = \begin{pmatrix} e^{ik_1 d_1} & e^{-ik_1 d_1} \\ ik_1 e^{ik_1 d_1} & -ik_1 e^{-ik_1 d_1} \end{pmatrix} \begin{pmatrix} A \\ r \end{pmatrix} \qquad \textbf{(D.33)}$$

and,

$$\begin{pmatrix} \psi_{N-1} \\ \psi_N \end{pmatrix} = \begin{pmatrix} e^{ik_3 d_2} & 0 \\ ik_3 e^{ik_3 d_2} & 0 \end{pmatrix} \begin{pmatrix} t \\ 0 \end{pmatrix}. \tag{D.34}$$

Which is written into a general global transformation matrix,

$$\begin{pmatrix} \psi_1 \\ \psi_2 \\ \vdots \\ \psi_{N-1} \\ \psi_N \end{pmatrix} = \begin{pmatrix} e^{ik_1 d_1} & e^{-ik_1 d_1} & \cdots & 0 & 0 \\ ik_1 e^{ik_1 d_1} & -ik_1 e^{-ik_1 d_1} & \cdots & 0 & 0 \\ \vdots & \vdots & \ddots & \vdots & \vdots \\ 0 & 0 & \cdots & e^{ik_3 d_2} & 0 \\ 0 & 0 & \cdots & ik_3 e^{ik_3 d_2} & 1 \end{pmatrix} \begin{pmatrix} A \\ r \\ \vdots \\ t \\ 0 \end{pmatrix}. \tag{D.35}$$

We define the transformation matrix as,

$$T = \begin{pmatrix} e^{ik_1 d_1} & e^{-ik_1 d_1} & \cdots & 0 & 0 \\ ik_1 e^{ik_1 d_1} & -ik_1 e^{-ik_1 d_1} & \cdots & 0 & 0 \\ \vdots & \vdots & \ddots & \vdots & \vdots \\ 0 & 0 & \cdots & e^{ik_3 d_2} & 0 \\ 0 & 0 & \cdots & ik_3 e^{ik_3 d_2} & 1 \end{pmatrix}. \tag{D.36}$$

The interior diagonal elements in the global transformation matrix are equal to 1. Substituting this into the original matrix equation we arrive at the following matrix equation to solve, $A\,T\,\sigma = b$. Here b is the vector containing the boundary condition information and σ is the unknown vector we wish to solve for and contains the coefficients A, r, and t.

Results:

We use our finite element algorithm to calculate the transmission coefficient for the square well barrier with potential $V_0 = 0.35 \ [\text{eV}]$ and width $\lambda = 30 \ [\text{Å}]$. We increment the particle energy E over the range $0.02\,V_0 \le E \le 5.5\,V_0$. An exact expression for the transmission coefficient is given in Eisberg and Resnick [40],

$$T = \begin{cases} \left[1 + \dfrac{\frac{1}{4}V_0^2 \sinh^2(k_2 \ell)}{E|V_0 - E|}\right]^{-1} & \text{for } E < V_0 \\ \left[1 + \dfrac{\frac{1}{4}V_0^2 \sin^2(k_2 \ell)}{E|V_0 - E|}\right]^{-1} & \text{for } E > V_0 \end{cases} . \qquad \textbf{(D.37)}$$

Figure D.11 is a plot of the comparison of the transmission coefficient for 2, 4, and 10 elements. We find the finite element solution converges quickly to the exact solution as the number of elements increases. In Figure D.12 we plot the difference between the exact and FEM solutions.

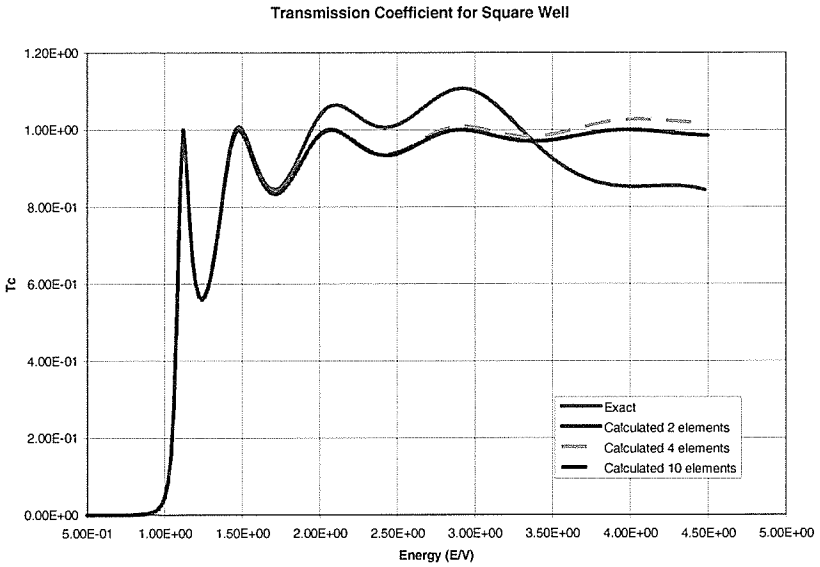

Figure D.11: The transmission coefficient for a square potential barrier.

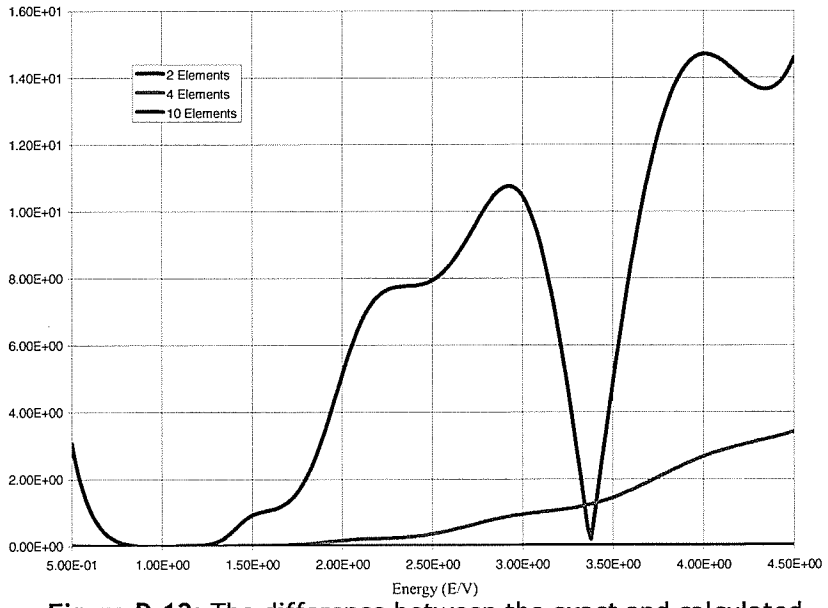

Figure D.12: The difference between the exact and calculated transmission coefficient for 2, 4, and 10 elements.

D.4 Smooth Potential Barrier

Next we will examine the concepts necessary to solve tunnelling problems for an arbitrary potential barrier[46],[47] which changes continuously with position. Consider a potential barrier given by,

$$V(x) = \frac{V_0}{\cosh^2\left(\alpha(x-d)\right)} \tag{D.38}$$

where α is a scaling factor required to convert the coordinate x into dimensionless form. Notice that d is used to shift the potential so that the solution domain lies entirely within the positive x-axis, thus we can use the finite element formulation developed in the previous section.

For this problem we again must specify the energy E of the incident particle and solve for the wave function inside of the barrier region. We assume that the particle is incident from the left hand side of the barrier. For this problem there is no clearly defined barrier interface. Instead we artificially truncate the domain at some reasonable coordinate, $x \in \Omega = (d_1, d_2)$, beyond which we assume the potential is zero. This truncation point replaces the barrier interface we that we had for the square well potential barrier of Section D.4. Hence the truncation point is treated as if it were a barrier interface giving us the three regions with wave functions given by Equations (D.23), (D.24) and, (D.25). Again we require the continuity of the wave function and its first derivative across the region boundaries. The boundary conditions are the same as Equation (D.21) in the previous section.

The finite element formulation for this type of problem is in exactly the same form as that presented in Section A for the square potential barrier. We simply replace the square well potential Equation (D.20) with the smooth potential of Equation (D.38) with the wave vectors,

$$k_1 = k_3 = \sqrt{\frac{2mE}{\hbar^2}},$$
$$k_2 = \sqrt{\frac{2m}{\hbar^2}(V(x) - E)}. \qquad \textbf{(D.39)}$$

After replacing the potential we solve the set of corresponding matrix equations for the transmission coefficient with the following parameters. The maximum of the potential is set at, $V_0 = 0.35 \ \ [\mathrm{eV}]$, the scaling factor is $\alpha = 8\times10^{10}\ [m]^{-1}$, and the truncated barrier region is set at d_1 = 150 [Å] and d_2 = 180 [Å]. We increment the particle energy E over the range $0.02\,V_0 \le E \le 5.5\,V_0$ and compare the transmission coefficient determined using our finite element algorithm with the exact transmission coefficient. An exact expression for the transmission coefficient is calculated by Landau and Lifshitz [48],

$$T = \frac{\sinh^2(\pi k_1/\alpha)}{\sinh^2(\pi k_1/\alpha) + \cosh^2\left(\frac{1}{2}\pi\sqrt{8mV_0/(\eta^2\alpha^2) - 1}\right)} \qquad \textbf{(D.40)}$$

when $8mV_0/(\eta^2\alpha^2) > 1$ and,

$$T = \frac{\sinh^2(\pi k_1/\alpha)}{\sinh^2(\pi k_1/\alpha) + \cos^2\left(\frac{1}{2}\pi\sqrt{1 - 8mV_0/(\eta^2\alpha^2)}\right)} \qquad \textbf{(D.41)}$$

when $8mV_0/(\eta^2\alpha^2) < 1$.

Figure D.13 is a plot of the transmission coefficient calculated with our finite element algorithm using 2, 4, and 10 elements. Figure D.14 is a plot of the difference between the exact transmission coefficient and that calculated using our finite element algorithm. We find that the finite element solution converges quickly to the exact solution as the number of elements increases.

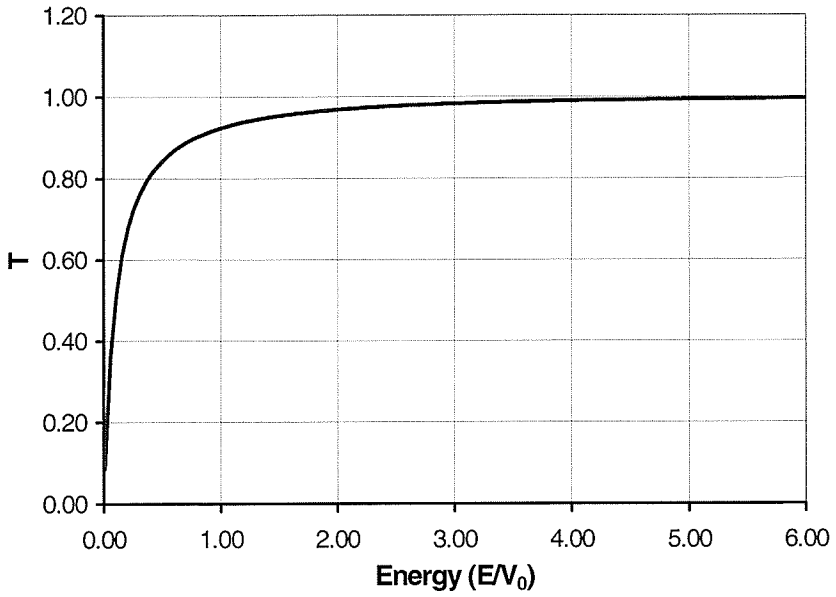

Figure D.13: Transmission Coefficient for hyperbolic potential.

References

[1] Ram-Mohan, L.R. *Finite Element and Boundary Element Applications in Quantum Mechanics*, Oxford University Press, 2002.

[2] Ram-Mohan, L.R., and J.R. Meyer. "Multiband Finite Element Modeling of Wavefunction-Engineered Electro-Optical Devices", *Journal of Nonlinear Optical Physics and Materials*, Volume 4, No. 1, 1995, pg. 191.

[3] Ram-Mohan, L.R., I. Vurgaftman, and J.R. Meyer. "Wave function engineering of antimonide quantum-well lasers", *Microelectronics Journal* 30, 1999, pg. 1031.

[4] Tsuneya, A. "Self-Consistent Results for a GaAs/Al_xGa_{1-x} As Heterojunction. I. Subband Structure and Light-Scattering Spectra", Journal of the Physical Society of Japan, Volume 51, No. 12, 1982, pg. 3893.

[5] Tsuneya, A.; "Self-Consistent Results for a GaAs/Al_xGa_{1-x} As Heterojunction. II. Low Temperature Mobility", Journal of the Physical Society of Japan, Volume 51, No. 12, 1982, pg. 3900.

[6] Shur, M., J.H. Baek, P.P. Ruden, R.R. Daniels, D.E. Grider, T. Nohava, and D. Arch; "Modeling and Simulation of Doped Channel Heterostructure FETs and Integrated Circuits", ISCAS 88, 1988, pg. 409.

[7] Foulger, D.L., P.M. Smowton, P. Blood, and PA. Mawby. "Self-consistent simulation of (AlGa)InP/GaInP visible lasers", IEE Proceedings Optoelectonics, Volume. 144, No. 1, 1997, pg. 23.

[8] Zid, F.B., A. Bhouri, H. Merjri, M. Sais, N. Bouarissa, J.L. Lazzari, F. Arnaud d'Avitaya, and J. Derrien. "Electronic structure calculations for Si/Si1-x Gex multi-quantum well devices", Materials Science & Engineering C 23, 2003, pg. 959.

[9] Bettess, P., R.A. Abram. "Finite and infinite elements for a simple problem in quantum mechanics," *Communications in Numerical Methods in Engineering* 18, 2002, pg. 325.

[10] Shertzer, J., and L.R. Ram-Mohan. "Removal of accidental degeneracies in semiconductor quantum wires," Physical Review B, Volume 41, No. 14, 1990, pg. 9994.

[11] Searles, D.J., E.I. von Nagy-Felsobuki. "Numerical experiments in quantum physics: Finite-element method," *American Journal of Physics* 56, No 5, 1988, pg. 444.

[12] Fanchiotti, S., and M.A. Rubin. "Error estimates, error bounds, and adaptive refinement in finite-element quantum theory," Physical Review D, Volume 43, No. 10, 1991, pg. 3524.

[13] Moussa, J.E. *The Schrödinger-Poisson Selfconsistency in Layered Quantum Semiconductor Structures*, Master of Science Thesis, Worcester Polytechnic Institute, 2003.

[14] Ram-Mohan L.R., K. Yoo and J. Moussa; "The Schrödinger-Poisson self-consistency in layered quantum semiconductor structures", *Journal of Applied Physics*, Volume 95, Number 6, March 2004, pg. 3081.
[15] Stern, F.; "Iteration Methods for Calculating Self-Consistent Fields in Semiconductor Inversion Layers", Journal of Computational Physics, Volume 6, 1970, pg. 56.
[16] Stern, F.; "Self-Consistent Results for n-Type Si Inversion Layers", Physical Review B, Volume 5, No. 12, 1972, pg. 4891.
[17] Bastard, G. *Wave Mechanics Applied to Semiconductor Heterostructures*, Les Editions de Physique, Les Ulis, France, 1988.
[18] Inoue, K., H. Sakaki, J. Yoshino and T Hotta; "Self-consistent calculation of electronic states in AlGaAs/GaAs/AlGaAs selectively doped double-heterojunction systems under electric fields", Journal of Applied Physics, Volume 58, No. 11, 1985, pg. 4277.
[19] Kerkhoven, T., A.T. Galick, U. Ravaioli, J.H. Arends and Y. Saad; "Efficient numerical simulation of electronic states in quantum wires", Journal of Applied Physics, Volume 68, No. 7, 1990, pg. 3461.
[20] Kerkhoven, T., M.W. Raschle and U. Ravaioli; "Self-consistent simulation of quantum wires in perodic heterojunction structures", Journal of Applied Physics, Volume 74, No. 2, 1993, pg. 1199.
[21] Kim, K.T., S.S. Lee and S.L. Chuang; "Inter miniband optical absorption in a modulation-doped AlxGa1-xAs/GaAs superlattice", Journal of Applied Physics, Volume 69, No. 9, 1991, pg. 6617.
[22] Trellakis, A., A.T. Galick, A. Pacelli and U. Ravaioli; "Iteration scheme for the solution of the two-dimensional Schrödinger-Poisson equations in quantum structures", Journal of Applied Physics, Volume 81, No. 12, 1997, pg. 7880.
[23] Wolfe, C.M., N. Holonyak JR., and G.E. Stillman. Physical Properties of Semiconductors, Prentice-Hall, Inc. 1989.
[24] Morgan, D.V., F.H. Eisen, and A. Ezis; "Prospects for ion bombardment and ion implantation in GaAs and Inp device fabrication," IEE Proceedings, Volume 128, No. 4, 1981, pg. 109-130.
[25] Solymar, L. and D. Walsh. "Lectures on the Electrical Properties of Materials", 5th Edition, Oxford University Press, New York, 1993.
[26] Kittel, C. *Introduction to Solid State Physics*, 6th Edition, John Wiely & Sons Inc., New York, 1986.
[27] *Heterostructures and Quantum Devices*, VLSI Electronics: Microstructure Science, W.R. Frensley, and E.G. Einspruch editors. Academic Press, 1994.
[28] Adachi, S. "GaAs, AlAs, and $Al_xGa_{1-x}As$: Material Parameters for use in Research and Device Applications." Journal of Applied Physics, Volume 58, No. 3, 1985, pg. R1.

[29] Humlicek, J., and F. Lukes. "Temperature Dependence of the Direct Energy Gap in a GaAs/AlAs superlattice", Physical Review B, Volume 42, Number 5, 1990, pg. 2932.
[30] Batey, J. and L. Wright. "Energy band alignment in GaAs:(Al,Ga)As heterostructures: The dependency on alloy composition", Journal of Applied Physics, Volume 59, No. 1, 1966, pg. 200.
[31] Vurgaftmann, I., J.R. Meyer, and L.R. Ram-Mohan. "Band parameters for III-V compound semiconductors and their alloys", Journal of Applied Physics, Volume 89, No. 11, 2001, pg. 5815.
[32] Szabo, B. and I. Babuska. "Finite Element Analysis", John WiLey & Sons Inc., New York, 1991.
[33] Guo, B. Course notes for 136.811 Applied Finite Element Analysis, University of Manitoba, 2002.
[34] DeVries, P.L. "A First Course in Computational Physics", John WiLey & Sons Inc., New York, 1994.
[35] Zienkiewicz, O.C. and R.L. Taylor. "The Finite Element Method, Volume 1, The Basis", 5th Edition, Butterworth-Heinemann, Oxford, 2000.
[36] Silvester, P.P. and R.L. Ferrari. "Finite Elements for Electrical Engineers", 3rd Edition, Cambridge University Press, Cambridge, 1996.
[37] Lapidus, L. and G.F. Pinder; "Numerical Solution of Partial Differential Equations in Science and Engineering", John WiLey & Sons Inc., New York, 1999.
[38] IMSL Numerical Library, Visual Numerics, Inc. San Ramon, California, United States.
[39] Nakamura, K., A. Shimizu, M. Koshiba, and H. Kazuya. "Finite-Element Analysis of Quantum Well of Arbitrary Semiconductors with arbitrary Potential Profiles," IEEE Journal of Quantum Electronics. Volume. 25, No. 5, 1989, pg. 889.
[40] Eisberg, R. and R. Resnick. *Quantum Physics of Atoms, Molecules, Solids, Nuclei, and Particles*, Second Edition, John WiLey & Sons, Inc., 1985.
[41] A. Messiah; "Quantum Mechanics", Dover Publications, Toronto, 1999.
[42] J.J. Brehm and W.J. Mullin; *Introduction to the Structure of Matter*, John WiLey & Sons Inc., 1989.
[43] F. Rief; *Fundamentals of Statistical and Thermal Physics*, McGraw-Hill Book Company, New York, 1965.
[44] W.H. Press, S.A. Teukolsky, W.T. Vetterling, and B.P. Flannery; "Numerical Recipes in Fortran 77, The Art of Scientific Computing", 2nd Edition, Cambridge University Press, Cambridge, 1992, page 352-355.
[45] Hermansson, B., and Yevich, D.; *Finite-element approach to band-structure analysis*, Physical Review B, Vol. 33, No. 10, May 1986, pg. 7241.

[46] Nakamura, K., A Shimizu and, M. Koshiba. "Finite-Element Calculation of the transmission Probability and Resonant-tunneling Lifetime Through Arbitrary Potential Barriers," IEEE Journal of Quantum Electronics, Volume 27, No 5, 1991, pg. 2035.
[47] Ando, Y. and Tomohiro Itoh;"Calculation of transmission tunneling current across arbitrary potential barriers", Journal of Applied Physics, Volume 61, No. 4, 1987, pg. 1497.
[48] L.D. Landau and E.M. Lifshitz; "Quantum Mechanics - Nonrelativistic Theory", McGraw-Hill, New York, 1958.
[49] W.H. Beyer (Editor); *CRC Standard Mathematical Tables*, 27th Edition, CRC Press Inc., Florida, 1986.